A wind tunnel study of the effect of density ratio on saltation threshold

A Thesis Presented for the

Master of Science

Degree

The University of Tennessee, Knoxville

Emily Victoria Nield

August 2018

Copyright © 2018 by Emily Victoria Nield

All rights reserved.

ACKNOWLEDGEMENTS

I would not have been able to complete this thesis without the support and encouragement from my family, friends, and colleagues. I would like to thank my mother and father for being my biggest cheerleaders and always giving me pep talks when I needed them the most. My brother Matthew, for letting my ramble nonstop about wind on other planetary bodies. Laverne, the woman who I consider to be a second mother, for always fighting for me. My close friends, Ariana and Molly, for always being there to provide moral support and to listen to all my triumphs, downfalls, and general silliness. Those two women are the epitome of the quote “That real queens adjust each other’s crowns.”

I would like to thank the Titan Wind Tunnel team for all their hard work, including Ken Smith for always accompanying me at NASA Ames and operating the wind tunnel, and Stephen Sutton for his support and thoughtful comments about this research. I thank Nathan Bridges, who passed away too soon, for all the work he put into this project.

Thank you to my committee members Christopher Fedo, Josh Emery, and Jasper Kok for their revisions to my work and their valuable feedback. Thank you to my advisor, Devon Burr, for all the edits, revisions, encouragement, thoughtful discussion, mentoring, and for the fun times at NASA Ames.

ABSTRACT

The aeolian saltation threshold is the minimum wind speed required to entrain sediment into saltation. An expression for saltation threshold is needed for Earth and other planetary bodies with aeolian activity. The saltation threshold has been inferred to be a function of the density ratio, the ratio of the density of the sediment being entrained to the density of the entraining fluid (ρ_p/ρ). Previous work, including experiments in the Venus Wind Tunnel (VWT), resulted in a curve for the dimensionless threshold parameter, *A*, as a function of the density ratio [*Iversen et al.* 1987]. However, that curve does not fit threshold data from the Titan Wind Tunnel (TWT) [*Burr et al.,* 2015]. In this work, I investigate the derived curve of the density ratio term [*Iversen et al*., 1987] by running new threshold experiments in the TWT under a range of density ratios conditions. I convert these new threshold wind speeds to *A* values and compare these new values to the density ratio curve of Iversen et al. [1987]. These new results with uncertainty estimates do not overlie the previous density ratio curve. Consequently, I derive new density ratio curves to fit the expanded data set using the same format as the previous expression but with new values for the two exponential parameters. The different curves are based on varying roughness heights, representing different ways that the boundary layer profile data could be fit and different definitions of threshold. These new curves have exponent parameters that increase the value of *A* in the transitional portion of the

curve previously defined by the VWT data. Multiple factors might explain why the TWT data do not lie on the density ratio curve derived from VWT data. This mismatch could be due to 1) grain size effects, 2) lack of sediment transport during boundary layer profile collection, 3) boundary layer depth in the small TWT test section, 4) different similitude parameters, 5) grain shape, and 6) grain sorting. This work raises important questions about the aerodynamics and sediment entrainment processes that occur at intermediate density ratios and impels future work.

TABLE OF CONTENTS

1. Introduction 1

2. Background 4

2.1 Threshold friction speed 4

2.2 Derivations of threshold friction speed for other planetary bodies 7

2.3 The density ratio term under different planetary conditions 11

2.4 Derivation of the *A* expression with $f(\rho_p/\rho)$ 17

2.4.1 Expressions for forces acting on a grain 19

2.4.2 Threshold equilibrium 21

2.4.3 Dimensionless threshold parameter, *A* 22

2.4.4 The *A* expression with the density ratio term 23

2.5 Density ratio expression derived by Iversen et al. [1987] 26

2.6 Threshold computational models 28

2.7 Questions regarding the validity of the model by Iversen and colleagues (1974-1987) 28

3. Hypotheses 31

4. Methods 32

4.1 Titan Wind Tunnel 34

4.2 Experimental setup 36

4.3 Data reduction 43

4.3.1 Boundary Layer Profiles (BLPs) 43

4.3.2 Derivation of z and z_o from Boundary Layer Profiles 45

4.3.3 Conversion of transducer voltage data to freestream speed 50

4.4 Uncertainty analysis 50

4.4.1 Uncertainty in freestream wind speed, $\delta u_\infty/u_\infty$ 51

4.4.2 Uncertainty in roughness height, $\delta z_o/z_o$ 53

4.4.3 Uncertainty in Boundary Layer Height, $\delta z/z$ 54

4.4.4 Uncertainty in friction speed, $\delta u_*/u_*$ 54

5. Results 55

5.1 Overview of results 55

5.2 Dimensionless threshold parameter, A, as a function of density ratio 61

6. Analysis 66

7. Discussion 69

7.1 Variations in the density ratio curve fitting 69

7.1.1 Threshold definition 69

7.1.2 Boundary Layer Profiles 73

7.2 Possible explanation for the mismatch between the VWT and the TWT data 79

7.3 Future work 89

8. Summary 91

List of References 93

Appendix 103

A1: Experimental set up for previous threshold studies 104

A2: Definitions of experimental threshold 105

A3: Experimental matrix 107

A4: R Code to reduce boundary layer profiles to find z and z_o 109

A5: R Code to reduce voltages to freestream speeds 119

Vita 128

LIST OF TABLES

Table 1: Expressions for *A* by Reynolds number range in the model by Iversen and White [1982] and Greeley and Iversen [1985]. 10

Table 2: Conditions necessary to achieve kinematic viscosity with the Titan near-surface atmosphere. Adapted from Burr et al. [2015a]. 42

Table 3: Summary of boundary layer profile results and the resulting z_o and z from each BLP. FMS indicates fan motor speed. 56

Table 4: Summary table of the threshold experiments displaying the experimental parameters, the freestream speed at threshold, the boundary layer profiles used to convert freestream to friction speed, the Reynold's friction number, and the dimensionless threshold parameter, *A*. Note that QF stands for quartzo-feldspathic. 58

Table 5: Parameters from original work by Iversen et al. 1987 and derived in this thesis from fitting to the data for each of the boundary conditions as indicated. These data show the possible range of parameter values. I endorse the data in bold. Combinations with insufficient data are noted. *This value is corrected from the equation given in Iversen et al. 1987 (see plot --- above) 80

Table 6: A comparison of similitude parameters in the Titan Wind Tunnel and Titan. Red is when the atmospheric density is the similitude parameter and blue represents when the similitude parameter is kinematic viscosity. 84

Table A1: A summary table of the experimental parameters used in previous threshold experiments. All experiments were conducted by placing material into the wind tunnel and incrementally increasing the wind speed in the tunnel until threshold, as defined……94

Table A2: A summary table of the experimental parameters used in previous threshold experiments. All experiments were conducted by placing material into the wind tunnel and incrementally increasing the wind speed in the tunnel until threshold, as defined……..95

Table A3: Experimental matrix used for threshold experiments conducted in the Titan Wind Tunnel……97

LIST OF FIGURES

Figure 1: Forces acting on a grain at rest subjected to an airflow; adapted from Iversen et al. [1976]. 5

Figure 2: The threshold parameter *A* as a function of grain diameter. Adapted from Iversen et al. [1976]. The numbers next to the materials in the legend refer to their densities in g/cm^3. A vertical line shows where the value of *A* becomes independent of size at values of D_p > 200 µm. 14

Figure 3: Threshold parameter *A* plotted as a function of particle Reynolds number for various fluids. Adapted from Iversen et al. [1987]. A vertical line shows where *A* becomes independent of the particle friction Reynolds number ($Re_{*t} \geq 10$). 15

Figure 4: Threshold parameter *A* plotted as a function of the density ratio for various fluids for particles > 200 µm diameter and Re_{*t} >10. Adapted from Iversen et al. [1987], with their density ratio curve overlaid on top of the data. A subset of data for the same filtering conditions collected from the Titan Wind Tunnel [*Burr et al*., 2015a] is also plotted and shown not to fit the curve. Note that the plotted curve shown in the Iversen et al. [1987] publication is not consistent with the expression they derived (see section 2.5). 16

Figure 5: Balance of moments with forces showing in blue and moment arms indicated in light green. 18

Figure 6: The original density ratio curve plot as printed in the Iversen et al. [1987] publication. 27

Figure 7: A comparison of 1) the density ratio curve plotted as in Iversen et al. [1987] (solid line) but which does not match the original expression for *A*, and 2) the expression that matches the original curve (dashed line) but which does not fit the data. 27

Figure 8: A flow chart outlining the methods used to collect and reduce the data. 33

Figure 9: (top) Photograph of the Titan Wind Tunnel. (bottom) Sectioned layout of the Titan Wind Tunnel. For clarity, only the downwind observational ports are labeled, but the upwind port is visible (to the left) in the photograph. From Burr et al. [2015b]. 35

Figure 10: The spread of experimental density ratios in this thesis compared to those in previous literature. Iversen et al. [1987] includes experiments conducted in water, the Venus Wind Tunnel, and the Iowa State University Wind Tunnel. Burr et al. [2015a] experiments were conducted at the Titan Wind Tunnel. 37

Figure 11: a) Experimental setup showing the positioning of the high-speed video (HSV) camera and the laser system used to illuminate the grains at the downwind observation portal for the 2017 experimental configuration. b) A view of the inside of the tunnel at the downwind observation port showing the laser light sheet illuminating the bed of sediment. c) Photo of the trip plate that was used to induce a steady state flow in the TWT during the 2017 experiments collected for this thesis. 40

Figure 12: A comparison of boundary layer profiles for different fan motor speeds taken with and without roughness elements. Boundary layer profiles taken with and without roughness elements converge at approximately the same location, which will result in similar roughness heights..... 41

Figure 13: Boundary layer profile adapted from Shao [2008]. 44

Figure 14: Boundary layer profiles for quartzo feldspathic, 833-1000 microns, at 8 bar for various fan speeds, taken without roughness elements. 48

Figure 15: Derivation of parameters to solve the Law of the Wall (Eq. 28), using boundary layer profile for quartzo-feldspathic sand, 833-1000 microns, at 8 bar taken at 75% fan speed. The solid lines represent the two regressions taken to determine a) the roughness height, z_o, which is derived from the y-intercept, and b) the freestream, *z,* which is the point of intersection of these two lines. Two regions could be fit to derive

the z_o; the solid line denotes the upper region of the BLP (used in this thesis) and the dashed line denotes the lower region of the BLP..... 49

Figure 16: Experimental threshold speeds from the TWT experiments performed for this thesis, plotted as a function of grain diameter. The graphs are subdivided by the atmospheric pressure for each experiment. QF refers to a quartzo-feldspathic composition. 60

Figure 17: Threshold parameter *A* plotted as a function of particle Reynolds number for various atmospheric pressures. This plot shows how the friction Reynolds number is no longer dependent on *A* after approximately Re_{*t}>10, This graph only includes data collected in this work and does not include the Burr et al. [2015a] data collected in the TWT..... 62

Figure 18: Threshold parameter *A*, derived from various sources, plotted as a function of the density ratio for various fluids for particles >200 µm diameter and Re_{*t} >10. Adapted from Iversen et al. [1987], with their density ratio curve overlaid on top of the data. A subset of data for the same filtering conditions collected from the Titan Wind Tunnel [*Burr et al*., 2015a] is also plotted and shown not to fit the curve. Previously published data did not include error bars..... 63

Figure 19: Values for the threshold parameter *A*, derived from TWT experiments, plotted as a function of the density ratio for particles > 200 µm diameter and Re_{*t} >10 sorted

by grain size. Adapted from Iversen et al. [1987], with their density ratio curve also shown. The data collected previously from the Titan Wind Tunnel [*Burr et al*., 2015a] are marked by triangles. 65

Figure 20: Threshold parameter *A* plotted as a function of the density ratio for various fluids for particles >200 μm diameter and Re_{*_t} >10. Adapted from Iversen et al. [1987] (dashed curve). A subset of data for the same filtering conditions collected from the Titan Wind Tunnel [*Burr et al*., 2015a] is also plotted along with the data collected for this thesis. The density ratio curve overlaid on top is derived in this thesis (solid curve). The density ratio curve derived using only TWT data is overlaid on the graph (dotted curve). The definition of threshold for this plot is 50% bed motion..... 68

Figure 21: Threshold parameter *A*, for which the definition of threshold is 'patches', sporadic or episodic grain motion (Burr et al. 2015a), plotted as a function of the density ratio for various fluids for particles > 200 μm diameter and Re_{*_t} >10 (solid line). Adapted from Iversen et al. [1987], with their density ratio curve (dashed line) overlaid on top of the VWT data, which did not include error bars. The density ratio curve derived using only TWT data is overlaid on the graph (dotted curve). 72

Figure 22: Boundary layer profiles taken with saltation (solid circles) and without saltation (open circles). These profiles show that the wind speed is consistently

higher without the presence of saltation which produces a smaller roughness height. Reproduced from Bauer et al. [2013]. 74

Figure 23: The sensitivity of the threshold friction speed to the roughness height. When the roughness height is lower than 10 µm, the threshold friction speed changes drastically. 77

Figure 24: The change in wind speed for a change in roughness height, showing the sensitivity of the friction speed to roughness height. Reducing the value of z_o by an order of magnitude significantly affects the value of threshold friction speed. 77

Figure 25: Threshold parameter *A* plotted as a function of the density ratio for various fluids for particles >200 µm diameter and Re_{*t} >10 (solid line). Adapted from Iversen et al. [1987], with their density ratio curve overlaid on top of the data (dashed line). The thesis data were derived using the z_o's calculated from the lower region of the boundary label profile. The definition of threshold for this plot is 50% bed motion. The density ratio curve derived using only TWT data is overlaid on the graph (dotted curve). 78

Figure 26 : Photographs of materials used in the Titan Wind Tunnel showing how the QF material is more rounded than the Walnut Shells and Plastic Chips. 86

Figure 27: Values of the threshold parameter *A*, derived from TWT experiments, plotted as a function of the density ratio for various fluids for particles >200 μm diameter and Re_{*t} >10 sorted by grain material. Adapted from Iversen et al. [1987], with their density ratio curve overlaid on top of the data. Data collected previously from the Titan Wind Tunnel [*Burr et al*., 2015a] are included. 87

LIST OF SYMBOLS

Symbol	Meaning
A	Dimensionless threshold parameter
D_p	Mean particle diameter
F	Force
$f(\rho_p/\rho)$	Density ratio function
g	Gravitational acceleration
$h(Re_*)$	Reynolds number function
K_D	Drag coefficient
K_L	Lift coefficient
K_M	Moment coefficient
K_P	Interparticle force coefficient
m	Mass of the particle
P_{dyn}	Dynamic pressure
P	Static pressure
Re_*	Particle frictions Reynolds number
Re_{*t}	Particle frictions Reynolds number at threshold
u_{ft}	Fluid threshold speed
u_{it}	Impact threshold speed
u_{*ft}	Fluid threshold friction speed
u_{*it}	Impact threshold friction speed
u_∞	Freestream windspeed
z	Height of boundary layer profile
z_o	Roughness length
$\delta x/\mathrm{x}$	Fractional uncertainty of a variable
κ	von Kármán constant
ν	Kinematic viscosity
ρ	Fluid density
ρ_p	Particle density
τ	Shear stress

1. Introduction

Aeolian processes classically refer to the entrainment, transport, and deposition of sand and dust by the wind. These processes can lead to the creation and evolution of small-scale bedforms, like ripples, up to large-scale bedforms, such as dunes. The creation and evolution of these bedforms require a supply of granular material and winds of sufficient strength to move it. Any planet that has a dynamic atmosphere and a solid surface with granular material is therefore subject to aeolian processes [*Kok et al.*, 2012].

Aeolian processes provide a direct link between the atmosphere and the surface. Thus, the identification and study of aeolian landforms can lead to a greater understanding of the effect of current and past atmospheric conditions on planetary surfaces [*Greeley and Iversen*, 1985]. Aeolian studies have provided information about, for example, the various ways that sediment can be transported by the wind (saltation, suspension, and traction) [*Bagnold*, 1941]; the rate of abrasion on Mars and Venus using ventifacts [e.g. *Laity a& Bridges*, 2009; *Garvi*n, 1981]; the global wind circulation models on Mars, Venus, and Titan using wind streaks [e.g. *Cohen-Zada et al.*, 2016]; and the dust generation and transportation on Earth and Mars [e.g. *Reiss et al*., 2016].

Observations of aeolian bedforms give evidence of aeolian activity on Mars, Venus and Titan. On Mars, orbiters have taken photos of extensive fields of barchan, transverse,

dome, longitudinal, and star dunes [e.g., *Hayward, Fenton,* & *Titus, 2014; Hayward et al*., 2007]. The Magellan orbiter documented fields of transverse dunes on Venus [*Greeley et al.*, 1992; *Weitz et al.*, 1994], and the Cassini spacecraft, during exploration of the Saturnian system, returned images showing linear sand dunes on Titan [*Lorenz et al.*, 2006].

Formation of dunes requires the movement of sand in saltation. R. A. Bagnold was the first researcher to collect and publish extensive results from wind tunnel studies investigating the movement of sediment. Since Bagnold's [1941] seminal work on the physics of windblown sand, researchers have been deriving equations to model threshold speed and using wind tunnel data to parameterize their models. For example, Chepil and Milne introduced roughness elements in their experiments to better replicate wind erosion over farmland [*Chepil & Milne*, 1941]. As another example, McKenna Neuman's model included the effects of temperature and humidity on the entrainment of grains based on climate controlled wind tunnel experiments [*McKenna Neuman*, 2003].

The saltation threshold speed is a fundamental parameter in aeolian science, influencing all aspects of sediment movement, including aeolian mass flux [*White*, 1979; *White*, 1981] and minimum aeolian erosion potential [Sagan *et al*., 1977] and effectiveness [*Bridges et al*., 2005]. It impacts our analysis and understanding of phenomena from a local scale, (e.g., ventification [*Knight*, 2008] and dune orientation

[*Rubin & Hunter*, 1987]) to the global scale (e.g., relative importance of various resurfacing processes [*Bridges et al*., 2012]), all of which have important implications for past climate conditions and climate change [*Bridges et al*., 1999; *Greeley et al*., 2000; *Golombek et al*., 2006; *Ewing et al.*, 2013].

Building on terrestrial work, saltation threshold models were developed for application to other planetary bodies over a wide range of pressures [*Iversen et al.*, 1976a; *Iversen and White*, 1982]. These empirically-derived models were based on the presumption that the authors observed fluid threshold (see section 2.1) in their wind tunnel experiments [*Greeley et al.*, 1977, p. 10]. When subsequent data did not fit the old models, a density ratio term (density of the sediment/density of the fluid) was developed for inclusion in the planetary threshold model. However, the derivation of the term and the mismatch of more recent data evoke questions as to its physical justification.

In this work, I investigate the validity of the density ratio term and its inclusion in the Iversen et al. [1987] threshold model. Testing the validity of the density ratio term – and thus, of their model – entailed running new threshold experiments under a range of pressures and, therefore, density ratio conditions and comparing these new data of threshold wind speed to the density ratio curve of Iversen et al. [1987]. The results of the work presented here raise important questions about the aerodynamics and sediment entrainment processes that occur at intermediate density ratios.

2. Background

2.1 Threshold friction speed

The initiation of the saltation process may occur under two different conditions: fluid threshold or impact threshold (also referred to as static threshold and dynamic threshold). Fluid threshold wind speed (u_{ft}) refers to the minimum wind speed necessary to initiate the saltation of a grain owing to the direct pressure of the fluid [*Bagnold*, 1941]. Impact threshold wind speed (u_{it}) refers to the minimum wind speed necessary to initiate the saltation of a grain in conjunction with the impact of saltating grains from upwind [*Bagnold*, 1941].

In theory, a grain of sand sitting on a bed of similar-sized grains under airflow is subjected to a variety of forces including: aerodynamic drag, aerodynamic lift, gravity, and interparticle forces (Figure 1). At the fluid threshold of motion, the moments that result from the aerodynamic drag and lift force are equal to the moments that results from the force of gravity and the interparticle force which initiates movement of the grain [*Bagnold*, 1941; *Iversen et al.*, 1976]. Under impact entrainment (not shown), the kinetic energy of the grain(s) from upwind constitutes an additional motive force.

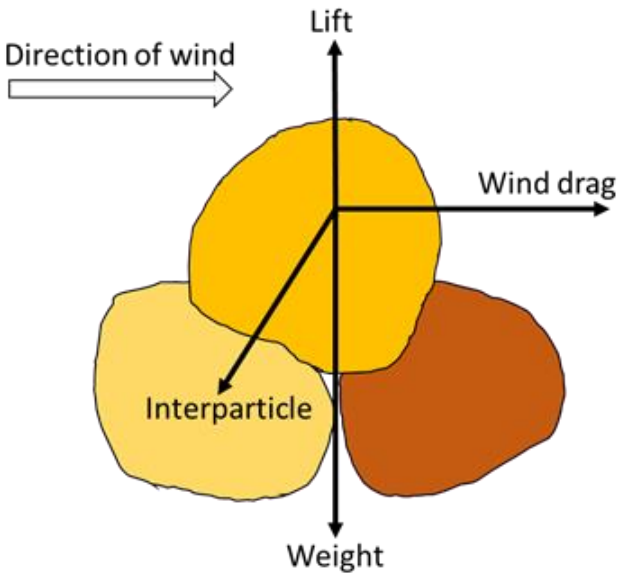


Figure 1: Forces acting on a grain at rest subjected to an airflow; adapted from Iversen et al. [1976] See Figure 5 for a diagrammatic presentation of the moments.

In the work presented here, threshold is quantified using friction speed (u_{*t}), not wind speed (u_t). Friction wind speed is a characteristic velocity that describes the amount of shear at the surface. Wind speed varies with the height above the surface, whereas a friction wind speed is independent of the height and so provides a more consistent, and thus more reliable, measure of the effect of the wind at the surface. The friction speed, a measure of vertical momentum flux, is defined in terms of the shear stress, τ, that the wind exerts on the surface as shown in equation 1 where ρ is the fluid density

$$u_* = \sqrt{\frac{\tau}{\rho}}. \tag{1}$$

Bagnold used the balance of the lift force and the gravitational force (Figure 1) at the moment of entrainment to derive the threshold friction speed as:

$$u_{*t} = A\sqrt{\frac{\rho_p - \rho}{\rho} g D_p}, \tag{2}$$

where A is the dimensionless threshold parameter, ρ_p is the particle density, D_p is the mean particle diameter, and g is the gravitational acceleration. The parameter A was experimentally determined by Bagnold. He suggested that it is dependent on the particle frictions Reynolds number at threshold (Re_{*t}) defined as:

$$Re_{*t} = \frac{u_{*t} D_p}{\nu}, \tag{3}$$

where v is the kinematic viscosity. Bagnold simplified A by setting it equal to 0.1 for all grains with a diameter larger than 250 microns. Bagnold calculated this value of for A from his threshold speed experiments by negating dependence on the interparticle force, Re_{*_t} and the lift force.

2.2 Derivations of threshold friction speed for other planetary bodies

With the discovery of aeolian activity on other planetary bodies [see reviews in *Greeley and Iversen*, 1985 and *Lorenz and Zimbelman*, 2014], researchers developed new interest in threshold models appropriate for these various bodies. Wind tunnel experiments have been a constant tool for parameterizing these models, and a historical survey of those previous results shows the importance of appropriate boundary conditions for the planetary bodies being investigated [*Burr et al*., 2015b].

Initial planetary experiments were conducted under ambient (terrestrial) conditions. The experiments were run in the Iowa State University (ISU) Wind Tunnel to test the validity of Bagnold's threshold equation at ambient conditions. The experiments at ISU lead to the first expression in Table 1 (the generic form). These experiments, conducted from the mid 1970's through 1980's (Table A1) in a variety of wind tunnels led to a suite of equations describe the functional behaviour ofthe dimensionless threshold parameter, A, in different flow regimes (Table 1, expressions 2 to 4). This previous work in the ISU wind tunnel was based on the expectation that operations at ambient

conditions would produce results that could be mathematically corrected to Martian conditions [*Greeley et al.*, 1974, p. 335]. This set of experiments enabled prediction of threshold friction speeds as a function of grain size for Mars and Venus [*Iversen et al.*, 1976a; *Iversen et al.*, 1976b]. The results from their first set of experiments indicated that A is not uniquely a function of Re_{*t} but that it also depends on interparticle forces (parameterized by the exponent for D_p^n in Table 1). which have a greater influence on smaller particles due to their larger surface area-to-volume ratios. These interparticle forces are caused by van der Waal's forces, electrostatic charges, and forces between adsorbed films, all of which make smaller grains more difficult to entrain due to their larger surface-area-to-volume ratio. In other words, this cohesion results in a higher threshold wind speed for grains below a certain size [*Iversen et al.*, 1976b].

In 1976, the Martian Surface Wind Tunnel (MARSWIT) came into operation for the purpose of studying aeolian processes in a low pressure environment [*Greeley et al.*, 1976]. Greeley et al. [1976] conducted a series of experiments testing threshold speeds under Martian conditions (~6 mbar). In contrast to expectation, the data from the MARSWIT experiments did not match the predicted results based on mathematical extrapolation from ambient conditions. This mismatch led to refinement of Bagnold's expression of threshold friction speed (Eq. 2), by defining different formulae for A for a given range of Re_{*t} [*Greeley et al*., 1976]. This refined expression (Table 1, last 3 rows)

follows the same generic form for A as shown in the first expression in Table 1, where A_1 is a dimensionless constant and K is a constant having units of g cm^{-2} sec^{-2}. Based on previous work, this generic expression formulates the threshold parameter A as a function of Re_{*t}, and also assumes interparticle forces are proportional to an unknown power n of the particle diameter [*Iversen and White*, 1982]. The value for n of 2.5 (Table 1, last 3 rows) was derived from fitting the experimental data. The literature from this time suggests that experiments under these low-fluid-density conditions were considered to involve fluid ("static") threshold [*Greeley et al*. 1977, p. 10]. However, subsequent modeling shows that this presumption was likely incorrect. Specifically, numerical modeling has shown that under low-fluid-density conditions, impact threshold is lower than fluid threshold [*Kok*, 2010]. This modeling suggests that the threshold in the MARSWIT, described as "the movement of particles over the entire bed" (Table A2), was a result of some (unobserved) impact of upwind grains.

Table 1: Expressions for *A* by Reynolds number range in the model by Iversen and White [1982] and Greeley and Iversen [1985].

Re_{*t} Range	Expression for *A*
Generic Form	$A = A_1 f(Re_{*t}) \left(1 + \frac{K}{\rho_p g D_p^n}\right)^{\frac{1}{2}}$
$0.03 \leq Re_{*t} \leq 0.3$	$A = 0.2 \left(\frac{1 + 0.006/\rho_p g {D_p}^{2.5}}{1 + 2.5 Re_{*t}}\right)^{\frac{1}{2}}$
$0.3 \leq Re_{*t} \leq 10$	$A = 0.129 \left(\frac{1 + 0.006/\rho_p g {D_p}^{2.5}}{1.928 {Re_{*t}}^{0.092} - 1}\right)^{\frac{1}{2}}$
$Re_{*t} \geq 10$	$A = 0.12 \left(\frac{1 + 0.006}{\rho_p g {D_p}^{2.5}}\right)^{\frac{1}{2}} \left(1 - 0.0858 e^{-0.0617(Re_{*t} - 10)}\right)$

Based on this refined threshold model derived from wind tunnel data for relatively low-density (Martian and terrestrial) conditions, a theoretical expression of threshold at high-density (Venusian) atmospheres was derived [*Iversen and White*, 1982]. The Venus Wind Tunnel was then developed to study the entrainment of sediment under high pressure (Venusian) conditions, in order to test the validity of the expressions in Table 1 under Venus conditions. The data collected in this tunnel [*Greeley et al.*, 1984] were found to be inconsistent with their theoretical Venusian expression [*Iversen et al.*, 1987]. Iversen *et al.* suggested that this discrepancy between their theoretical expression and their experimental results was due to the effect of grain impact, which had not been accounted for in previous force-balance equations used to derive threshold. To correct their model to align with the experimental results, they introduced into the formula for A a density ratio term, $f(\rho_p/\rho)$, where ρ_p, is the density of the particle and ρ, is the density of the fluid.

2.3 The density ratio term under different planetary conditions

Three parameters affect A in the threshold speed model constructed by Iversen et al. [1987]: (1) the particle friction Reynolds number (Re_{*t}), (2) the interparticle force, and (3) the density ratio. To isolate the effect of the density ratio term on the threshold parameter A, Iversen et al. [1987] compiled extant threshold data for a range of density ratio values: under terrestrial conditions at ISU [*Iversen et al*., 1976b], under low pressure conditions at MARSWIT [*Greeley et al*., 1980], under high pressure conditions at the VWT

[*Greeley et al*., 1984] and with water as the fluid [*Graf,* 1971]. They filtered these threshold data so that (1) the grain diameter was larger than 200 μm, and (2) Re_{*t} was larger than 10.

The first criterion (D_p >200 μm) was set in order to make the interparticle force term negligible. As shown in Figure 2, the value of *A* becomes independent of size for D_p greater than 200 μm. The second criterion (Re_{*t} > 10), was designed to ensure that *A* is independent of the particle friction Reynolds number. As shown in Figure 3, the data scatter in *A* reduces significantly for Re_{*t} >10 and begins to approach a universal asymptote where Re_{*t} is independent of *A*.

The filtered data for *A* were plotted vs the density ratio, ρ_p/ρ, and fitted with a curve described by the expression with the density ratio term shown on Figure 4. Although its derivation was impelled by data under intermediate density-ratio (i.e., Venus Wind Tunnel) conditions, this continuous expression was intended to correct their previous formulation so as to align with experimental results at all density-ratio conditions. At density ratios > 1000, as for atmospheric conditions on Earth or Mars, the density-ratio term ($f(\rho_p/\rho)$) goes to zero and the original expression for *A* is recovered. At intermediate density ratios, as on Venus (or Titan), this term becomes large and the expression for *A* diverges (increases) in value from the original static value of *A* (0.11) assigned by Bagnold

[1941] based on terrestrial conditions. As the density ratio approaches 1, as experienced in fluvial environments on Earth, the *A* value approaches 0.2.

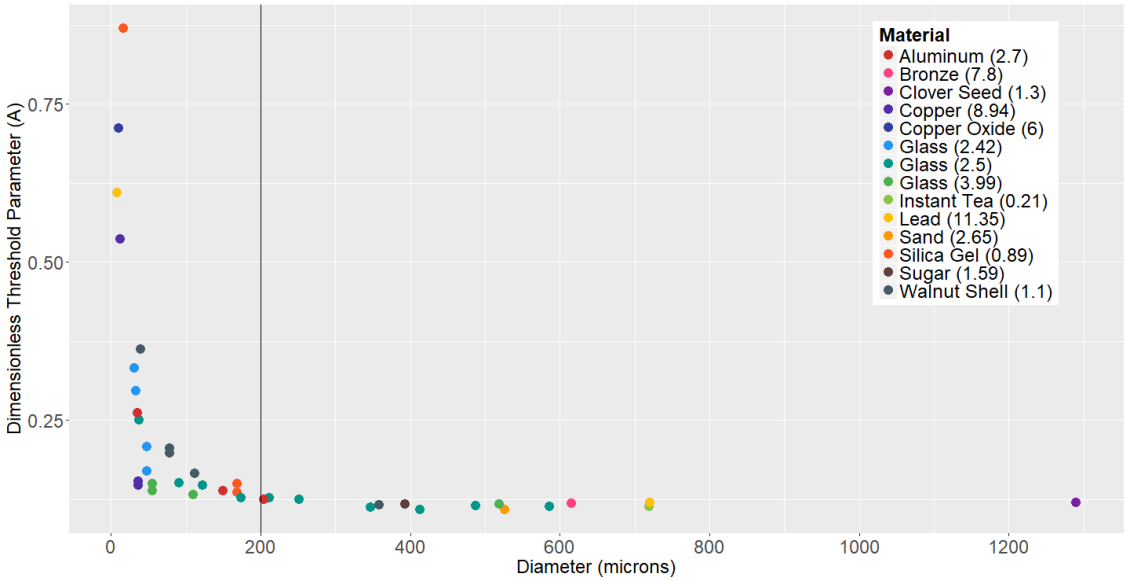


Figure 2: The threshold parameter *A* as a function of grain diameter. Adapted from Iversen et al. [1976]. The numbers next to the materials in the legend refer to their densities in g/cm^3. A vertical line shows where the value of *A* becomes independent of size at values of $D_p > 200$ µm.

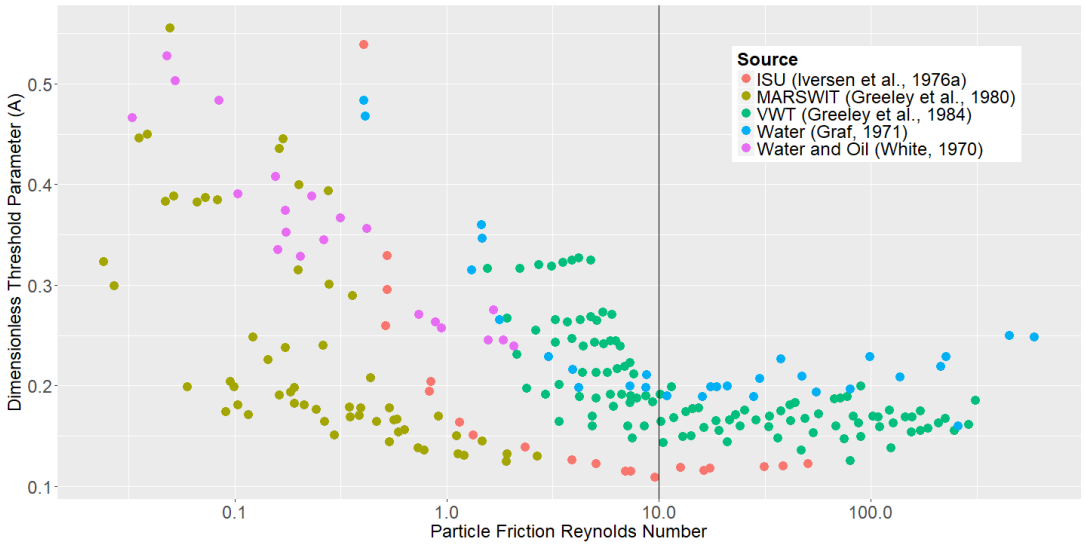


Figure 3: Threshold parameter *A* plotted as a function of particle Reynolds number for various fluids. Adapted from Iversen et al. [1987]. A vertical line shows where *A* becomes independent of the particle friction Reynolds number ($Re_{*t} \geq 10$).

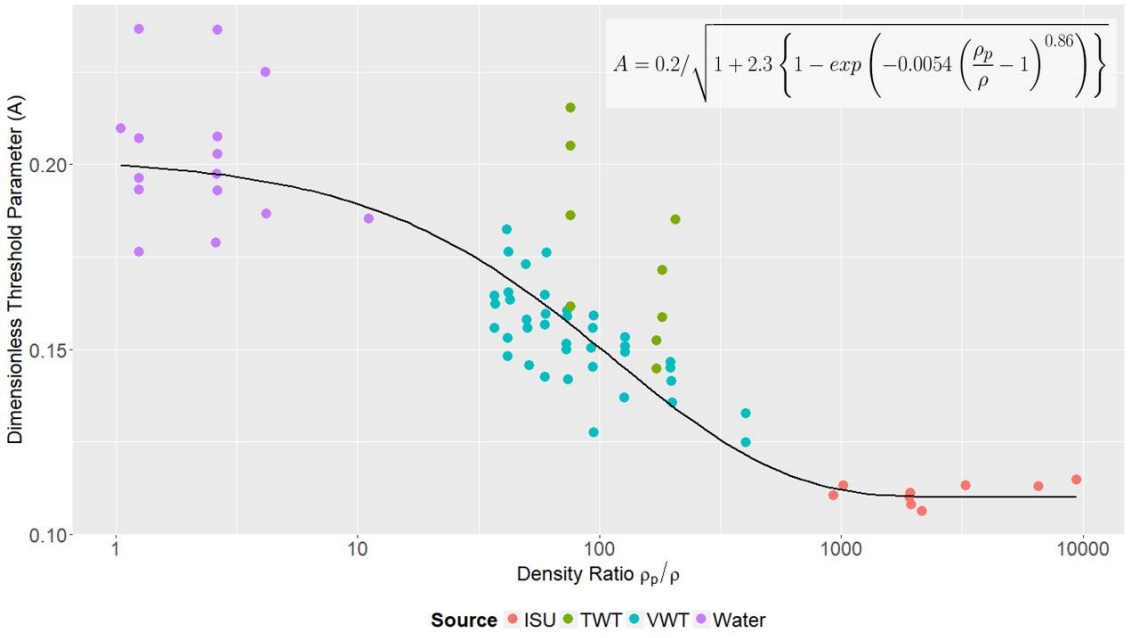


Figure 4: Threshold parameter *A* plotted as a function of the density ratio for various fluids for particles > 200 µm diameter and Re_{*t} >10. Adapted from Iversen et al. [1987], with their density ratio curve overlaid on top of the data. A subset of data for the same filtering conditions collected from the Titan Wind Tunnel [*Burr et al*., 2015a] is also plotted and shown not to fit the curve. Note that the plotted curve shown in the Iversen et al. [1987] publication is not consistent with the expression they derived (see section 2.5).

2.4 Derivation of the *A* expression with $f(\rho_p/\rho)$

A spherical grain resting on a bed of similar grains has the following forces acting on it: the lift force (F_L), the drag force (F_D), the combined force of gravity and buoyancy known as the weight (F_W), the interparticle force (F_P), and the aerodynamic moment (F_M). As shown in Figure 5, these forces act with respect to point P, so they constitute moments. At the point of threshold as defined by Bagnold [1941], the moments are at equilibrium with each other around the point *P* (Figure 5). Any increase in the wind speed will cause the moments of the lift and drag forces to exceed the moments of the weight and interparticle forces. As a result, the particle will rotate around *P* and lift from the surface. When a grain from upwind strikes the stationary grain on the bed, another force acts the grain, the impact force (F_I).

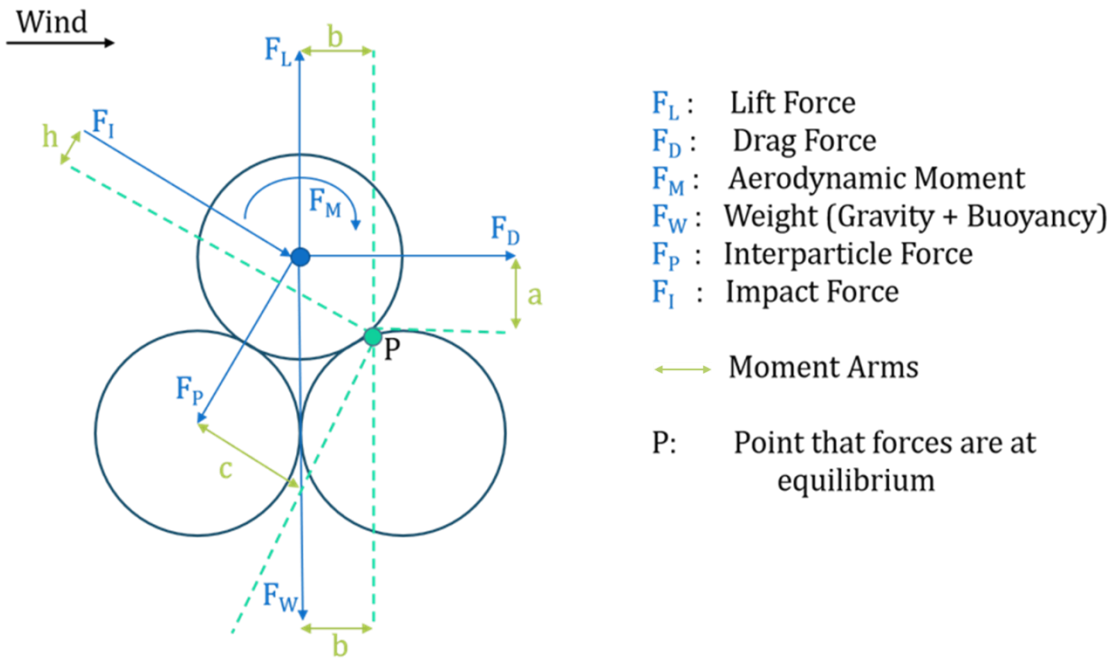


Figure 5: Balance of moments with forces showing in blue and moment arms indicated in light green.

Iversen et al. [1987] derived an expression for the dimensionless threshold friction speed, *A*, in terms of interparticle forces, Reynolds friction number Re_{*t} and the density ratio function, $f(\rho_p/\rho)$. Some steps of the derivation are omitted and their equation 14 for *A* contains a typo. For clarity, I provide the full derivation below.

2.4.1 Expressions for forces acting on a grain

The drag force (F_D) can be expressed in terms of the air density (ρ), the friction speed (u_*), the median grain diameter (D_p), and the drag coefficient (K_D):

$$F_D = K_D \rho u_* D_p^2. \tag{4}$$

The lift force (F_L) is

$$F_L = K_L \rho u_* D_p^2, \tag{5}$$

where K_L is the lift coefficient.

The aerodynamic moment is

$$F_M = K_M \rho u_* D_p^3, \tag{6}$$

where K_M is the moment coefficient.

The weight (F_W) is

$$F_W = (\pi/6)(\rho_p - \rho) g D_p^3, \tag{7}$$

where g is the gravitational acceleration, and ρ_p is the density of the grain.

Interparticle force (F_P) includes the effects of relative humidity, surface characteristics, and electrostatic forces. These multiple variables can be combined into a simplified expression using the van der Waal's force, where less important interparticle forces are ignored

$$F_P = K_P D_P, \tag{8}$$

where K_P is the interparticle force coefficient.

It is assumed that u_* and particle speed are proportional. This proportionality has recently been disputed by Martin and Kok [2017] who argued for a nonlinear 3/2 stress-flux scaling between particle speed and u_* when the density ratio is intermediate between terrestrial aeolian and fluvial conditions. Under such conditions, as on Titan, the scaling factor is ambiguous. I will be assuming the proportionality in order to follow the derivation of the Iversen et al. [1987] threshold model, which is the model I am studying in this work. The impact force, F_I, is calculated by setting the kinetic energy of the incoming grain to the work done in moving the resting grain through a distance proportional to its diameter

$$(1/2)m{u_*}^2 = F_I * KD_P, \tag{9}$$

where m is the mass of the grain and K is a constant. The mass of the grain is calculated using the volume and the density of the grain, $m = (\pi/6)D_P^3\rho$. Substitution of the mass into the above equation gives

$$\frac{1}{2}\left(\frac{\pi}{6}\right) {D_p}^3 \rho_p {u_*}^2 = K D_p F_I. \tag{10}$$

Solving for F_I yields

$$F_I = \frac{\pi {D_p}^2 \rho_p {u_*}^2}{12K}. \tag{11}$$

Setting the constant ($\pi/12K$) equal to constant K_1 results in the expression for F_I,

$$F_I = K_1 {D_p}^2 \rho_p {u_*}^2. \tag{12}$$

2.4.2 Threshold equilibrium

At threshold, the particle forces are assumed to be in equilibrium about the point P. The forces causing the grains to move are equal to the forces causing the grain to remain stationary (Figure 5):

$$F_D a + F_L b + F_M + F_I h = F_W b + F_P c. \tag{13}$$

The moment arms are proportional to the particle size and can be rewritten as such: $a = a_1 D_p$, $b = b_1 D_p$, $c = c_1 D_p$, and $h = h_1 D_p$. Input Eq. 4 through 8 and 12 into Eq. 13 gives

$$\begin{aligned} &K_D \rho u_*^2 D_p^3 a_1 + K_L \rho u_*^2 D_p^3 b_1 + K_M \rho u_*^2 D_p^3 + K_1 \rho u_*^2 D_p^3 h_1 = \\ &(\pi/6)\,(\rho_p - \rho)\, g D_p^4 b_1 + K_p D_p^2 c_1 \end{aligned}. \tag{14}$$

The factor $u_*^2\rho_p D_p^3$ may be factored out to yield

$$u_*{}^2\rho_p D_p{}^3\left(K_D a_1 + K_L b_1 + K_M + K_1 h_1 \rho_p/\rho\right) = (\pi/6)\left(\rho_p - \rho\right) g D_p{}^4 b_1 + K_p D_p{}^2 c_1 \quad (15)$$

Solving for u_*^2 results in the expression

$$u_*{}^2 = \frac{(\pi/6)\left(\rho_p - \rho\right) g D_p^2 b_1 + K_p c_1}{\rho_p D_p \left(K_D a_1 + K_L b_1 + K_M + K_1 h_1 \rho_p/\rho\right)}. \quad (16)$$

2.4.3 Dimensionless threshold parameter, *A*

Bagnold [1941] derived the following expression for A^2:

$$A^2 = \frac{u_*^2 \rho}{\left(\rho_p - \rho\right) g D_p}. \quad (17)$$

Combining Eqs. 15 and 17 and solving for A^2 gives

$$A^2 = \frac{\left(\frac{\pi}{6}\right)\left(\rho_p - \rho\right) g D_p{}^2 b_1 + K_p c_1}{\left(\rho_p - \rho\right) g D_p{}^2 \left(K_D a_1 + K_L b_1 + K_M + K_1 h_1 \rho_p/\rho\right)}. \quad (18)$$

The expression $(\pi/6)\left(\rho_p - \rho\right) g D_p{}^2 b_1$ can be factored out to yield

$$A^2 = \frac{\left(\frac{\pi}{6}\right) b_1 \left(1 + \frac{K_P c_1 6}{\left(\rho_p - \rho\right) g D_p{}^2 b_1 \pi}\right)}{K_D a_1 + K_L b_1 + K_M + K\ h_1 \rho_p/\rho}. \quad (19)$$

In the denominator, $K_D a_1 + K_L b_1 + K_M$, are functions of Re_{*t}, and can be rewritten as $h(Re_{*t})$.

Comparison with Iversen et al. [1987] equations 16 and 17 shows that the expression

$K_I h_1 \rho_p/\rho$ is the density ratio function $f(\rho_p/\rho)$. The significance of the interparticle force decreases as the particle size increase. All the grains in this work are over 200 µm making the interparticle force insignificant. K_P is therefore reduced to zero. Simplifying Eq. 19 gives

$$A^2 = \frac{K}{h\left(Re_{*t}\right) + f\left(\rho_p/\rho\right)}, \tag{20}$$

which is the general model for the *A* term (see Table 1).

2.4.4 The *A* expression with the density ratio term

The data plotted by Iversen et al. [1987] showing *A* vs ρ_p/ρ (Figure 4 of this thesis) indicates that the expression for *A* with the density ratio term will be sigmoidal and thus have the form of $1/(1+e^{-x})$, which can be rewritten as:

$$A^2 = \frac{\alpha}{\left(1 + \beta\left\{1 - e^{\left[-\gamma(\rho_p/\rho - 1)^{\lambda}\right]}\right\}\right)}, \tag{21}$$

where α, β, γ, and λ are constants. α represents the upper limit of the sigmoidal function.

The upper and lower limits of the sigmoidal expression need to be determined. The lower limit was derived by Bagnold [1941] as A=0.11 for high density ratios (terrestrial conditions). The upper limit for *A* is determined by using water as the end member for low density ratios. The coefficients in Eq. 21 have been determined for liquid water.

Coleman [1967] derived values for the coefficients a_1, b_1, and c_1 for a sphere resting on a closely packed bed of spheres in the same configuration as Figure 5, they are $a_1=1/6^{1/2}$, $b_1=1/4*3^{1/2}$, and $c_1=1/2*2^{1/2}$. Chepil [1958] derived the following values for spheres in water: $K_M=0$, $K_L=2.2$, and $K_D=3.85$. The density ratio term, $f(\rho_p/\rho)=K_1h_1\rho_p/\rho$, is negligible in water and can be assumed to be equal to zero. These values are input into Eq. 21to produce

$$A^2 = \frac{(\pi/6)\left(\frac{1}{4\sqrt{3}}\right)}{3.85\left(\frac{1}{\sqrt{6}}\right) + 2.2\left(\frac{1}{4\sqrt{3}}\right)} = \frac{0.075575}{1.889} = 0.04 \quad (22)$$

From Eq. 22, A equals 0.2 in water, making it the upper limit for the sigmoidal expression. This upper limit of 0.2 has been supported by flume experiments [Bridge and Bennett, 1992; Elhakeem and Imran, 2012; Tregnaghi et al., 2012]. Substituting in the coefficients for water in gives

$$A = \sqrt{\frac{0.0756}{1.89 + f(\rho_p/\rho)}}. \quad (23)$$

The value 1.89 can be factored out of the denominator to yield

$$A = \sqrt{\frac{0.0756}{1.89\left(1 + f(\rho_p/\rho)\right)}} = \frac{0.2}{\sqrt{1 + f(\rho_p/\rho)}}. \quad (24)$$

The 0.2 in the numerator in Eq. 25 anchors the upper limit of the sigmoidal expression for *A*, i.e., when the density ratio term, $f(\rho_p/\rho)$, approaches 1 (Figure 4). Setting the lower limit of the sigmoidal expression to 0.11 (Bagnold, 1941) gives a value for $f(\rho_p/\rho)$ of 2.3, so that the expression for *A* becomes

$$A = \frac{0.2}{[1+2.3]^{1/2}} = 0.11 \quad . \tag{25}$$

Comparison of Eq. 25 with Eq. 21 shows that α=0.2 and β=2.3. Rewriting Eq. 21 with these new constants yields

$$A = \frac{0.2}{\sqrt{\left(1+2.3\left\{1-e^{\left[-\gamma(\rho_p/\rho-1)^{\lambda}\right]}\right\}\right)}} \quad . \tag{26}$$

The parameters γ and λ in Eq. 26 are calculated by fitting the model to the data. Iversen et al. [1987] fitted their data (Figure 4) to the curve in Eq. 26 and show on their plot the following expression:

$$A = 0.2/\sqrt{1+2.3\left\{1-exp\left(-0.0054\left(\frac{\rho_p}{\rho}-1\right)^{0.86}\right)\right\}} \quad . \tag{27}$$

However, this expression does not fit the data in Iversen et al. [1987]. That is, it does not describe the curve that appears to fit the data as shown on Iversen et al. [1987], their figure 3 (see Figure 4, solid line).

2.5 Density ratio expression derived by Iversen et al. [1987]

Figure 3 in the Iversen et al. [1987] (Figure 6 in this thesis) displays their data along with the curve they derived to fit it. The expression for the density ratio is provided on this figure. There is a mismatch between the plotted curve and the provided expression (Figure 7). Using the curve fitting toolbox in MATLAB 2017b, I derive an expression to describe the density ratio curve plotted in Iversen et al. [1987]. The value of γ in Eq. 26 is found to be equal to 0.0078, not 0.0054 as stated in their equation.

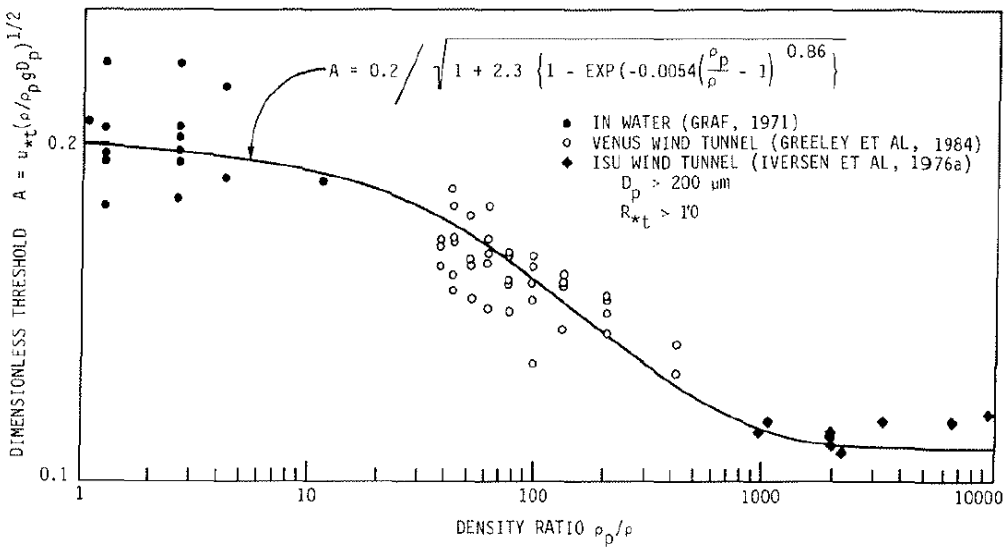


Figure 6: The original density ratio curve plot as printed in the Iversen et al. [1987] publication.

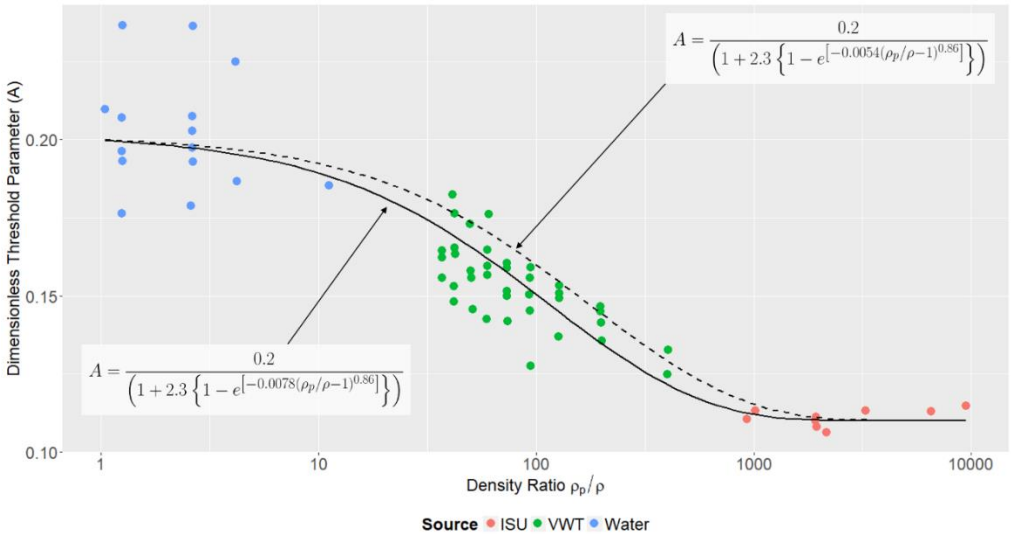


Figure 7: A comparison of 1) the density ratio curve plotted as in Iversen et al. [1987] (solid line) but which does not match the original expression for *A*, and 2) the expression that matches the original curve (dashed line) but which does not fit the data.

2.6 Threshold computational models

The computational model COMSALT [*Kok and Reno,* 2009; see also *Kok et al.*, 2012] quantifies fluid and impact thresholds on Earth, Mars, Venus, and Titan. Results from this model suggested that the impact threshold is far lower proportionately on Mars than it is on Earth. The low martian air density, along with the low gravity, allows a salting grain to travel higher from the bed and into faster moving air. As a result, the grain is able to impart more energy on the bed and can kick up grains for entrainment, which reduces the amount of energy required from the wind to entrain the grains. The COMSALT model [*Kok and Reno,* 2009; see also *Kok et al.*, 2012] also indicates that, conversely on planetary bodies with a dense atmosphere (i.e., Titan and Venus), the fluid threshold is lower than the impact threshold. In thicker atmospheres, lower wind speeds are required to entrain grains due to the additional force applied by the denser air. Under these conditions, the saltating grains are moving more slowly so that they have less energy to eject grains upon impact with the bed.

2.7 Questions regarding the validity of the model by Iversen and colleagues (1974-1987)

The derivation of the density ratio term excludes all data from the Mars Wind Tunnel due to the criterion that all the data used to derive the term must have a Re_{*t} >10. As shown in Figure 3, the data scatter in A reduces significantly when Re_{*t}>10 and begins

to approach an asymptote where Re_{*t} is independent of A. This universal asymptote encompasses all data from each wind tunnel. At the same time, however, each dataset exhibits its own unique asymptote. Selecting an asymptote for each dataset (e.g. MARSWIT, VWT, ISU) would allow more data (i.e., from the MARSWIT) to be used to derive the asymptote for high density ratio conditions, thereby potentially changing the model derived by Iversen et al. [1987].

A larger question is raised by the availability of new data. New experimental wind tunnels enable testing of previous models [*Burr et al*., 2015b]. Following the discovery of extensive aeolian dunes on Titan [*Lorenz et al.,* 2006], the Venus Wind Tunnel was refurbished and used to simulate Titan conditions [*Burr et al.,* 2015b]. Specifically, experiments were conducted to quantify threshold under Titan analog conditions [*Burr et al.,* 2015a]. The derived threshold friction wind speeds were compared to the model published by Iversen and White [1982] and Shao and Lu [2000], and found to be consistently ~40-50% higher than predicted by those models. The fit was improved when the density ratio term Iversen et al. [1987] was included. However, the data collected by Burr et al. did not fit on the density ratio curve shown in Figure 4.

According to Iversen et al. [1987], the density ratio should be influential for impact threshold conditions. However, Burr et al. [2015a] argued that they were observing fluid threshold. They supported this argument by citing numerical modeling results [*Kok and*

Reno, 2009; *Kok et al.,* 2012], which indicate that the fluid threshold is lower than the impact threshold on planetary bodies with a dense atmosphere (i.e., Titan and Venus). This explanation would imply that the first (lowest) threshold that they observed was fluid and not impact. Thus, whereas the fit of the Iversen and White [1982] model to the Titan Wind Tunnel (TWT) data is improved with the density ratio term, the physical justification for the inclusion of the term on the basis of computational modeling [*Kok and Reno,* 2009; *Kok et al.*, 2012] remains obscure.

The omission of the MARWIT data when deriving the density ratio curve [*Iversen et al*., 1987] and the results from the Titan Wind Tunnel experiments [*Burr et al.*, 2015a], in conjunction with computational modeling [*Kok and Reno*, 2009; *Kok et al.,* 2012], raise interesting questions about the experimental work upon which the derivation of the density ratio term is based. Why does the inclusion of the density ratio term improve the fit of Titan Wind Tunnel data? At the same time, why do those filtered data not fall on the density ratio curve (Figure 4)? Would the density ratio curve be more accurate with the inclusion of MARSWIT (or TWT) data? Is there any reason to think that the VWT data were imprecise / low? Answers to these questions could test the explanations as to why the Venus Wind Tunnel observations did not align with earlier models, change these commonly used experimental models, and explain the mismatch between the Titan Wind Tunnel data and the density ratio curve.

3. Hypotheses

The modeling of Kok et al. [2012] shows the importance of fluid vs impact entrainment at different pressures. However, the mismatch between the Titan Wind Tunnel data [*Burr et al.*, 2015a] and the threshold model along with the omission of MARSWIT data call into the question the accuracy of the expression for the density ratio curve [*Iversen et al*., 1987]. These facts lead to my two hypotheses.

Null Hypothesis: The density ratio expression derived by Iversen et al. [1987] is correct.

Alternative Hypothesis: The density ratio expression derived by Iversen et al. [1987] is incorrect.

These hypotheses are tested through collecting data from Titan Wind Tunnel experiments at different density ratios. The data are reduced and plotted on the Iversen et al. [1987] density ratio plot (Figure 4). If the data adequately fit on the Iversen et al. [1987] density ratio curve, then the null hypothesis would be supported. If the data do not adequately fit on the Iversen et al. curve [1987], then the alternative hypothesis would be supported. If the alternative hypothesis is supported, then the density ratio curve would be rederived using TWT data.

4. Methods

An overview of the methodology used in this thesis from data collection to data reduction is shown in Figure 8.

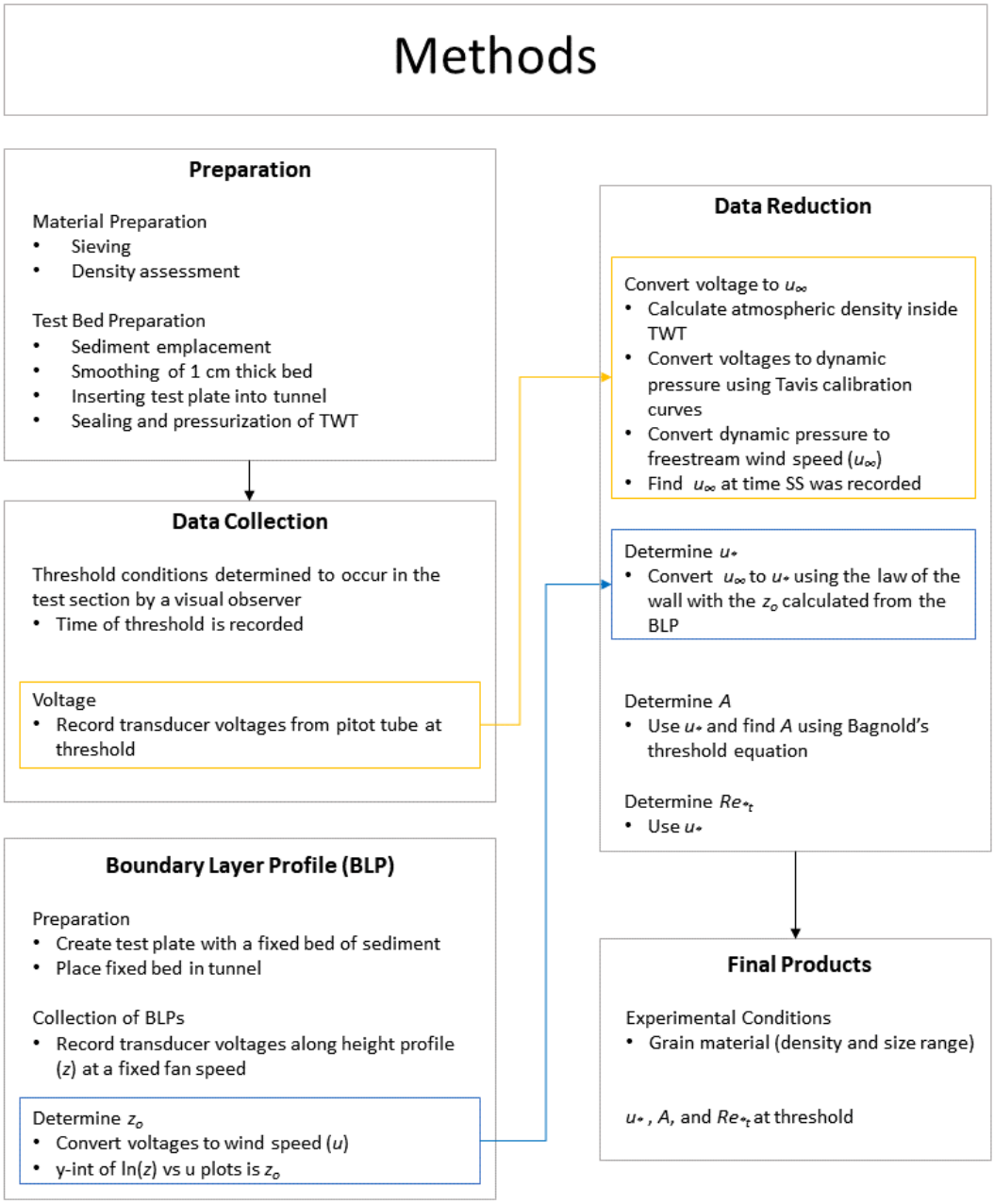


Figure 8: A flow chart outlining the generic methods used to collect and reduce the data. In order to produce all the plots given in the Results section, z_o is derived by fitting two different parts of the BLPs.

4.1 Titan Wind Tunnel

The Titan Wind Tunnel was refurbished from the Venus Wind Tunnel with the purpose of studying aeolian processes on Titan [*Burr et al.,* 2015b]. Capable under nominal conditions of reaching a pressure of 20 bar, this closed-circuit wind tunnel has a 122-cm-long test section with an interior diameter of 20.3 cm. The test section can be removed from the rest of the wind tunnel in order to set the bed with material. Two stations along the test section enable observations of the bed. The upwind observation station consists of one circular window that is 7.6 cm in diameter on the exterior of the tunnel, whereas the downwind station consists of three circular viewing ports: windows on the interior and exterior of the tunnel, both of which are 7.6 cm in diameter, and an additional port on the top (5 cm diameter) that can be used for illumination. A transverse pitot tube, used to measure wind speed, is installed in the tunnel where the downwind observation station is located, and represents a change in configuration from previous Titan Wind Tunnel use [*Burr et al.*, 2015a]. This pitot tube is connected to a custom designed transducer (used to measure voltage) that can withstand high pressures. Figure 9 is a schematic photo of the TWT with these elements labelled.

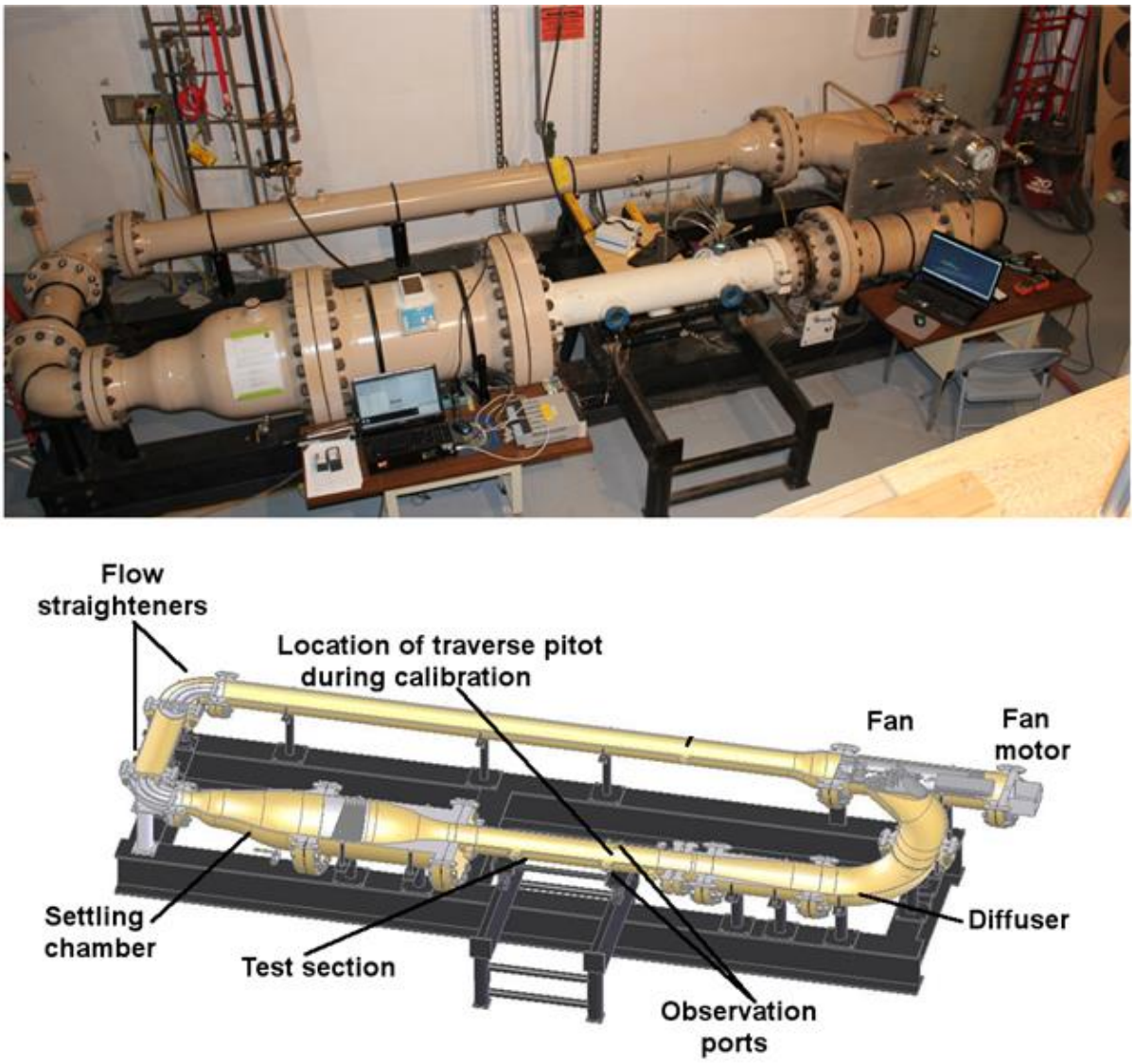


Figure 9: (top) Photograph of the Titan Wind Tunnel. (bottom) Sectioned layout of the Titan Wind Tunnel. For clarity, only the downwind observational ports are labeled, but the upwind port is visible (to the left) in the photograph. From Burr et al. [2015b].

4.2 Experimental setup

The experimental materials covered a wide range of densities and grain diameters (Table A3). This range enables comparison with past experiments, provides data that span the threshold curve (Figure 4), and overlaps as much as possible the parameter space for the density ratio from previous experiments (Figure 10).

Threshold data were collected during two different dates: 1) August 2016, and 2) March and May 2017. The August 2016 data collection involved slowly ramping up the wind speed through several stages of motion, as visually estimated by the observed, including first motion/twinkling, flurries, patches, 50% of bed in motion, 100% of bed in motion (see *Burr et al.,* 2015a, Supplemental Information, ED Table 3). As in Burr et al. 2015a, I used 50% of the bed in motion as one definition of threshold. However, I also analyze the results using patches as another definition of threshold, one that is more consistent with previous high-pressure experiments in the Venus Wind Tunnel (Greeley et al. 1984; see A2: Definitions of Experimental Threshold). The March and May 2017 date collection entailed setting the wind speed to achieve a steady-state conditions, estimated qualitatively as having the same number of grains enter the field of view (FOV) as leave it. Although the criteria for wind speeds were different during these two sets of experiments, the fan motor speeds were comparable for the 2017 and August 2016 threshold data (Table 4).

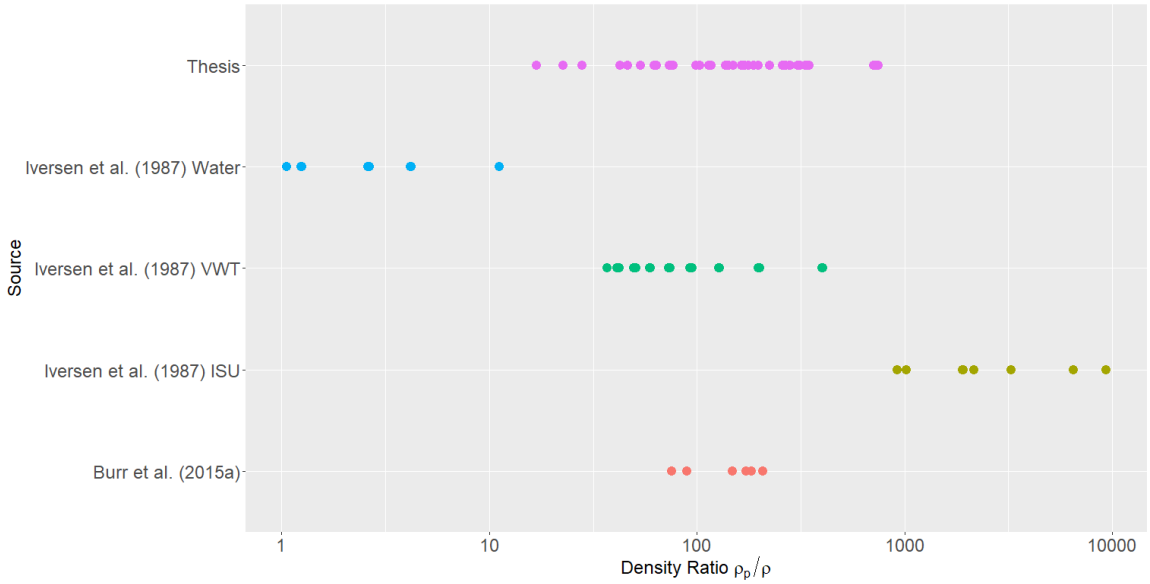


Figure 10: The spread of experimental density ratios in this thesis compared to those in previous literature. Iversen et al. [1987] includes experiments conducted in water, the Venus Wind Tunnel, and the Iowa State University Wind Tunnel. Burr et al. [2015a] experiments were conducted at the Titan Wind Tunnel.

For all data collection experiments, the experimental sediments were placed in the test section where they were smoothed into a bed of a constant thickness (1 cm). For the 2017 experiments, a trip plate was placed on the upwind section of the test plate to induce steady state conditions in the wind tunnel faster. The trip plate consisted of bolts that were evenly distributed (Figure 11c). A trip plate was not used in the 2016 experiments, but boundary layer profiles taken with and without the trip plates yield values within the same order of magnitude for the roughness heights (Figure 12). After the bed was laid down, a ruler was placed so as to be viewable through the downwind observation port and photographed for scale. The ruler was removed, and the tunnel was sealed and pressurized. The bed was then pre-conditioned by increasing the fan speed until ~50% of the bed surface was observed to be in motion, in order to provide a more natural texture to the bed and remove any perched grains.

An Edgertronic SC1 high speed video camera was positioned outside the tunnel at the side observation portal of the tunnel (Figure 11). The camera frame rate was set to 500 frames per minute (approximately 8 frames per second) with a field of view of 3.6 cm by 2 cm (1280 pixels by 720 pixels). The camera was focused on the bed under the pitot tube in the centre of the tunnel. Two snake lights were used to illuminate the bed surface for the 2016 experiments. A laser system, consisting of 5 lasers focused through a convex cylindrical lens, was placed on the top observation portal of the wind tunnel to properly

illuminate the grains with a 2-mm wide laser light sheet for the 2017 experiments (Figure 11). During each experiment, a high-pressure transducer connected to a pitot tube continually recorded voltage data as a person visually observed the bed. For the 2016 data collection, the fan speed was incrementally increased through each stage of motion [given in *Burr et al.*, 2015a] as qualitatively perceived by the observer, who recorded the time of its occurrence. For the 2017 data collection, the fan speed of the tunnel was increased until the observer estimated that steady state conditions were achieved, and the fan motor speed was held constant while high speed video captured the grains in motion for 6 seconds. After the experiments, steady state was confirmed by watching the videos and comparing the number of grains entering the frame to those leaving the frame of view. The number of grains entering and grains exiting the FOV were within 20% of each other.

The similitude boundary condition used for these threshold experiments was kinematic viscosity, consistent with previous TWT threshold work [*Burr et al.,* 2015a]. The surface atmospheric pressure on Titan is ~1.4 bar, but, given the difference in temperature between the surface of Titan and the Titan Wind Tunnel, higher pressures were necessary in order to recreate the kinematic viscosity conditions of Titan's atmosphere in the wind tunnel for current and past climates (Table 2). The experimental matrix in the Appendix lists the materials, densities, size ranges, and pressures for each experiment (Table A3).

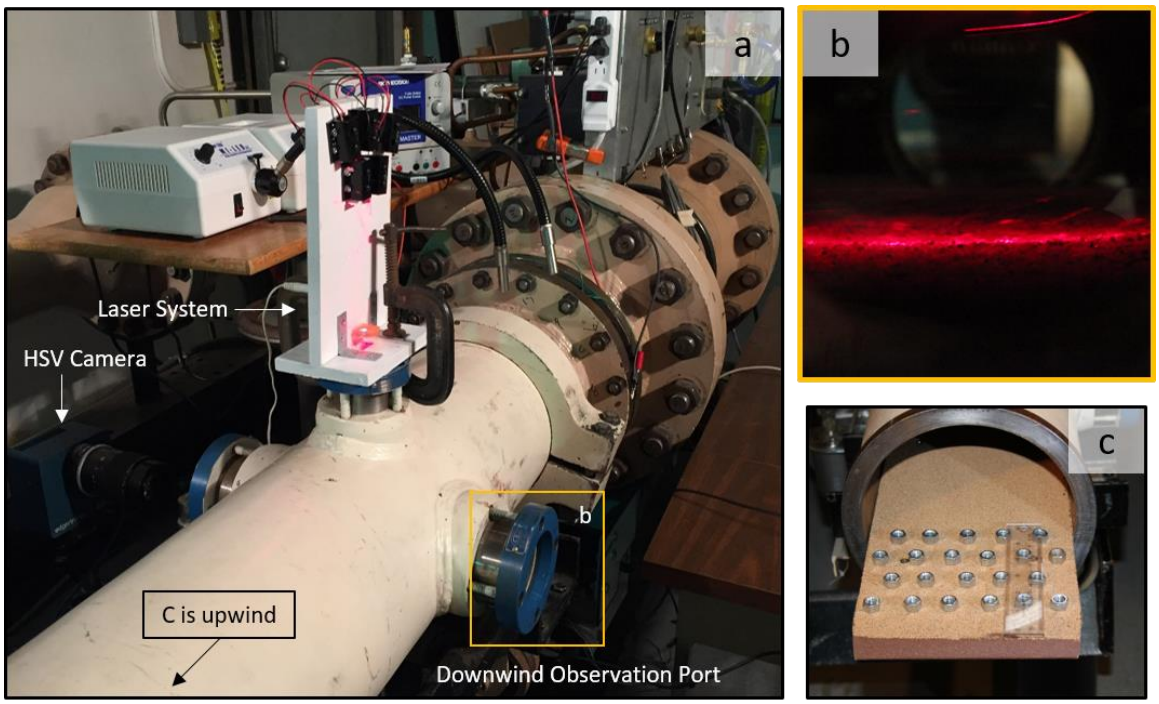


Figure 11: a) Experimental setup showing the positioning of the high-speed video (HSV) camera and the laser system used to illuminate the grains at the downwind observation portal for the 2017 experimental configuration. b) A view of the inside of the tunnel at the downwind observation port showing the laser light sheet illuminating the bed of sediment. c) Photo of the trip plate that was used to induce a steady state flow in the TWT during the 2017 experiments collected for this thesis.

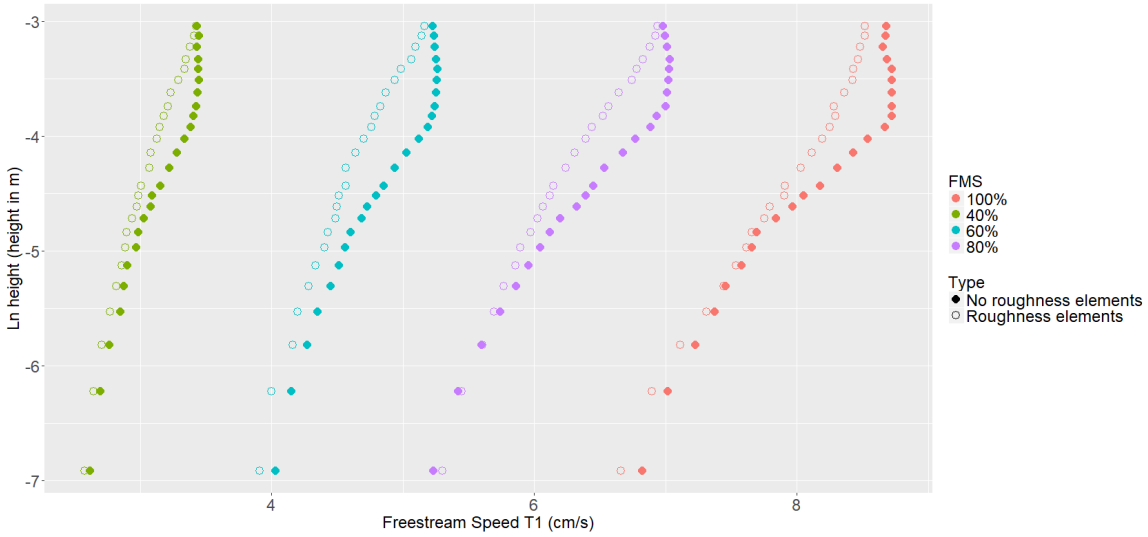


Figure 12: A comparison of boundary layer profiles for different fan motor speeds taken with and without roughness elements. Boundary layer profiles taken with and without roughness elements converge at approximately the same location, which will result in similar roughness heights.

Table 2: Conditions necessary to achieve kinematic viscosity with the Titan near-surface atmosphere. Adapted from Burr et al. [2015a].

Parameter	**Titan**	**Titan Wind Tunnel**
Atmospheric composition	~95% N_2, ~5% CH_4	~79% N_2, ~20% O_2
Static pressure, P (Pa)	1.44×10^5	1.25×10^6
Temperature, T (K)	94	293
Molecular (dynamic) viscosity, μ (Pa s)	6.25×10^{-6}	1.85×10^{-5}
Atmospheric density, ρ (kg/m^3)	5.3	14.5
Kinematic viscosity, ν (m^2/s) = μ/ρ	1.2×10^{-6}	1.2×10^{-6}

4.3 Data reduction

Data reduction began with collecting and analyzing boundary layer profiles in order to derive values to solve the Law of the Wall equation for threshold friction velocity.

4.3.1 Boundary Layer Profiles (BLPs)

The *boundary layer* is the zone where the flow velocity increases vertically from zero to freestream velocity, i.e., the zone where the velocity gradient is non-zero. This vertical gradient in velocity develops due to the viscosity of the fluid. As a fluid flows over a surface, the fluid is immobile at the adjacent stationary boundary, and, due to flow continuity, logarithmically increases in velocity with height (Figure 13) [*Shao*, 2008].

The *Law of the Wall* (also known as the Prandtl-von Kármán equation) states that the rate of increase of fluid velocity (u) with log height is proportional to the slope or rate of change of the velocity distribution curve:

$$u(z) = \frac{u_*}{\kappa} \ln\left(\frac{z}{z_o}\right) \tag{28}$$

where κ is the von Kármán constant (0.41) and z_o is the roughness height, the elevation above the bed where the wind speed is zero due to friction [*Bagnold*, 1941]. The Law of the Wall is important because it relates the freestream velocity, $u(z)$, to the friction velocity (u_*).

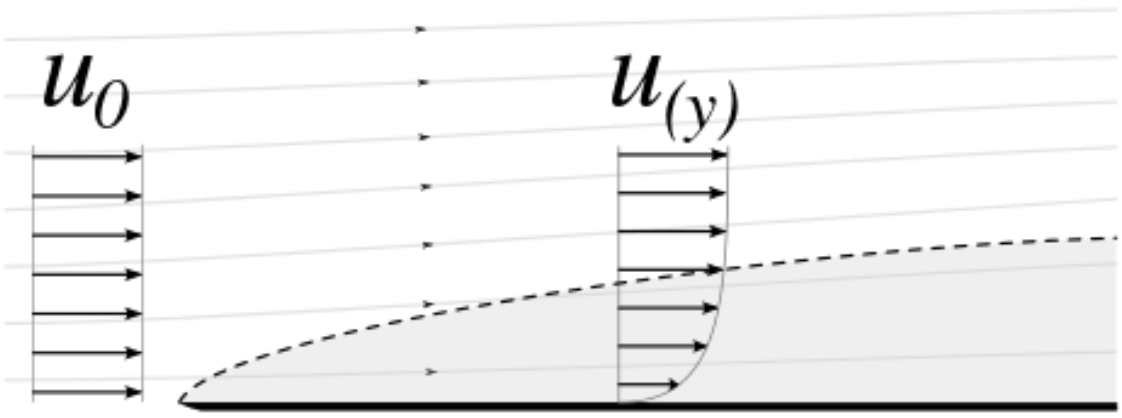


Figure 13: Boundary layer profile adapted from Shao [2008].

The roughness height (z_o) is independent of the wind velocity and all velocity profiles should converge to this value. According to Schlichting [1968], the roughness height is ~ 1/30 the mean particle diameter for rough surfaces, although this relationship varies with shape and distance between individual particles.

4.3.2 Derivation of z and z_o from Boundary Layer Profiles

Solving the Law of the Wall (Eq. 28) requires roughness heights and freestream wind speeds and heights, which I derived from boundary layer profiles. Boundary layer profiles were collected from fixed roughness beds constructed by gluing sediment onto cardstock paper. To cover the relevant experimental grain sizes while maintaining operational efficiency, three sizes of sediment were used: 400-600 µm glass beads, 500-600 µm walnut shells, and 833-1000 µm quartzo-feldspathic sand. To collect a boundary layer profile, a fixed (glued) bed was placed in the wind tunnel, the tunnel was pressurized, and the fan speed was held constant while a stepping motor moved the pitot tube through a sequence of positions within the boundary layer. The pitot tube traversed 25 positions, logarithmically spaced, from 1 mm to 48 mm above the fixed bed. Each position was held for 10 seconds while the transducer attached to the pitot tube collected voltages. At the end of each traverse, the pitot was returned in the bed, the fan speed was increased by ~10% or 25%, and another boundary layer profile was collected. The procedure was

repeated for a variety of fan motor speeds and atmospheric pressures for each of the three beds.

The voltages from the transducer are averaged over the 10 seconds that the data were collected at each of the 25 pitot tube positions that were traversed. I converted these voltages to dynamic pressures using calibration curves provided by the manufacturer. The dynamic pressure (P_{dyn}) was then converted to free stream wind speed using the following formula:

$$u(z) = \sqrt{\frac{2P_{dyn}}{\rho}}. \tag{29}$$

The Law of the Wall (Eq 28) can be linearized as:

$$\ln(z) = \frac{\kappa}{u_*}u + \ln(z_O). \tag{30}$$

According to this linearization, the freestream velocities are plotted against the logarithmic height above the bed (z) (Figure 14). A trendline for these velocities yields a y-intercept, $\ln(z_o)$, from which z_o is derived. The BLPs are not linear in log space as they have two different slopes that correspond to different regions in the BLP. The lower region corresponds to the area fit by the Law of the Wall and the upper region corresponds to the area fit by the Law of the Wake [*Bauer*, 2013]. One could fit the regression line to either the upper or lower region of the BLP (Figure 15). Fitting to the

lower region produces values of z_o between 0.1 and 5 µm, while fitting to the upper region produces values of z_o that are 1 to 2 orders of magnitude larger, between 10-20 µm. I chose to fit the upper region of the BLPs, and as a result the lowest four values are excluded when fitting the trendline. The reason for this non-linearity in log space is not clear. To see the implications of this choice in fitting region, see the possible sources of error discussed in section 7.2.2.

Multiple boundary layer profiles are recorded for each sediment size and air pressure for different fan speeds. To derive the value of z_o for each experiment, I used the average value of z_o derived from the boundary layer profiles for the closest one or two fan motor speeds to that at which threshold was observed and also the adjacent two fan motor speeds. For experiment T-17-1500, for example, the fan speed at threshold was 64%. Thus, I averaged the roughness heights at 50%, 60%, 75%, and 100% of the maximum rated fan motor speed to derive z_o for this experiment.

The height of the freestream, z, is calculated by fitting a line on the vertical portion of the boundary layer profile (the upper portion). The point of intersection of the vertical line in the freestream and the regression used to calculate the roughness height (the lower portion of the BLP) is taken to be the height of the freestream (Figure 15). To see the code used to derive z_o and z from a BLP, please refer to section A4 of the Appendix.

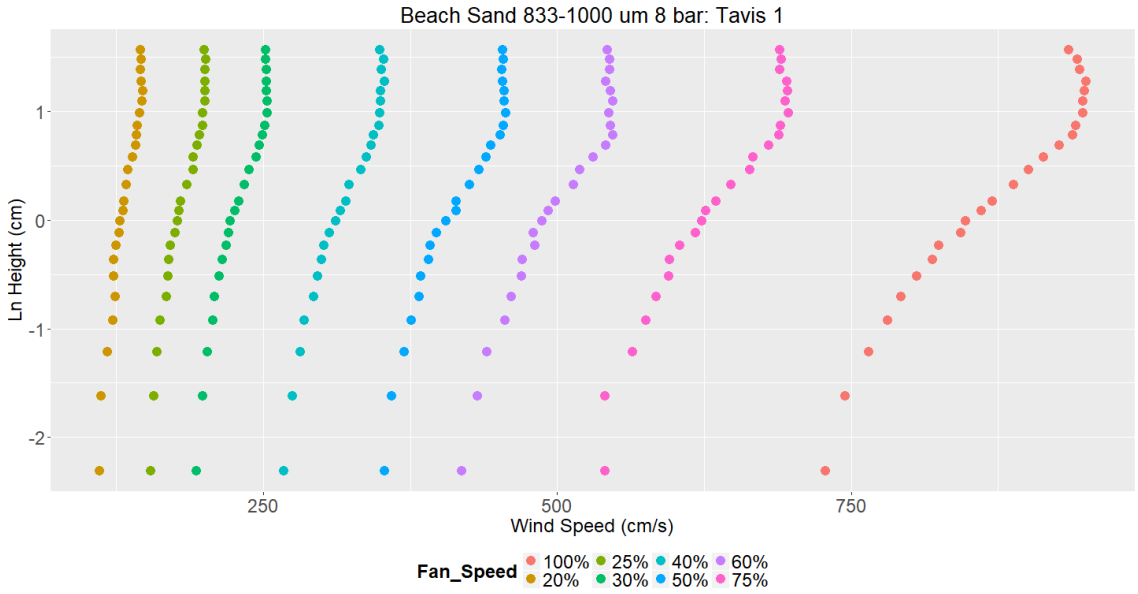


Figure 14: Boundary layer profiles for quartzo feldspathic, 833-1000 microns, at 8 bar for various fan speeds, taken without roughness elements.

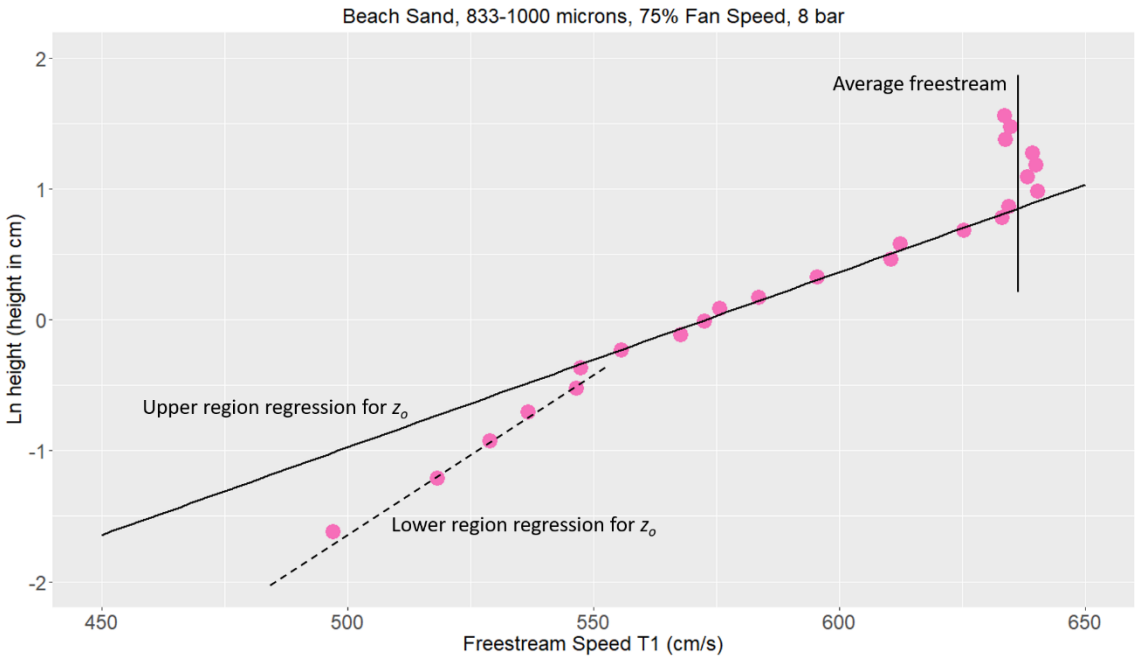


Figure 15: Derivation of parameters to solve the Law of the Wall (Eq. 28), using boundary layer profile for quartzo-feldspathic sand, 833-1000 microns, at 8 bar taken at 75% fan speed. The solid lines represent the two regressions taken to determine a) the roughness height, z_o, which is derived from the y-intercept, and b) the freestream, z, which is the point of intersection of these two lines. Two regions could be fit to derive the z_o; the solid line denotes the upper region of the BLP (used in this thesis) and the dashed line denotes the lower region of the BLP.

4.3.3 Conversion of transducer voltage data to freestream speed

The time recorded for threshold (2016 data) or steady state (2017 data) was matched to the corresponding voltage data from the transducer. This voltage was converted to a dynamic pressure that was then converted to a freestream wind speed using manufacturer calibration curves and equation 29, as described above.

The freestream speed at height z was converted to friction wind speed using the Law of the Wall (Eq. 28), along with the roughness height from the appropriate boundary layer curve. To see the code used to reduce the voltages to freestream speeds, please refer to section A5 of the Appendix.

4.4 Uncertainty analysis

I calculate total measurement uncertainties in my results for the TWT by propagating the uncertainties in the individual measurements used in calculating A. In the explanation below, I provide example values for one experiment type, 833-1000 µm walnut shells at 8 bar. Data for this experiment were collected on experiment T-17-1500. Uncertainties for the other experiments are similarly calculated (and are given in Table 4)

The freestream speed u_∞ is converted to friction wind speed (u_*) using the Law of the Wall (Eq. 28). Three variables in equation 28 affect the u_*: u_∞, z, and z_o. These three variables are independent of one another. To determine the error value of u_*, the error

values on these three variables are calculated and propagated through the Law of the Wall equation.

4.4.1 Uncertainty in freestream wind speed, $\delta u_\infty/u_\infty$

When calculating the freestream speed, u_∞, uncertainties arise due to the following (modified from *Burr et al*., 2015a):

A) Voltage as measured at the pitot at threshold. The uncertainty in the voltage recorded at the time that threshold is observed is due to two factors.

   i) Transducer uncertainty. I quantify this fractional uncertainty as the ratio of the 'Deviation (mV)' and the 'Output Voltage (VDC)' (VDC, d.c. voltage in volts) recorded in the manufacturer's transducer calibration data. The maximum fractional uncertainty over the entire range of test pressures is always ≤1%. 1% is taken as a standard, conservative value.

   ii) Voltage variability. The fractional uncertainty in the voltage variability is the standard deviation of the population divided by the average voltage. This uncertainty is calculated for the 5 seconds after threshold is observed. For experiment T-17-1500, the average voltage is 2.37 VDC, the standard deviation is 0.10 VDC and the fractional uncertainty is 0.042 or 4.2%.

Because these uncertainties in the voltage at threshold are random and independent, they are added in quadrature. For the experiment T-17-1500 for which threshold was observed, the result is 4.3%.

B) Conversion from pitot voltages to pressures. Conversion from voltage to dynamic pressure is done using the manufacturer-supplied linear calibration curves, for which the uncertainty is <0.01%. Given the linear shape of the curves and their small uncertainty, I consider this uncertainty to be negligible.

C) Conversion from pitot pressures to pitot freestream wind speeds. Dynamic pressure from the pitot tube as recorded by the transducer is converted to wind speed according to Eq. 30, where ρ is calculated using the universal gas law (as indicated in Table 2). The static pressure (P) for this calculation is measured with a precision of <0.5% using a calibrated gauge. The temperature in the wind tunnel is measured with a calibrated thermometer. Thus, the fractional uncertainty in density ($\delta\rho/\rho$) is the fractional uncertainty in the static pressure ($\delta P/P$), and is taken to be 0.5%.

The fractional uncertainty in the wind speed ($\delta u_\infty/u_\infty$) at the pitot is derived by propagating uncertainties in the dynamic pressure (P_{dyn}) and the density (ρ):

$$\frac{\delta u}{u} = \frac{1}{2}\sqrt{\left(\frac{\delta P}{P}\right)^2 + \left(\frac{\delta \rho}{\rho}\right)^2} \tag{31}$$

For experiment T-17-1500, the uncertainty value for the freestream speed ($\delta u_\infty / u_\infty$) is 2.2%.

4.4.2 Uncertainty in roughness height, $\delta z_o / z_o$

The error in z_o for a given roughness bed is a function of two factors. The first factor is the propagation of the errors in the regressions for each individual fan motor speed. This error is computed by propagating the errors of the individual regression through the averaging equation:

$$\delta(z_o)_{avg} = \frac{1}{4}\sqrt{(\delta z_{o1})^2 + (\delta z_{o2})^2 + (\delta z_{o3})^2 + (\delta z_{o4})^2} \tag{32}$$

The second source of error for any given bed is the variability among the multiple z_o values, derived at different fan motor speeds. This error, is characterized by the standard deviation of the mean:

$$\delta(z_o)_{mdev} = stdev\ of\ mean[z_{o1}, z_{o2}, z_{o3}, z_{o4}] \tag{33}$$

The total error in z_o is then calculated by adding these two independent contributions together in quadrature.

$$\delta(z_o)_{tot} = \sqrt{\delta(z_o)_{avg}{}^2 + \delta(z_o)_{mdev}{}^2} \tag{34}$$

For T-17-1500, z_o = 5.85 microns and the uncertainty in roughness height ($\delta z_o / z_o$) is 25.52%.

4.4.3 Uncertainty in Boundary Layer Height, $\delta z/z$

The average height of the boundary layer profile was found by averaging the heights of measured boundary layer profiles at different fan speeds (Section 4.3.2). The standard deviation of the measured boundary layer heights is used as the error. It is converted to a fractional uncertainty. For T-17-1500, z = 2.63 mm, the standard deviation is 0.052, and the fractional uncertainty ($\delta z/z$) is 2.42%.

4.4.4 Uncertainty in friction speed, $\delta u_*/u_*$

The errors found in the freestream velocity, the roughness height, and the boundary layer height are propagated through the Law of the Wall equation (Eq. 28) as follows:

$$\frac{\delta u_*}{u_*} = \sqrt{\left(\frac{\delta u_\infty}{u_\infty}\right)^2 + \left[\frac{\left(\frac{\delta z}{z}\right)^2 + \left(\frac{\delta z_o}{z_o}\right)^2}{\left(\ln\frac{z}{z_o}\right)^2}\right]} \tag{35}$$

For experiment T-17-1500, the fractional uncertainty for the friction speed is 6.72%.

5. Results

5.1 Overview of results

A total of 67 experiments and 134 corresponding boundary layer profiles were taken in the Titan Wind Tunnel (summaries in Table 3 and Table 4). A plot of friction speeds vs grain diameter shows that, in general, the speed increases with grain diameter for each bed material at a given atmospheric pressure (Figure 16), as expected. There are a few exceptions, however, to that general rule. For example, when the atmospheric pressure is 12.5 bar, the threshold speeds remain relatively constant across the various grain diameters, instead of increasing with size.

As the atmospheric pressure increases, the friction speed required to entrain the grains decreases (Figure 16), as expected. The denser materials (ex. basalt, 3000 kg/m^3) have a higher wind speed than the least dense materials (ex. walnut shells, 1100 kg/m^3).

Table 3: Summary of boundary layer profile results and the resulting z_o and z from each BLP. FMS indicates fan motor speed.

Experimental Parameters			Reduction	Results		
Material and Size (microns)	Pressure (bar)	FMS	Regression Range zo (cm)	z_o (um)	z_o Fractional Uncertainity	z (cm)
Glass Beads 400-600 µm	1	60	.79 to 2.2	12.16	13.4	2.56
		75	.69 to 2	2.46	24.3	2.34
		100	.89 to 2	2.14	46.0	2.57
	3	40	.89 to 2	23.08	41.2	2.19
		50	.89 to 1.8	7.57	26.7	2.23
		60	.69 to 2	6.12	22.4	2.44
	8	40	.79 to 2	3.04	48.3	2.29
		50	.79 to 2	11.71	41.7	2.18
		60	.69 to 1.6	3.14	68.1	2.38
		75	.7 to 1.8	10.80	44.9	2.11
		100	.6 to 1.8	3.55	18.4	2.15
	12.5	25	.6 to 1.8	7.08	45.0	2.23
		30	.7 to 1.8	9.26	49.1	2.10
		40	.69 to 1.6	2.52	68.8	2.27
		50	.6 to 1.8	5.05	46.4	2.19
		60	.59 to 2	2.48	36.4	2.22
	15	30	.7 to 1.8	6.73	67.9	2.25
		40	.69 to 1.8	5.52	33.0	2.07
		50	.79 to 1.8	5.17	26.9	2.07
		60	.69 to 1.8	2.15	24.1	2.11
	20	40	.79 to 1.8	6.63	39.8	2.13
		50	.69 to 1.6	3.78	47.5	2.03
		60	.69 to 1.8	2.11	19.3	2.11
Quartz Sand 500-600 µm	3	60	.7 to 1.8	6.68	21.3	2.56
		75	.7 to 2	5.70	20.8	2.39
		100	.8 to 2.2	6.61	15.9	2.26
	8	50	.69 to 2	4.05	49.8	2.42
		60	.79 to 2	8.92	51.6	2.31
		75	.79 to 1.8	6.15	47.9	2.30
		100	.8 to 2.2	2.91	18.3	2.30
	12.5	50	.6 to 1.8	8.56	31.8	2.22
		60	.7 to 2	7.52	22.6	2.09
		75	.8 to 1.8	2.82	21.2	2.25
		100	.8 to 2.2	2.54	10.6	2.29
	15	50	.7 to 1.8	6.57	28.0	1.99
		60	.7 to 1.6	3.00	10.7	2.16
		75	.7 to 1.8	2.53	31.4	2.15

Table 3 continued

Experimental Parameters			Reduction	Results		
Material and Size (microns)	Pressure (bar)	FMS	Regression Range zo (cm)	z_o (um)	z_o Fractional Uncertainity	z (cm)
Quartzofeldspathic Sand 833-1000 µm	3	50	.6 to 1.8	18.00	30.2	2.55
		60	.5 to 2.2	14.07	24.2	2.62
		75	.6 to 2	8.39	37.6	2.61
		100	.6 to 2	4.62	31.9	2.55
	8	50	.8 to 2	9.27	34.0	2.31
		60	.6 to 1.8	5.45	48.9	2.29
		75	.7 to 2	4.64	34.0	2.39
		100	.7 to 2	4.23	18.5	2.38
	12.5	40	.7 to 2	3.82	54.1	2.40
		50	.7 to 2	3.83	50.3	2.44
		60	.7 to 2	7.09	32.7	2.33
		75	.8 to 1.8	5.67	37.0	2.18
		100	.7 to 2	4.96	10.2	2.20
	15	40	.6 to 1.8	6.86	27.1	2.14
		50	.7 to 1.8	5.34	34.0	2.28
		60	.7 to 2	3.78	25.7	2.28
		75	.7 to 1.8	4.46	34.7	2.17
	20	30	.6 to 2.2	8.39	30.1	2.27
		40	.7 to 2	4.90	21.9	2.34
		50	.7 to 2	4.49	16.5	2.33
		60	.8 to 2	3.69	32.8	2.24
		75	.7 to 2	3.88	25.5	2.12

Table 4: Summary table of the threshold experiments displaying the experimental parameters, the freestream speed at threshold, the boundary layer profiles used to convert freestream to friction speed, the Reynold's friction number, and the dimensionless threshold parameter, *A*. Note that QF stands for quartzo-feldspathic.

Experimental Parameters			Measurements at Threshold			Boundary Layer Profiles						Results			
Material and Size Range	Experiment Number	Desired Pressure (bar)	Free Stream Speed (m/s) u_∞	$\delta u_\infty / u_\infty$	Max Fan Speed (%)	BLPs used to convert u_∞ to u_*	BLP Fan Speeds % Used	Roughness Element z_o (m)	$\delta z_o / z_o$	Freestream Height z (m)	$\delta z / z$	u_* (m/s)	Re_{*t}	A	$\delta u_* / u_*$
Walnut Shells 833-1000 µm	T-16-1298	3	7.74	2.93	97	Beach Sand, 833-1000 µm, 3 bar	60, 75, 100	9.03E-06	55.67	0.025	12.65	0.27	13.5	0.16	9.47
	T-16-1297	8	4.80	9.10	61.9	Beach Sand, 833-1000 µm, 8 bar	50, 60, 75	6.45E-06	44.65	0.026	5.11	0.19	9.2	0.18	14.96
	T-16-1296	12.5	4.02	8.46	49.5	Beach Sand, 833-1000 µm, 12.5 bar	40, 50, 60	4.91E-06	45.71	0.025	15.64	0.12	6.1	0.15	14.04
	T-16-1295	15	3.59	9.52	43.5	Beach Sand, 833-1000 µm, 15 bar	40, 50, 60	5.33E-06	33.72	0.024	1.44	0.18	8.7	0.24	14.52
	T-16-1294	20	3.01	12.12	35.2	Beach Sand, 833-1000 µm, 20 bar	30, 40, 50	5.93E-06	39.51	0.024	4.50	0.12	5.8	0.18	13.84
Walnut Shells 833-1000 µm	T-17-1501	3	7.63	2.96	105.5	Beach Sand, 833-1000 µm, 3 bar	60, 75, 100	9.03E-06	55.67	0.026	1.46	0.39	19.6	0.23	14.77
	T-17-1500	8	4.88	4.78	64.1	Beach Sand, 833-1000 µm, 8 bar	60, 75, 100	4.77E-06	25.82	0.024	2.42	0.24	11.7	0.23	6.39
	T-17-1499	12.5	3.79	6.60	51.4	Beach Sand, 833-1000 µm, 12.5 bar	50, 60, 75	5.53E-06	36.93	0.023	5.62	0.19	9.2	0.23	9.30
	T-17-1498	15	3.70	6.80	45.8	Beach Sand, 833-1000 µm, 15 bar	40, 50, 60	5.33E-06	33.72	0.023	3.59	0.18	9.0	0.24	8.96
Walnut Shells 707-833 µm	T-17-1514	3	6.04	4.34	102.2	Beach Sand, 833-1000 µm, 3 bar	60, 75, 100	9.03E-06	55.67	0.026	1.46	0.31	13.1	0.20	14.96
	T-17-1513	8	4.29	3.84	62.3	Beach Sand, 833-1000 µm, 8 bar	50, 60, 75	6.45E-06	44.65	0.023	2.33	0.21	9.0	0.23	9.83
	T-17-1512	12.5	3.51	7.34	48.4	Beach Sand, 833-1000 µm, 12.5 bar	40, 50, 60	4.91E-06	45.71	0.024	2.23	0.17	7.0	0.23	12.08
	T-17-1511	15	3.26	7.61	44	Beach Sand, 833-1000 µm, 15 bar	40, 50, 60	5.33E-06	33.72	0.023	3.59	0.16	6.6	0.23	9.70
Walnut Shells 500-600 µm	T-17-1497	3	4.91	8.06	81.5	Beach Sand, 833-1000 µm, 3 bar	60, 75, 100	9.03E-06	55.67	0.026	1.46	0.25	7.6	0.20	16.78
	T-17-1496	8	3.46	10.27	51.2	Beach Sand, 833-1000 µm, 8 bar	50, 60, 75	6.45E-06	44.65	0.023	2.33	0.17	5.2	0.22	13.60
	T-17-1495	12.5	3.26	10.70	43.8	Beach Sand, 833-1000 µm, 12.5 bar	40, 50, 60	4.91E-06	45.71	0.024	2.23	0.16	4.7	0.25	13.57
	T-17-1494	15	3.26	9.59	42.4	Beach Sand, 833-1000 µm, 15 bar	40, 50, 60	5.33E-06	33.72	0.023	3.59	0.16	4.7	0.28	11.51
Walnut Shells 175-250 µm	T-17-1503	12.5	2.15	44.74	31.8	Glass Beads, 400-600 µm, 12.5 bar	25, 30	8.17E-06	29.52	0.022	4.15	0.11	1.3	0.29	15.06
	T-17-1502	15	1.98	13.92	28.9	Glass Beads, 400-600 µm, 15 bar	30, 40, 50	5.81E-06	32.57	0.021	4.81	0.10	1.1	0.28	15.21
QF Sand 833-1000 µm	T-16-1328	8	7.30	3.96	88	Beach Sand, 833-1000 µm, 8 bar	60, 75, 100	4.77E-06	25.82	0.024	2.42	0.35	17.5	0.23	5.94
	T-16-1327	12.5	5.98	2.79	69.2	Beach Sand, 833-1000 µm, 12.5 bar	60, 75, 100	5.91E-06	25.60	0.022	3.75	0.30	14.7	0.24	5.90
	T-16-1326	15	5.15	3.54	59.8	Beach Sand, 833-1000 µm, 15 bar	50, 60, 75	4.52E-06	18.95	0.022	2.87	0.25	12.3	0.22	4.97
	T-16-1325	20	4.49	3.08	51.3	Beach Sand, 833-1000 µm, 20 bar	50, 60, 75	4.02E-06	17.72	0.022	4.65	0.21	10.5	0.22	4.08
QF Sand 833-1000 µm	T-17-1516	12.5	5.85	3.73	94.2	Beach Sand, 833-1000, 12.5 bar	60, 75, 100	5.91E-06	25.60	0.022	3.75	0.29	14.4	0.24	6.15
	T-17-1515	15	5.42	2.09	82	Beach Sand, 833-1000, 15 bar	50, 60, 75	4.52E-06	18.95	0.022	2.87	0.26	12.9	0.23	3.99
QF Sand 707-833 µm	T-17-1520	8	6.45	3.48	100.8	Beach Sand , 833-1000, 8 bar	60, 75, 100	4.77E-06	29.21	0.023	0.21	0.33	13.8	0.23	15.04
	T-17-1519	12.5	5.87	2.85	88.2	Beach Sand, 833-1000, 12.5 bar	60, 75, 100	5.91E-06	66.68	0.022	4.71	0.28	11.7	0.25	12.29
	T-17-1518	15	4.95	3.80	72.1	Beach Sand, 833-1000, 15 bar	50, 60, 75	4.52E-06	57.24	0.021	4.60	0.24	9.8	0.23	10.94
QF Sand 600-707 µm	T-17-1523	8	5.84	3.77	88.5	Quartz Sand, 500-600, 8 bar	60, 75, 100	7.54E-06	29.21	0.023	0.21	0.30	10.6	0.23	15.41
	T-17-1522	12.5	5.04	3.21	71.4	Quartz Sand, 500-600, 12.5 bar	60, 75, 100	4.29E-06	66.68	0.022	4.71	0.24	8.5	0.23	12.25
	T-17-1521	15	4.64	2.92	65	Quartz Sand, 500-600, 15 bar	50, 60, 75	8.04E-06	57.24	0.021	4.60	0.22	7.8	0.23	9.98

Table 4 continued

Experimental Parameters			Measurements at Threshold			Boundary Layer Profiles						Results			
Material and Size Range	Experiment Number	Desired Pressure (bar)	Free Stream Speed (m/s) u_∞	$\delta u_\infty / u_\infty$	Max Fan Speed (%)	BLPs used to convert u_∞ to u_*	BLP Fan Speeds % Used	Roughness Element z_o (m)	$\delta z_o / z_o$	Freestream Height z (m)	$\delta z / z$	u_* (m/s)	Re_{*t}	A	$\delta u_* / u_*$
QF Sand 500-600 µm	T-17-1531	8	5.33	3.92	78.4	Quartz Sand, 500-600 µm, 8 bar	60, 75, 100	7.54E-06	29.21	0.023	0.21	0.27	8.1	0.23	15.58
	T-17-1530	12.5	4.65	3.82	62.9	Quartz Sand, 500-600 µm, 12.5 bar	50, 60, 75	8.04E-06	16.18	0.022	3.75	0.24	7.2	0.25	4.33
	T-17-1529	15	4.31	3.76	57.4	Quartz Sand, 500-600 µm, 15 bar	50, 60, 75	4.03E-06	57.24	0.021	4.60	0.21	6.1	0.24	10.21
Basalt 707-1000 µm	T-17-1535	8	7.19	2.74	101.7	Beach Sand , 833-1000, 8 bar	60, 75, 100	4.77E-06	25.82	0.024	2.42	0.35	16.1	0.20	5.44
	T-17-1534	12.5	5.54	3.25	73.5	Beach Sand, 833-1000, 12.5 bar	60, 75, 100	5.91E-06	25.60	0.022	3.75	0.28	12.7	0.20	5.85
	T-17-1533	15	4.79	3.73	62.9	Beach Sand, 833-1000, 15 bar	50, 60, 75	4.52E-06	18.95	0.022	2.87	0.23	10.6	0.18	4.40
Basalt 500-707 µm	T-17-1538	8	5.41	4.03	76.2	Quartz Sand, 500-600 µm, 8 bar	50, 60, 75	6.38E-06	44.65	0.023	2.33	0.27	8.9	0.19	10.78
	T-17-1537	12.5	4.54	3.23	59.7	Quartz Sand, 500-600 µm, 12.5 bar	50, 60, 75	8.04E-06	36.93	0.023	5.62	0.22	7.3	0.19	6.84
Basalt 500-707 µm	T-16-1345	8	5.09	4.69	65	Quartz Sand, 500-600 µm, 8 bar	50, 60, 75	6.38E-06	48.95	0.024	7.75	0.18	6.0	0.13	15.73
	T-16-1344	12.5	4.11	6.44	51.1	Quartz Sand, 500-600 µm, 12.5 bar	50, 60, 75	8.04E-06	16.18	0.025	0.00	0.18	5.8	0.16	10.45
Charcoal 250-300 µm	T-16-1356	1	4.65	3.37	87.8	Glass Beads, 400-600 µm, 1 bar	60, 75, 100	1.22E-05	5.47	0.025	5.29	0.25	3.8	0.27	3.47
	T-16-1355	3	2.56	14.29	42.3	Glass Beads, 400-600 µm, 3 bar	40, 50, 60	1.23E-05	81.21	0.023	6.00	0.14	2.1	0.25	21.91
	T-16-1354	8	1.85	5.58	25.2	Glass Beads, 400-600 µm, 8 bar	40, 50, 60	7.43E-06	85.02	0.023	6.19	0.09	1.4	0.28	16.82
	T-16-1353	12.5	1.60	3.90	21.2	Glass Beads, 400-600 µm, 12.5 bar	40, 50, 60	3.35E-06	53.43	0.022	1.73	0.07	1.1	0.28	11.40
	T-16-1352	15	1.46	3.11	18.7	Glass Beads, 400-600 µm, 15 bar	40, 50, 60	4.28E-06	47.07	0.021	1.20	0.07	1.0	0.29	11.23
	T-16-1351	20	1.31	2.32	16.7	Glass Beads, 400-600 µm, 20 bar	40, 50, 60	4.17E-06	60.53	0.021	2.73	0.06	0.9	0.30	12.03
Charcoal 425-500 µm	T-16-1374	1	5.37	3.42	97.3	Glass Beads, 400-600 µm, 1 bar	60, 75, 100	1.22E-05	5.47	0.025	5.29	0.29	7.3	0.24	3.60
	T-16-1373	3	3.09	6.28	49.5	Glass Beads, 400-600 µm, 3 bar	40, 50, 60	1.23E-05	81.21	0.023	6.00	0.17	4.2	0.24	17.70
	T-16-1372	8	2.23	23.98	29.9	Glass Beads, 400-600 µm, 8 bar	40, 50, 60	7.43E-06	85.02	0.023	6.19	0.11	2.9	0.37	28.59
	T-16-1371	12.5	2.02	12.99	25.5	Glass Beads, 400-600 µm, 12.5 bar	40, 50, 60	3.35E-06	53.43	0.022	1.73	0.09	2.4	0.27	16.74
	T-16-1370	15	1.72	5.34	22.2	Glass Beads, 400-600 µm, 15 bar	40, 50, 60	4.28E-06	47.07	0.021	1.20	0.08	2.1	0.27	12.56
	T-16-1369	20	1.49	2.90	18.7	Glass Beads, 400-600 µm, 20 bar	40, 50, 60	4.17E-06	60.53	0.021	2.73	0.07	1.8	0.27	11.74
Charcoal 600-707 µm	T-16-1392	1	5.74	2.36	101.9	Glass Beads, 400-600 µm, 1 bar	60, 75, 100	1.22E-05	5.47	0.025	5.29	0.31	11.1	0.22	2.67
	T-16-1391	3	3.62	3.88	55.8	Glass Beads, 400-600 µm, 3 bar	40, 50, 60	1.23E-05	81.21	0.023	6.00	0.20	7.0	0.23	17.26
	T-16-1390	8	2.76	20.77	35.2	Glass Beads, 400-600 µm, 8 bar	40, 50, 60	7.43E-06	85.02	0.023	6.19	0.14	5.0	0.27	25.82
	T-16-1389	12.5	2.20	27.69	28.1	Glass Beads, 400-600 µm, 12.5 bar	40, 50, 60	3.35E-06	53.43	0.022	1.73	0.10	3.6	0.25	29.26
	T-16-1388	15	2.00	10.06	25.3	Glass Beads, 400-600 µm, 15 bar	40, 50, 60	4.28E-06	47.07	0.021	1.20	0.10	3.4	0.26	15.10
	T-16-1387	20	1.75	5.27	21.6	Glass Beads, 400-600 µm, 20 bar	40, 50, 60	4.17E-06	60.53	0.021	2.73	0.08	2.9	0.26	12.71
Glass Beads 300-600 µm	T-17-1527	8	4.84	3.52	69	Glass Beads, 400-600, 8 bar	60, 75, 100	3.24E-06	28.76	0.023	4.38	0.22	5.5	0.21	5.45
	T-17-1526	12.5	4.41	3.53	59.8	Glass Beads, 400-600, 12.5 bar	40, 50, 60	3.35E-06	53.43	0.022	1.73	0.21	5.0	0.24	11.33
	T-17-1525	15	3.87	4.54	52.4	Glass Beads, 400-600, 15 bar	40, 50, 60	4.28E-06	47.07	0.021	1.20	0.19	4.5	0.24	12.42
Plastic Chips (LPDE) 606-833 µm	T-17-1543	3	6.87	3.96	103.2	Beach Sand, 833-1000, 3 bar	60, 75, 100	9.03E-06	55.67	0.026	1.46	0.35	13.9	0.26	14.86
	T-17-1542	8	4.33	4.57	62.2	Beach Sand , 833-1000, 8 bar	60, 75, 100	4.77E-06	25.82	0.024	2.42	0.21	8.1	0.25	6.19
	T-17-1541	12.5	3.76	6.78	49.8	Beach Sand, 833-1000, 12.5 bar	40, 50, 60	4.91E-06	45.71	0.024	2.23	0.18	7.0	0.27	11.19
	T-17-1540	15	3.49	6.37	45.6	Beach Sand, 833-1000, 15 bar	40, 50, 60	5.33E-06	33.72	0.023	3.59	0.17	6.6	0.28	9.20

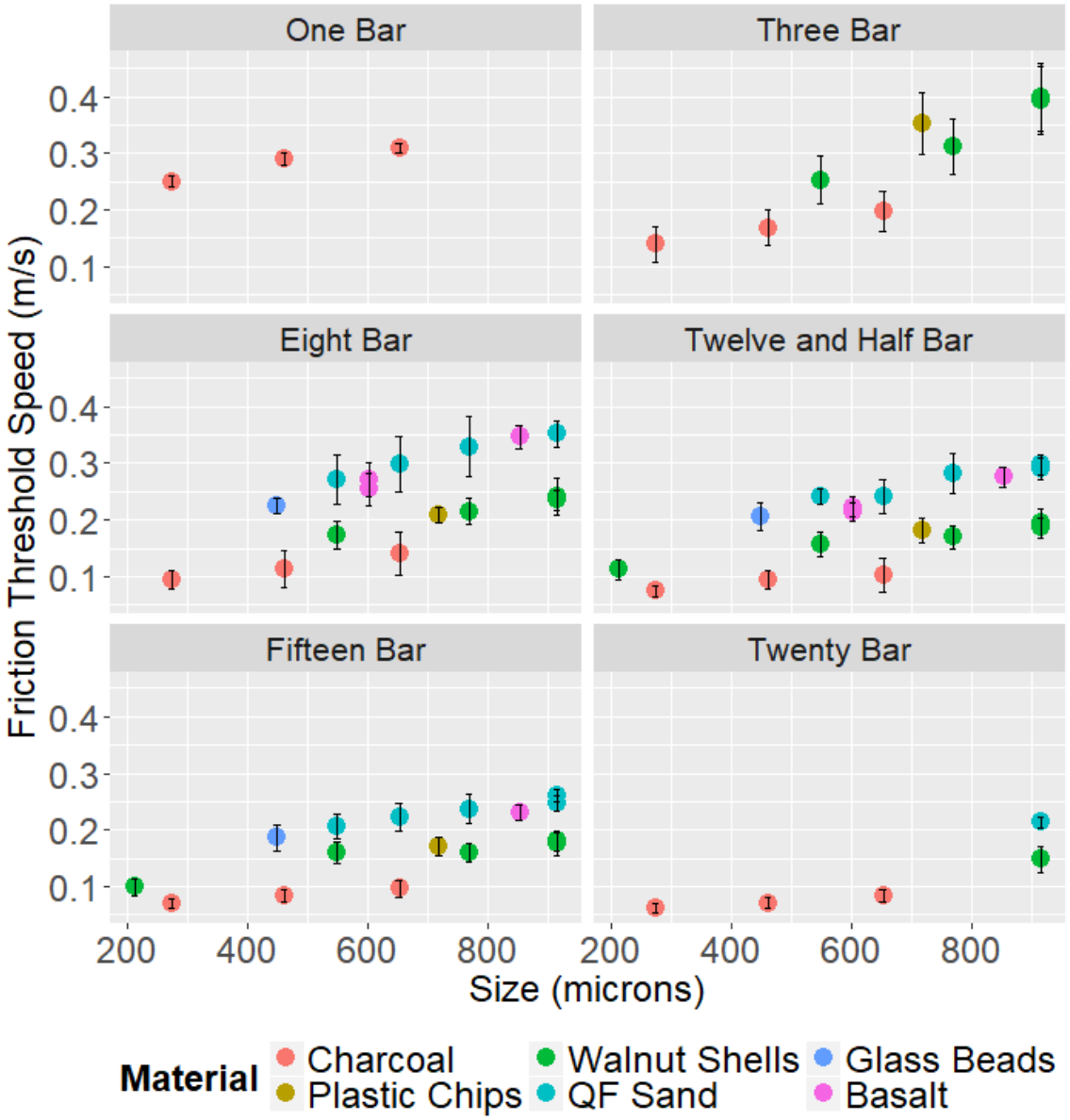


Figure 16: Experimental threshold speeds from the TWT experiments performed for this thesis, plotted as a function of grain diameter. The graphs are subdivided by the atmospheric pressure for each experiment. QF refers to a quartzo-feldspathic composition.

5.2 Dimensionless threshold parameter, *A*, as a function of density ratio

In order to recreate the dimensionless threshold parameter (*A*) expression with the inclusion of the density ratio term [$f(\rho_p/\rho)$] proposed by Iversen et al. [1987] (section 2.3), I applied the same criteria they used – $D_p > 200$ µm, and $Re_{*t} > 10$ – to filter the data in this thesis. The first criterion was met by only using bed materials with an average grain diameter larger than 200 µm. To meet the second criterion, the threshold parameter, *A,* is plotted as a function of particle Reynolds number for various atmospheric pressures (Figure 17), thus recreating the plot of Iversen et al. [1987], their Figure 3. Out of the 67 experiments conducted for this thesis, 19 of them had Reynolds numbers greater than 10. The values of density ratio vs *A* are plotted for these 19 experiments along with the experiments in Iversen et al. [1987] and Burr et al. [2015a] (Figure 18) that match the same two criteria. These experimental results do not overlap the density ratio curve within their error bars (Figure 18). Likewise, the previous TWT data points, with two exceptions, also do not fit the density ratio curve.

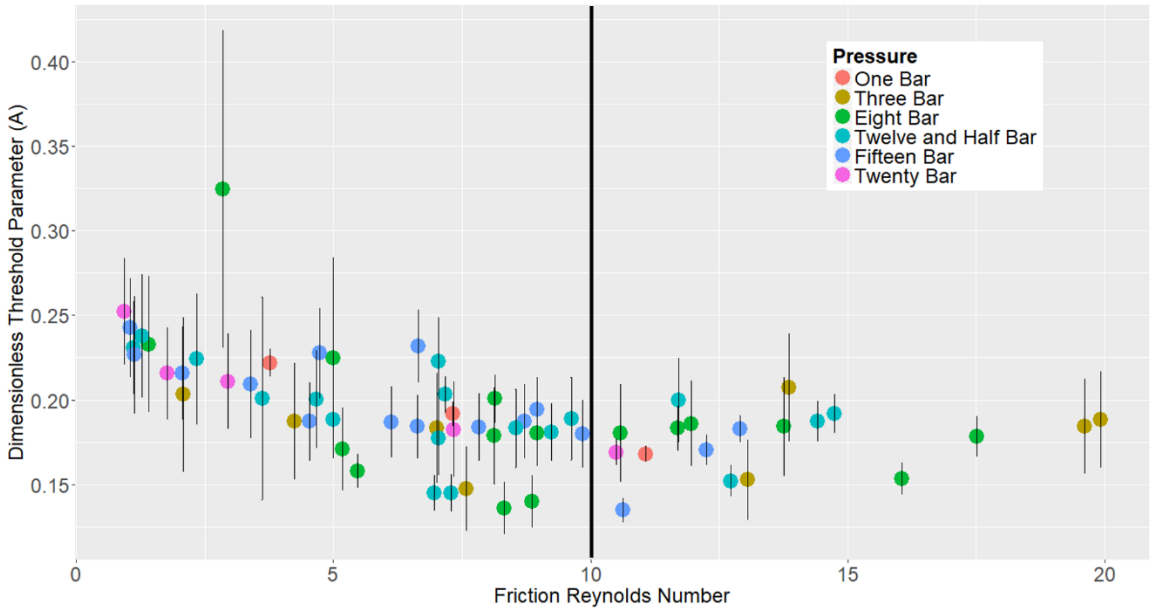


Figure 17: Threshold parameter *A* plotted as a function of particle Reynolds number for various atmospheric pressures. This plot shows how the friction Reynolds number is no longer dependent on *A* after approximately Re_{*t}>10, This graph only includes data collected in this work and does not include the Burr et al. [2015a] data collected in the TWT. The reason for the anomaly at ~ Re_{*t}=3 is unknown.

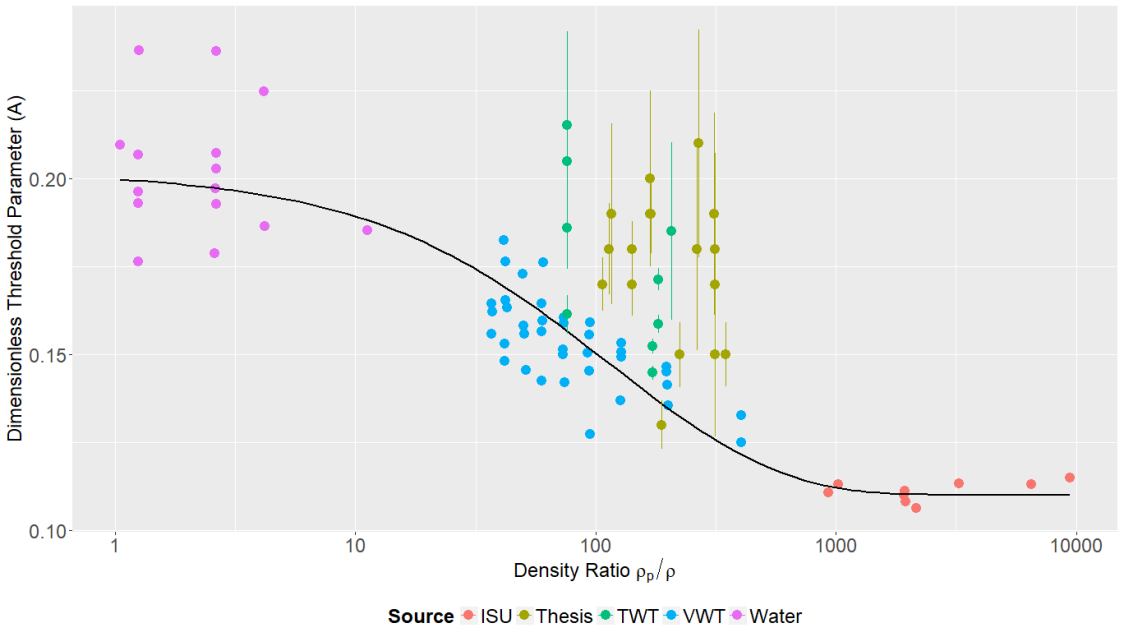


Figure 18: Threshold parameter *A*, derived from various sources, plotted as a function of the density ratio for various fluids for particles >200 µm diameter and Re_{*t} >10. Adapted from Iversen et al. [1987], with their density ratio curve overlaid on top of the data. A subset of data for the same filtering conditions collected from the Titan Wind Tunnel [*Burr et al*., 2015a] is also plotted and shown not to fit the curve. Previously published data did not include error bars.

To explore the effect that grain size may have on the density ratio curve, the Titan Wind Tunnel data from this thesis and from Burr et al. [2015a] are plotted as a function of average grain size (Figure 19). The plot shows that in general, smaller grain sizes lie closer to the density ratio curve than larger grain diameters, although exceptions are apparent. This tendency might be a partial explanation for the lower values for *A* from the earlier VWT than from the TWT, as the earlier work had maximum grain sizes of 776 µm [*Greeley et al*., 1984] whereas the latter used grain sizes ranging up to 1000 µm. However, the lack of more specific information about grain size in the VWT work prevents decisive investigation of grain size effects.

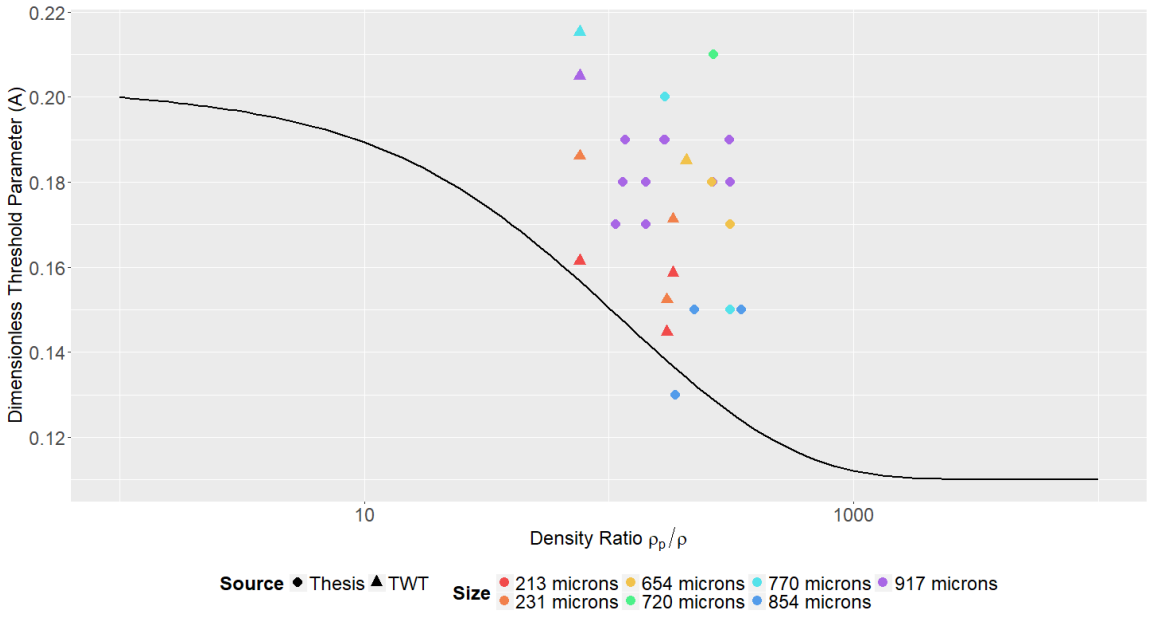


Figure 19: Values for the threshold parameter *A*, derived from TWT experiments, plotted as a function of the density ratio for particles > 200 µm diameter and Re_{*t} >10 sorted by grain size. Adapted from Iversen et al. [1987], with their density ratio curve also shown. The data collected previously from the Titan Wind Tunnel [*Burr et al*., 2015a] are marked by triangles. Smaller grains tend to lie closer to the curve than larger grains, but exceptions (e.g., the two 854 micron grains) are apparent.

6. Analysis

As shown in Figure 18, the data from the TWT do not align with the model for *A* derived by Iversen et al. [1987]. This mismatch leads me to reject the null hypothesis – that the density ratio expression derived by Iversen et al. [1987] is correct – and to accept the alternate hypothesis that the density ratio expression derived by Iversen et al. [1987] is incorrect. With the additional data from Burr et al. [2015a] and this thesis, a new expression for *A* can now be derived.

Section 2.4 describes the derivation for the *A* expression as calculated by Iversen et al. [1987]. Because the new data are consistent with a sigmoidal expression for *A* (Figure 18), I will use the Iversen et al. [1987] derivation as a starting point to derive a new expression for *A*. Eq. 20 shows the general sigmoidal expression.

The upper and lower limits of the sigmoidal expression are still 0.2 for liquid water, low density ratios, and 0.11 for terrestrial conditions, high density ratios, as derived by Iversen et al. [1987] and Bagnold [1941] respectively. The expression for *A* has the same form as Eq. 26. The data are plotted in MATLAB 2017b and the curve fitting toolbox is used to derive the values for γ and λ in Eq. 26 using the least squares fitting methodology. Errors were included as weights for the TWT data. The new best fit expression for *A* includes the constants γ =0.0032 and λ=0.89. Eq. 26 is now updated to be

$$A = \frac{0.2}{\sqrt{\left(1 + 2.3\left\{1 - e^{\left[-0.0032(\rho_p/\rho - 1)^{0.89}\right]}\right\}\right)}}. \tag{36}$$

The data are plotted with the new curve for *A* in Figure 20. As shown on Figure 20, the TWT data are a distinct population from the VWT, suggesting some systematic difference in data collection or boundary conditions. Accordingly, I also plot on Figure 20 the curve for just the TWT data. The formula for the curve fit to the TWT data alone is

$$A = \frac{0.2}{\sqrt{\left(1 + 2.3\left\{1 - e^{\left[-0.0009(\rho_p/\rho - 1)^{0.97}\right]}\right\}\right)}}. \tag{37}$$

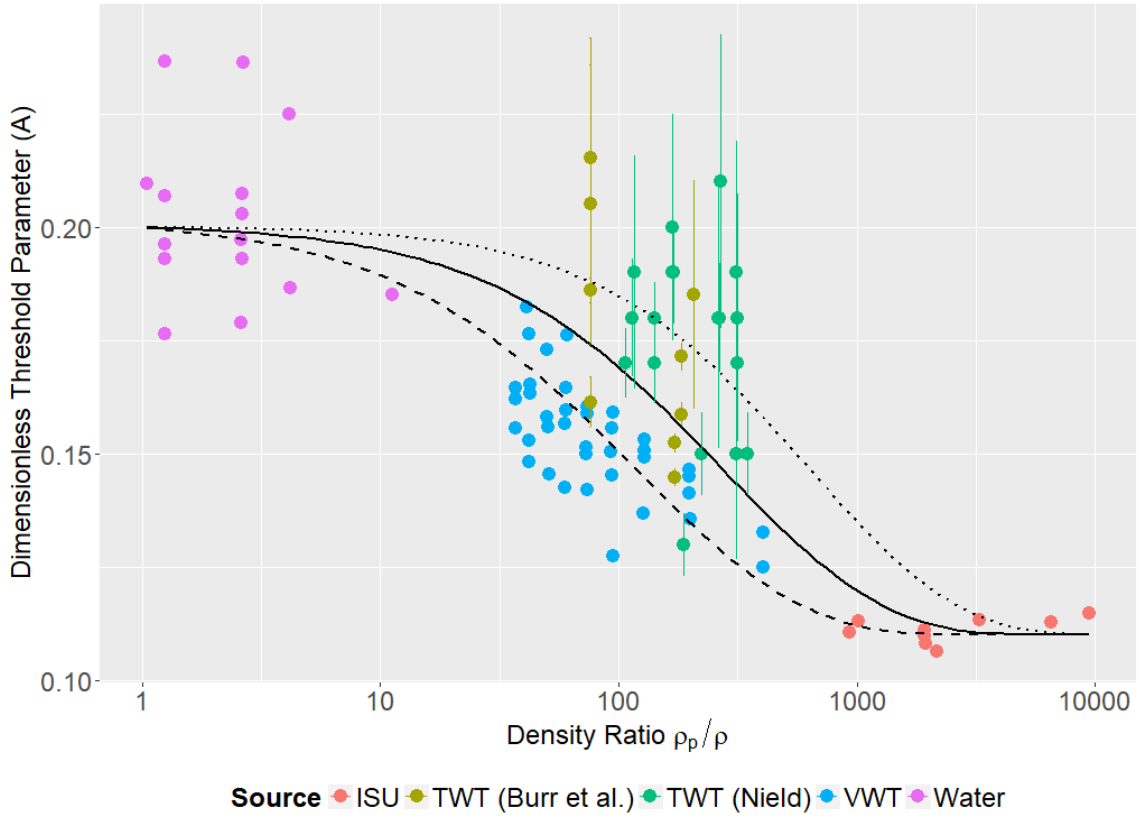


Figure 20: Threshold parameter *A* plotted as a function of the density ratio for various fluids for particles >200 µm diameter and Re_{*t} >10. Adapted from Iversen et al. [1987] (dashed curve). A subset of data for the same filtering conditions collected from the Titan Wind Tunnel [*Burr et al.*, 2015a] is also plotted along with the data collected for this thesis. The density ratio curve overlaid on top is derived in this thesis from both VWT and TWT data (solid curve). The density ratio curve derived using only TWT data is also overlaid on the graph (dotted curve). The definition of threshold for this plot is 50% bed motion.

7. Discussion

The motivation for this thesis was to answer the question about why the threshold results from Burr et al. [2015] did not align with the density ratio curve (Figure 4). In the results section, I showed that additional threshold speed data derived in Titan Wind Tunnel for this thesis also do not align with the density ratio curve of Iversen et al. [1987] within measurement uncertainties (Figure 18). Here, I discuss other, systematic, possible sources of error. These errors influence the threshold results and will change the newly derived threshold curve.

7.1 Variations in the density ratio curve fitting

There are two possible sources of systematic, or non-measurement, error in deriving the threshold friction speeds: the definition of threshold and the boundary layer profiles. In this section I explore these two parameters and how they would affect the density ratio curve.

7.1.1 Threshold definition

The threshold speed curve derived by Iversen et al. [1987] was constrained by data from four different sources, namely flume experiments [*Graff*, 1977], terrestrial wind tunnel experiments [*Greeley et al.,* 1976], MARWIT experiments [*Greeley et al.*, 1980], and VWT experiments [*Greeley et al.*, 1984]. I derived a new expression for this curve using data that I collected and data from Burr et al. [2015a]. There was not a unified

definition of threshold used in all of these experiments (see Appendix A2). The MARSWIT experiments defined threshold as "the speed at which the movement of particles [occurred] over the entire bed, rather than the movement of only a few individual particles" [*Greeley et al*., 1976]. The definition of threshold used in the VWT experiments is "the speed at which groups of grains began to saltate sporadically" [*Greeley et al*., 1984]. This thesis and Burr et al. [2015a] defined threshold in the TWT as the speed of at which ~50% of the bed is in motion, indicating that one-half of the grains have exceeded threshold and the other half have not. This definition is similar to that used in the MARSWIT experiments (Table A2 in the Appendix). However, the previous data most relevant to the shape of the intermediate density ratio curve are the VWT data. The TWT and VWT have same range in density ratios, yet different definitions of threshold are used for the experiments on the threshold curve.

To see if this difference in threshold definition significantly impacted the results of the threshold friction speed, I used data for a stage of motion that more closely corresponds to the definition of threshold used in the VWT work. Specifically, I considered the stage of 'patches', defined as sporadic or episodic grain motion, to be most comparable to the definition of threshold used in the VWT (Appendix A2). I analyzed results from selected experiments (performed in August 2016) for which stages of motion were recorded [cf. *Burr et al.,* 2015a, Extended Data, Table 3], D_p>200, and Re_{*t}>10. Data

from Burr et al. [2015a] were also examined but at the wind speed for 'patches', the data did not meet the Re_{*t}>10 criterion. In this reanalysis, all the experimental parameters remain constant, except that threshold corresponded to 'patches', a stage of lower activity and wind speed than ~50% of the bed in motion. An expression for *A* as a function of the density ratio is derived from the TWT thesis data using the patches threshold definition. The new best fit expression for *A* includes the constants γ =0.0041 and λ=0.87 Thus, for the 'patches' definition of threshold, Eq. 26 is

$$A = \frac{0.2}{\sqrt{1 + 2.3\left\{1 - e^{-0.0041\left(\rho_p/\rho - 1\right)^{0.87}}\right\}}}. \tag{38}$$

The data are plotted with the new curve for *A* in Figure 23. More of the patches data align within error of the old curve derived by Iversen et al. [1987] than the 50 % threshold data, suggesting that part of the mis-match found by Burr et al. 2015a was due to their different (higher) definition of threshold compared to that used in the VWT work. However, there is still an offset between the VWT and the TWT data.

Because of the continued separation of the VWT data and TWT data, even for threshold defined as patches, I again derive a curve for the TWT data alone (Fig. 21). The equation for that curve is

$$A = \frac{0.2}{\sqrt{\left(1 + 2.3\left\{1 - e^{\left[-0.0009\left(\rho_p/\rho - 1\right)^{0.97}\right]}\right\}\right)}}. \tag{39}$$

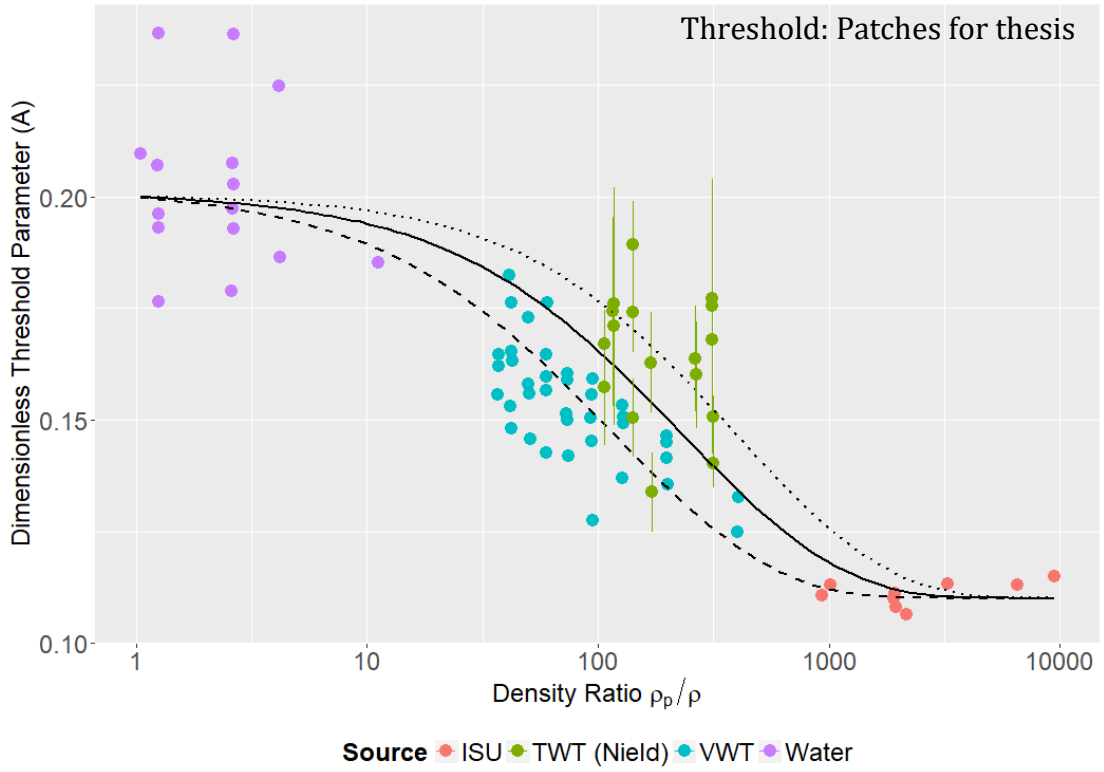


Figure 21: Threshold parameter *A*, for which the definition of threshold is 'patches', sporadic or episodic grain motion (Burr et al. 2015a), plotted as a function of the density ratio for various fluids for particles > 200 µm diameter and Re_{*t} >10 (solid line). Adapted from Iversen et al. [1987], with their density ratio curve (dashed line) overlaid on top of the VWT data, which did not include error bars. The density ratio curve derived using only TWT data is overlaid on the graph (dotted curve).

7.1.2 Boundary Layer Profiles

The boundary layer profiles, from which roughness heights are derived, are essential to convert freestream to friction speed using the Law of the Wall (Eq. 28). The BLPs were collected in the TWT prior to the experiments and using a fixed bed due to concern that saltating grains might clog the pitot tube. Boundary layer profiles collected from wind tunnel experiments with and without saltation are different, with higher friction wind speeds and lower roughness heights recorded in profiles with saltation (Figure 22) [*Bauer et al.*, 2004]. If the BLPs were recorded with saltation, then the threshold friction speeds could possibly be higher.

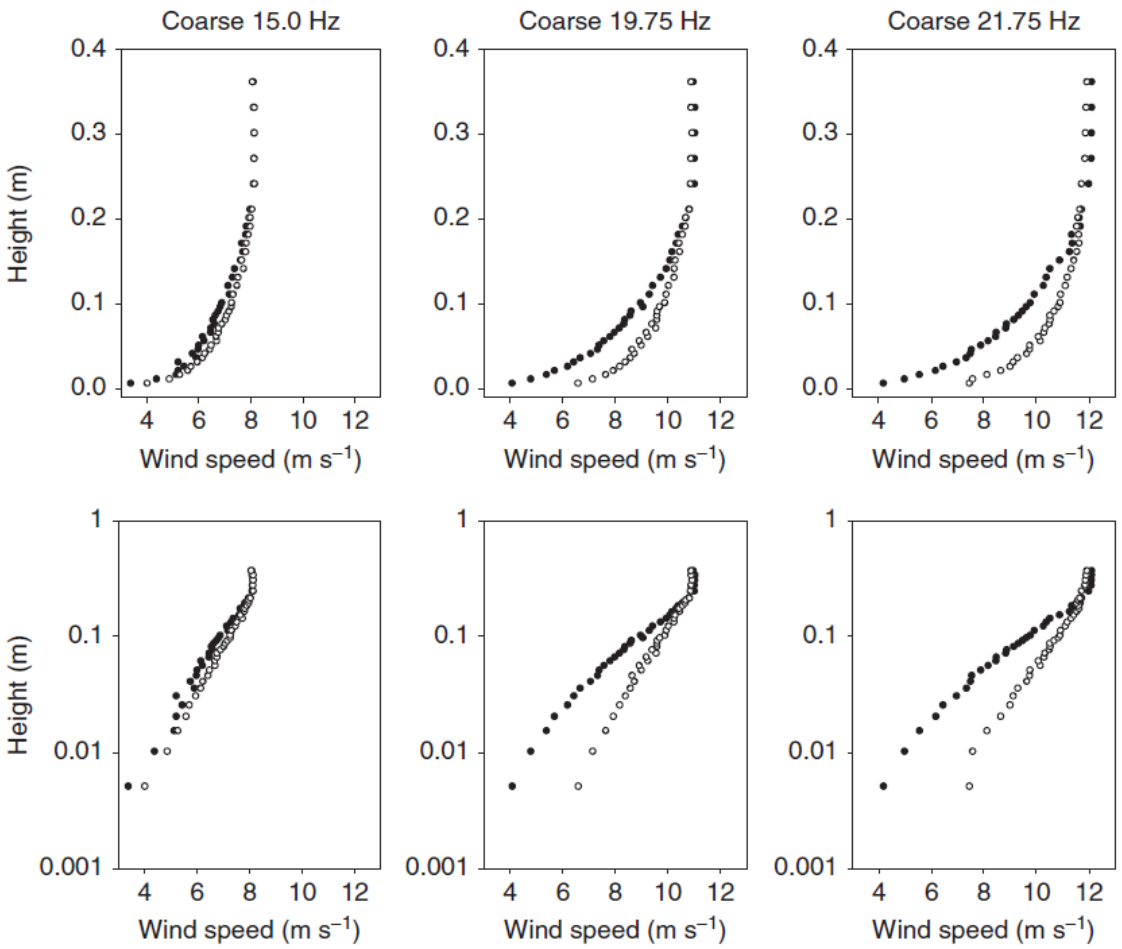


Figure 22: Boundary layer profiles taken with saltation (solid circles) and without saltation (open circles). These profiles show that the wind speed is consistently higher without the presence of saltation which produces a smaller roughness height. Reproduced from Bauer et al. [2013].

How the BLPs were reduced also affects the z_o value. In this work, the regression line is fit to the upper region of the BLP that corresponds to the area fit by the Law of the Wake instead of the lower region that corresponds to the area fit by the Law of the Wall (Eq. 28). If the lower region was fit, then the value of z_o is reduced by an order of magnitude. I performed a sensitivity analysis to see how u_{*t} would change if z_o is reduced by an order of magnitude. The initial values I used to calculate u_{*t} are u_∞ = 5 m/s, z =2 mm, u_* = 0.4 m/s, and z_o = 15 µm. I allowed z_o to vary from 0.1 to 30 µm. The percent change in u_* from the original value (0.4 m/s) is divided by the percent change in z_o from the initial value (15 µm) to calculate the sensitivity value (Figure 23). This sensitivity analysis shows that reducing the value of z_o by an order of magnitude significantly affects the value of threshold friction speed (Figure 24). For threshold defined as 50% bed motion, this reduction in u_{*t}, in turn, reduces Re_{*t} to be below 10 in all experiments except for six. Thus, only six data points fit the criterion from Iversen et al. (1987) of $Re_{*t} > 10$. Plotting these six data points on the density ratio curve (Figure 25) changes the original curve by Iversen et al. [1987] slightly. The expression for A using the lower region of the BLPs to derive threshold speeds at 50% bed motion is

$$A = \frac{0.2}{\sqrt{1 + 2.3\left\{1 - e^{-0.0072\left(\rho_p/\rho - 1\right)^{0.83}}\right\}}}. \tag{40}$$

As for previous plots, I've also derived density ratio curves using only the TWT data. That curve is shown on Fig. 25, and the expression is

$$A = \frac{0.2}{\sqrt{\left(1 + 2.3\left\{1 - e^{\left[-0.0012(\rho_p/\rho - 1)^{0.96}\right]}\right\}\right)}}. \tag{41}$$

There is no curve for when the TWT data is collected using the patches definition and fitted for the wall region because the Re_{*t} >10 criterion was not met for any of the experiments with these conditions.

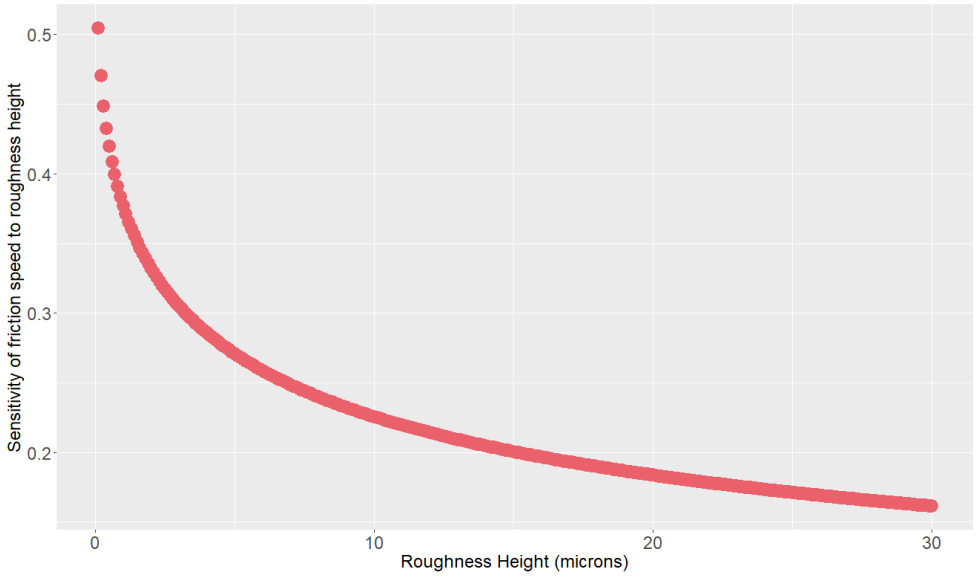


Figure 23: The sensitivity of the threshold friction speed to the roughness height. When the roughness height is lower than 10 µm, the threshold friction speed changes drastically.

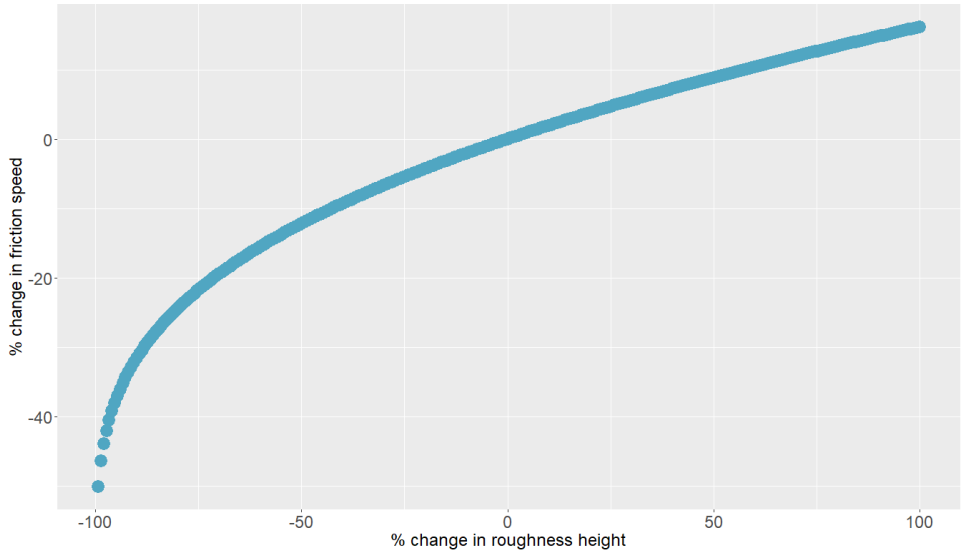


Figure 24: The change in wind speed for a change in roughness height, showing the sensitivity of the friction speed to roughness height. Reducing the value of z_o by an order of magnitude significantly affects the value of threshold friction speed.

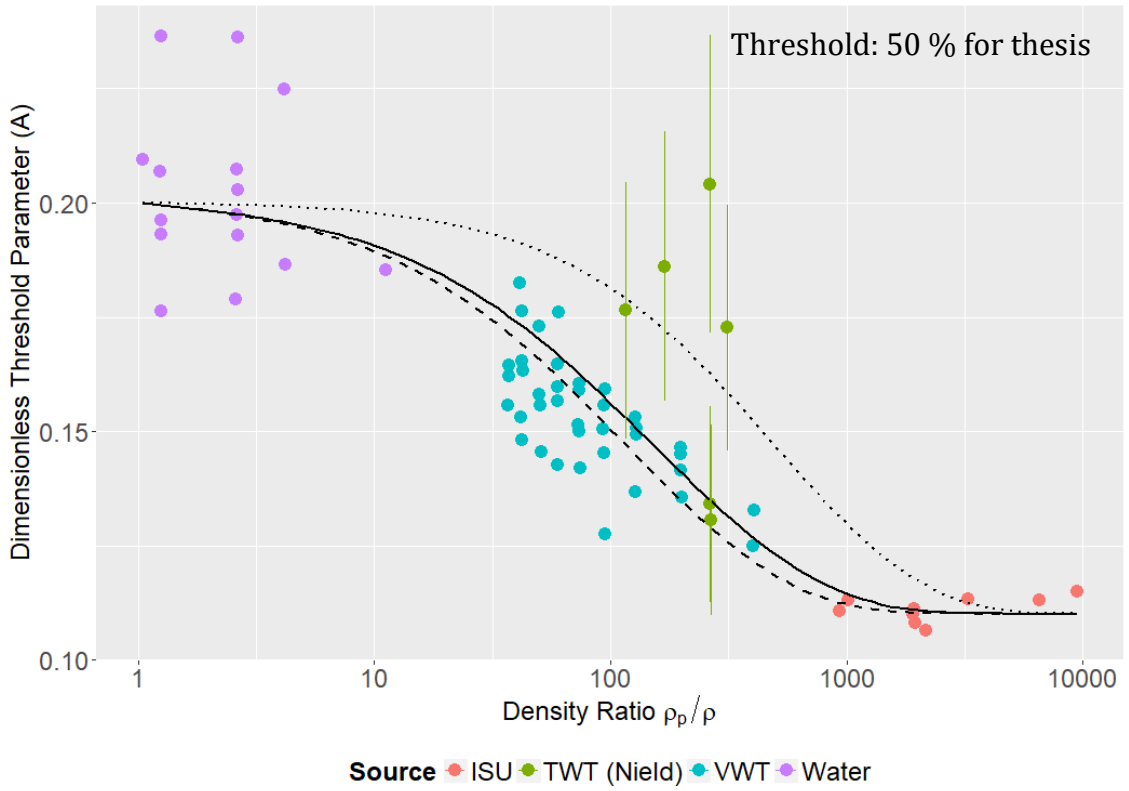


Figure 25: Threshold parameter *A* plotted as a function of the density ratio for various fluids for particles >200 µm diameter and Re_{*t} >10 (solid line). Adapted from Iversen et al. [1987], with their density ratio curve overlaid on top of the data (dashed line). The thesis data were derived using the z_o's calculated from the lower region of the boundary label profile. The definition of threshold for this plot is 50% bed motion. The density ratio curve derived using only TWT data is overlaid on the graph (dotted curve).

7.2 Possible explanation for the mismatch between the VWT and the TWT data

By considering the different sources of error (threshold definition and BLPs), I was able to derive three density ratio curves: 1) threshold defined as ~50% of the bed in motion and fitting the BLP to the wake region, 2) threshold defined as patches and fitting the BLP to the wake region, and 3) threshold defined as patches and fitting the BLP to the wall region. None of these derived curves align with the density ratio curve of Iversen et al. [1987]. Because the VWT and TWT datasets are visually distinct (Figs. 20, 21, and 25), I also derive, for each of these parameter combinations density, ratio curves for the TWT data alone. The parameters for each of these six curves are given below:

Table 5: Parameters from original work by Iversen et al. 1987 and derived in this thesis from fitting to the data for each of the boundary conditions as indicated. These data show the possible range of parameter values. I endorse the data in bold. Combinations with insufficient data are noted. *This value is corrected from the equation given in Iversen et al. 1987 (see Figure 7 above)

Threshold Definition	BLP fitting	Datasets	γ	λ
"The speed at which groups of grains began to saltate sporadically." [Greeley et al. 1984]	Not available	VWT only	0.0078*	0.86
New work in this thesis				
50%	Wake region	VWT +TWT	0.0032	0.89
50%	Wake region	TWT Only	0.0009	0.97
50%	Wall region	VWT +TWT	0.072	0.83
50%	Wall region	TWT Only	0.0012	0.96
Patches	**Wake region**	**VWT +TWT**	**0.0041**	**0.87**
Patches	Wake region	TWT Only	0.0019	0.92

From this work, I endorse the use the density ratio curve that uses the patches definition of threshold and reduces BLPs in the upper region as it most closely aligns with the threshold definition used in the VWT work. However, this new density ratio curve is not a close fit to the derived density ratio curve of Iversen et al. [1987]. If the data in the Iversen et al. curve had error bars, then their data might have aligned with this newly derived curve within error, removing the appearance of a mismatch. In the absence of error bars on the VWT data, I discuss possible explanations for the apparent mismatch. These explanations include: 1) grain size effects, 2) lack of sediment transport during BLP collection, 3) boundary layer depth in the small TWT test section, 4) different similitude parameters, 5) grain shape, and 6) grain sorting.

One possible explanation for the mismatch between the VWT and the TWT data is the smaller verses larger grain sizes, respectively. As shown in Figure 19, the experiments with larger grain sizes tended to plot further away from the curve. We do not know the grain size that corresponds with each VWT experiment but if we did, then we might see the same trend with smaller grains plotting closer to the density ratio curve. However, as noted above, a lack of grain size data for the VWT experiments precludes me from investigating this possibility in detail.

Another potential cause for the mismatch is lack of sediment transport during collection of the BLPs. Value for z_o derived from BLPs collected without sediment

transport are lower than those collected with transport (Figure 24; Bauer et al. 2013). Thus, the z_o values used in this work to convert the freestream wind speeds to friction wind speeds using the Law of the Wall (Eq. 28) are minima for the roughness heights during the experiments. These minimal roughness heights would result in maximal values for threshold friction wind speeds.

This increased value in *A* between the VWT and the TWT data could be a result of the effect of boundary layer depth on the fluctuation in wind speed [*Lu et al*., 2005]. That is, the smaller BL in the TWT would yield fewer fluctuations and so a higher relative threshold than for larger BLs. However, the VWT data, to which we're comparing most directly, were collected in the same tunnel, albeit at 30 bar. To compare the BLs would require the BL data from the VWT experiments, which are not available, as BLPs were not taking in the text section for that work (Greeley et al. 1984, Appendix II). Qualitatively, I consider that, because the TWT was refurbished from the VWT and the test section in these tunnels are identical with the same diameter and length [*Burr et al*., 2015b], any difference in boundary layer depth would be negligible.

Another reason for the mismatch could be the differences in the similitude parameters used to compare wind tunnel experiments on Earth to atmospheric conditions on Titan and Venus. For this work and previous TWT work, kinematic viscosity was used as the similitude parameter, in order to give the correct ratio of viscous forces

to density. In contrast, the VWT experiments used atmospheric density as the similitude parameter [*Greeley et al*., 1984]. To see if the different similitude parameters would affect the results, I calculate the atmospheric density similitude parameter in the TWT (Table 6). For kinematic viscosity to be the similitude parameter, the pressure in the wind tunnel is set to 12.5 bars. For atmospheric density to be the similitude parameter, then the air pressure in the tunnel would be set to 4.4 bars. Lowering the atmospheric pressure, would lower the atmospheric density from 14.9 kg/m^3 to 5.2 kg/m^3. By having a lower atmospheric density, the density ratio would increase. This increase in density ratio would further increase the mismatch between the TWT and the VWT results. Thus, it does not explain the current mismatch.

Table 6: A comparison of similitude parameters in the Titan Wind Tunnel and Titan. Red is when the atmospheric density is the similitude parameter and blue represents when the similitude parameter is kinematic viscosity.

Parameter	Titan	TWT (kinematic viscosity)	TWT (atmospheric density)
Gas Composition	~95% N2, ~5% CH4	~79% N2, ~20% O2	~79% N2, ~20% O2
Pressure (Pa)	144000	1250000	435000
Temperature (K)	94	293	293
Dyn. Viscosity (Pa s)	6.25E-06	1.85E-05	1.83E-05
Atm. Density (kg/m^3)	5.3	14.9	5.3
Kin. Viscosity (m^2/s)	1.2E-06	1.2E-06	3.5E-06

The shape of the grains could account for the mismatch between the two tunnels. The VWT only used quartz in their test section while we used a wide variety of materials in the TWT. The different experimental sediments have qualitatively different angularities. Walnut shells and plastic chips are visibly more angular than materials like QF sand (Figure 26) or glass spheres. The shape may have an effect on interparticle force, e.g., by increasing the surface area to weight ratio and by promoting interlocking (*McKenna-Neuman & Sanderson*, 2008). However, because I chose grains that are greater than 200 microns to make the interparticle force negligible, I do not expect the shape of the grain to significantly impact the results. To explore the possible effects of angularity, I plotted the data as a function of material type (Figure 27). The results show that QF sand, walnut shells, and plastic chips are equally distributed along the density ratio spectrum, and that data points from glass spheres, walnut shell, and basalt lie equally close to the curve. Thus, in these data, there is no discernable correlation between grain and position on the density ratio curve.



Figure 26 : Photographs of materials used in the Titan Wind Tunnel showing how the QF material is more rounded than the Walnut Shells and Plastic Chips.

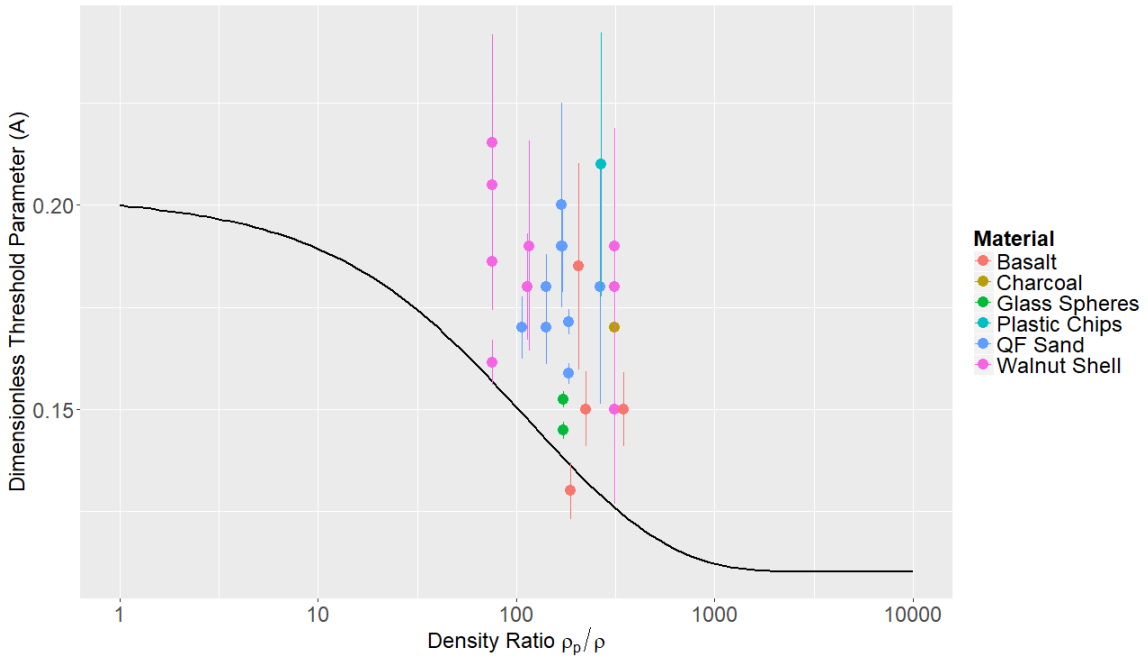


Figure 27: Values of the threshold parameter *A*, derived from TWT experiments, plotted as a function of the density ratio for various fluids for particles >200 µm diameter and Re_{*t} >10 sorted by grain material. Adapted from Iversen et al. [1987], with their density ratio curve overlaid on top of the data. Data collected previously from the Titan Wind Tunnel [*Burr et al*., 2015a] are included. This plot shows no discernable correlation between grain shape and position on the density ratio curve.

Another parameter that could affect the *A* parameter is the effect of grain sorting. The value of *A* is often larger for mixed particle sizes than uniforms one [*Lu et al*., 2005]. In this thesis, the grains were sieved to have uniform sizes. The sieve ranges follow the phi (φ) scale, so that there is a larger range in grain sizes for sieves with a lower φ value, e.g. 833-1000 µm (0 to 1 φ) has a range of 167 µm while 175-250 µm (2-3 φ) has a smaller range of 75 µm. As shown in Figure 19, this small variation in grain range does not appear to impact the results, as there is no apparent correlation between grain size and *A*. Thus, I conclude that grain sorting did not account for the mismatch in the results between the VWT and TWT data.

This new density ratio curve results in higher values for *A*. This result suggests that the threshold windspeeds to move the sand in the vast tropical dune fields on Titan are higher than we previously thought. More generally, this result suggests that – for any given wind speed – it is more difficult to move sand on planetary bodies with thick atmospheres. However, the possible effects of lower roughness heights during BLP collection than during experimental runs would mitigate and possible erase this difference.

The results of this work illustrate the importance of including the density ratio term when calculating threshold speeds on planetary bodies with thick atmospheres, like

Venus, Titan, and extrasolar planets with thick atmospheres (high density ratio conditions) [e.g., *Bean et al*., 2010; *Quintana et al*., 2014].

7.3 Future work

The most important factor for further exploration in future work would be to understand the shape of the boundary layer profiles. This shape affects the derivation of z_o, as described above, and thus of the derived values of u^*_t. The cause for the two-part boundary layer –with a lower region obeying the Law of the Wall and an upper region obeying the Law of the Wake – is not clear.

To increase the accuracy of the BLPs, the BLPs should be collected while saltation is present in the tunnel. This collection could be done in the future with larger grain sizes as smaller grain sizes clog up the pitot tube when saltating in the tunnel. These new BLPs would make the roughness heights more accurate and would perhaps eliminate the duality in regression lines that are currently present.

In future work, it would also be useful to fill in the missing sections of the density ratio curve in order to fit the density ratio curve more precisely and produce a more accurate expression. To fill in the region between 10 and 50 ρ_p/ρ, one could use a flume with high density material, ex. lead (11.34 g/cm^3). An alternate option is to run the TWT at pressures above 20 bar, although this option would require refurbishment of the TWT so that it could be recertified to up to 30 bar. To fill in the region between 500 and 1500

ρ_p/ρ, one could use a terrestrial wind tunnel with low density material, ex. walnut shells (1.1 g/cm^3). By filling out these regions on the density ratio curve, a more accurate expression can be derived to fit the curve. With these higher density ratios, I would obtain higher values for Re_{*t} so that I could still meet criterion and fit to density ratio curve.

To anchor the high-density ratio end of the plot, the MARSWIT data collected by Greeley et al. [1980] could be reexamined. As stated in Section 2.6, the derivation of the density ratio term excludes all data from MARSWIT due to the criterion that all the data used to derive the curve must have a Re_{*t} >10. As shown in Figure 3, the data scatter in A reduces significantly when Re_{*t}>10 and begins to approach an asymptote where Re_{*t} is independent of A. This universal asymptote encompasses all data from each wind tunnel. At the same time, however, each dataset exhibits its own unique asymptote. Selecting an asymptote for each dataset (e.g. MARSWIT, VWT, ISU) would allow more data (i.e., from the MARSWIT) to be used to derive the asymptote for high density ratio conditions, thereby potentially changing the curve derived by Iversen et al. [1987].

8. Summary

A general expression for aeolian saltation threshold, which takes the density ratio effect into account, is needed for the prediction of particle saltation threshold speeds on Earth as well as on other planetary bodies where aeolian activity is present. Iversen et al. [1987] derived a term for the density ratio in their threshold model. Their density ratio term was wrapped into the expression for the dimensionless threshold parameter, *A*. *A* is dependent on the Reynolds number, the interparticle force, and the density ratio term. To derive an expression for the density ratio, Iversen *et al.* only used experiments where D_p> 200 µm and Re_{*t}>10 to eliminate the dependency on the Reynold's number and the interparticle force. My goal in this work was to test the validity of the density ratio expression from Iversen et al. To achieve this goal, I ran a total of 67 threshold experiments at the Titan Wind Tunnel under a range of density ratios conditions. These experiments all had grain sizes larger than 200 µm, but only 19 of them had a Re_{*t}>10. I compared these new data, along with the threshold data from Burr et al. [2015a], to the density ratio curve of Iversen et al. [1987] and found it not to fit the TWT data. The null hypothesis of this work, that the density ratio expression derived by Iversen et al. [1987] was correct, is rejected and the alternate hypothesis that the density ratio expression is incorrect was accepted. The work revealed two main sources of uncertainty in the data collection and analysis – specifically, the definition of threshold and deriving z_o from the

BLPs. For each of these data collection and analysis permutations I provide new curves for the density ratio expression, using the data collected for this thesis and data published Burr et al. [2015a] and Iversen et al. [1987]. All the derived curves increase the value of *A*, increasing the threshold friction wind speeds. This increase makes it more difficult for sand to be entrained on Titan as the winds need to blow faster for sand to be entrained.

This work has revealed the intricacies and issues in deriving expressions for saltation threshold under planetary conditions. The results published here provide a robust range of parameter values, along with known uncertainty estimates, for the threshold expression under high-atmospheric density conditions. Thus, they will contribute to increasing our ability to correctly estimate threshold friction speeds on planetary bodies. As a result, they will improve all aspects of aeolian science that depend on threshold values, including estimates of sediment transport, mass flux, and minimum aeolian erosion potential and effectiveness.

List of References

Bagnold, R. A., 1941, The Physics of Blown Sand and Desert Dunes, London, Dover.

Bauer, B. O., Houser, C. A., and Nickling, W. G., 2004, Analysis of velocity profile measurements from wind-tunnel experiments with saltation: Geomorphology, v. 59, no. 1, p. 81-98.

Bean, J. L., Kempton, E. M.-R., and Homeier, D., 2010, A ground-based transmission spectrum of the super-Earth exoplanet GJ 1214b: Nature, v. 468, no. 7324, p. 669-672.

Bennett, S.J., P. Ashmore, and C. McKenna Neuman, 2015, Transformative geomorphic research using laboratory experimentation, Geomorphology, v. 244, p. 1-8.

Bridge, J. S., and Bennett, S. J., 1992, A model for entrainment and transport of sediment grains of mixed sizes, shapes, and densities: Water Resources Research, v. 28, no. 2, p. 337-363.

Bridges, N. T., Ayoub, F., Avouac, J. P., Leprince, S., Lucas, A., and Mattson, S., 2012, Earth-like sand fluxes on Mars: Nature, v. 485, no. 7398, p. 339-342.

Bridges, N. T., Greeley, R., Haldemann, A. F. C., Herkenhoff, K. E., Kraft, M., Parker, T. J., and Ward, A. W., 1999, Ventifacts at the Pathfinder landing site: Journal of Geophysical Research E: Planets, v. 104, no. E4, p. 8595-8615.

Bridges, N. T., Phoreman, J., White, B. R., Greeley, R., Eddlemon, E. E., Wilson, G. R., and Meyer, C. J., 2005, Trajectories and energy transfer of saltating particles onto rock surfaces: Application to abrasion and ventifact formation on Earth and Mars: Journal of Geophysical Research: Planets, v. 110, no. E12.

Burr, D. M., Bridges, N. T., Marshall, J. R., Smith, J. K., White, B. R., and Emery, J. P., 2015a, Higher-than-predicted saltation threshold wind speeds on Titan: Nature, v. 517, no. 7532, p. 60-U137.

Burr, D. M., Bridges, N. T., Smith, J. K., Marshall, J., White, B., and Williams, D. A., 2015b, The Titan Wind Tunnel: A new tool for investigating extraterrestrial aeolian environments: Aeolian Research, v. 18, p. 10.

Cheng, A. F., Lisse, C. M., and A'Hearn, M., 2013, Surface geomorphology of Jupiter Family Comets: A geologic process perspective: Icarus, v. 222, no. 2, p. 808-817.

Chepil, W. S., 1958, The use of evenly spaced hemispheres to evaluate aerodynamic forces on a soil surface: Eos, Transactions American Geophysical Union, v. 39, no. 3, p. 397-404.

Chepil, W. S., and Milne, R. A., 1941, Wind erosion of soil in relation to roughness of surface: Soil Science, v. 52, no. 1, p. 417-433.

Cohen-Zada, A. L., Blumberg, D. G., and Maman, S., 2016, Earth and planetary aeolian streaks: A review: Aeolian Research, v. 20, p. 108-125.

Elhakeem, M., and Imran, J., 2012, Density Functions for Entrainment and Deposition Rates of Nonuniform Sediment: Journal of Hydraulic Engineering-Asce, v. 138, no. 7, p. 591-609.

Ewing, R. C., Hayes, A. G., and Lucas, A., 2013, Reorientation Time-Scales of Titan's Equatorial Dunes, 44th Lunar and Planetary Science Conference: Houston, Lunar and Planetary Institute, p. Abstract #1187.

Coleman, N. L., 1967, A theoretical and experimental study of drag and lift forces acting on a sphere resting on a hypothetical stream bed: Proc. 12th Congr. IAHR, v. 3, p. 185-192.

Garvin, J. B., Mouginismark, P. J., and Head, J. W., 1981, Characterization of rock populations on planetary surfaces- techniques and a preliminary analysis of Mars and Venus: Moon and the Planets, v. 24, no. 3, p. 355-387.

Golombek, M. P., Grant, J. A., Crumpler, L. S., Greeley, R., Arvidson, R. E., Bell Iii, J. F., Weitz, C. M., Sullivan, R. J., Christensen, P. R., Soderblom, L. A., and Squyres, S. W., 2006, Erosion rates at the Mars Exploration Rover landing sites and long-term climate change on Mars: Journal of Geophysical Research E: Planets, v. 111, no. 12.

Graf, W. H., 1971, Hydraulics of Sediment Transport, Highlands Ranch, CO, Water Resources Publications.

Greeley, R., Arvidson, R. E., Elachi, C., Geringer, M. A., Plaut, J. J., Saunders, R. S., Schubert, G., Stofan, E. R., Thouvenot, E. J. P., Wall, S. D., and Weitz, C. M., 1992, Aeolian features on Venus - Preliminary Magellan results: Journal of Geophysical Research-Planets, v. 97, no. E8, p. 13319-13345.

Greeley, R., Iversen, J., Leach, R., Marshall, J., White, B., and Williams, S., 1984, Winblown sand on Venus: Preliminary Results of Laboratory Simulations: Icarus, v. 57, no. 1, p. 112-124.

Greeley, R., Kraft, M. D., Kuzmin, R. O., and Bridges, N. T., 2000, Mars Pathfinder landing site: Evidence for a change in wind regime from lander and orbiter data: Journal of Geophysical Research: Planets, v. 105, no. E1, p. 1829-1840.

Greeley, R., Leach, R., White, B., Iversen, J., and Pollack, J., 1980, Threshold windspeeds for sand on Mars: Wind tunnel simulations: Geophysical Research Letters, v. 7, no. 2, p. 121-124.

Greeley, R., White, B., Leach, R., Iversen, J., and Pollack, J., 1976, Mars: Wind friction speeds for particle movement: Geophysical Research Letters, v. 3, no. 8, p. 417-420.

Hayward, R. K., Fenton, L. K., and Titus, T. N., 2014, Mars Global Digital Dune Database (MGD(3)): Global dune distribution and wind pattern observations: Icarus, v. 230, p. 38-46.

Hayward, R. K., Mullins, K. F., Fenton, L. K., Hare, T. M., Titus, T. N., Bourke, M. C., Colaprete, A., and Christensen, P. R., 2007, Mars global digital dune database and initial science results: Journal of Geophysical Research-Planets, v. 112, no. E11.

Iversen, J. D., Greeley, R., Marshall, J. R., and Pollack, J. B., 1987, Aeolian saltation threshold: the effect of density ratio: Sedimentology, v. 34, no. 4, p. 699-706.

Iversen, J. D., Greeley, R., and Pollack, J. B., 1976a, Windblown dust on Earth, Mars, and Venus: Journal of the Atmospheric Sciences, v. 33, no. 12, p. 2425-2429.

Iversen, J. D., Pollack, J. B., Greeley, R., and White, B. R., 1976b, Saltation threshold on Mars - The effect of interparticle force, surface roughness, and low atmospheric denisty: Icarus, v. 29, no. 3, p. 381-393.

Iversen, J. D., and White, B. R., 1982, Saltation threshold on Earth, Mars, and Venus: Sedimentology, v. 29, no. 1, p. 111-119.

Knight, J., 2008, The environmental significance of ventifacts: A critical review: Earth-Science Reviews, v. 86, no. 1, p. 89-105.

Kok, J. F., and Renno, N. O., 2009, A comprehensive numerical model of steady state saltation (COMSALT): Journal of Geophysical Research-Atmospheres, v. 114, p. 20.

Kok, J. F., 2010, An improved parameterization of wind-blown sand flux on Mars that includes the effect of hysteresis: Geophysical Research Letters, v. 37, p. 6.

Kok, J. F., Parteli, E. J. R., Michaels, T. I., and Karam, D. B., 2012, The physics of wind-blown sand and dust: Reports on Progress in Physics, v. 75, no. 10, p. 72.

Laity, J. E., and Bridges, N. T., 2009, Ventifacts on Earth and Mars: Analytical, field, and laboratory studies supporting sand abrasion and windward feature development: Geomorphology, v. 105, no. 3-4, p. 202-217.

Lorenz, R. D., Wall, S., Radebaugh, J., Boubin, G., Reffet, E., Janssen, M., Stofan, E., Lopes, R., Kirk, R., Elachi, C., Lunine, J., Mitchell, K., Paganelli, F., Soderblom, L., Wood, C., Wye, L., Zebker, H., Anderson, Y., Ostro, S., Allison, M., Boehmer, R., Callahan, P., Encrenaz, P., Ori, G. G., Francescetti, G., Gim, Y., Hamilton, G., Hensley, S., Johnson, W., Kelleher, K., Muhleman, D., Picardi, G., Posa, F., Roth, L., Seu, R., Shaffer, S., Stiles, B., Vetrella, S., Flamini, E., and West, R., 2006, The sand seas of Titan: Cassini RADAR observations of longitudinal dunes: Science, v. 312, no. 5774, p. 724-727.

Lorenz, R. D., and Zimbelman, J. R., 2014, Dune Worlds: How windblown sand shapes planetary landscapes, New York, Springer, p. 290

Lu, H., Raupach, M., and Richards, K., 2005, Modeling entrainment of sedimentary particles by wind and water: A generalized approach: Journal of Geophysical Research: Biogeosciences (JGR), v. 110, no. D24.

McComas, D. J., Elliott, H. A., Weidner, S., Valek, P., Zirnstein, E. J., Bagenal, F., Delamere, P. A., Ebert, R. W., Funsten, H. O., Horanyi, M., McNutt, R. L., Moser, C., Schwadron, N. A., Strobel, D. F., Young, L. A., Ennico, K., Olkin, C. B., Stern, S. A., and Weaver, H. A., 2016, Pluto's interaction with the solar wind: Journal of Geophysical Research: Space Physics, v. 121, no. 5, p. 4232-4246.

McKenna-Neuman, C., 2003, Effects of temperature and humidity upon the entrainment of sedimentary particles by wind: Boundary-Layer Meteorology, v. 108, no. 1, p. 61-89.

McKenna Neuman C. and Sanderson S., 2008, Humidity control of particle emissions in aeolian systems: Journal of Geophysical Research, v. 113, F02S14.

Quintana, E. V., Barclay, T., Raymond, S. N., Rowe, J. F., Bolmont, E., Caldwell, D. A., Howell, S. B., Kane, S. R., Huber, D., Crepp, J. R., Lissauer, J. J., Ciardi, D. R., Coughlin, J. L., Everett, M. E., Henze, C. E., Horch, E., Isaacson, H., Ford, E. B., Adams, F. C., Still, M., Hunter, R. C., Quarles, B., and Selsis, F., 2014, An Earth-Sized Planet in the Habitable Zone of a Cool Star: Science, v. 344, no. 6181, p. 277-280.

Reiss, D., Fenton, L., Neakrase, L., Zimmerman, M., Statella, T., Whelley, P., Rossi, A. P., and Balme, M., 2016, Dust Devil Tracks: Space Science Reviews, v. 203, no. 1-4, p. 143-181.

Rubin, D. M., and Hunter, R. E., 1987, Bedform Alignment in Directionally Varying Flows: Science, v. 237, no. 4812, p. 276-278.

Sagan, C., and Chyba, C., 1990, Triton's streaks as windblown dust: Nature, v. 346, no. 6284, p. 546-548.

Sagan, C., Pieri, D., Fox, P., Arvidson, R. E., and Guinness, E. A., 1977, Particle motion on Mars inferred from the Viking Lander cameras: Journal of Geophysical Research, v. 82, no. 28, p. 4430-4438.

Schlichting, H., 1968. Boundary-Layer Theory, 6th ed. McGraw-Hill, New York.

Shao, Y., 2008. Physics and modelling of wind erosion, 2nd ed. Springer, Cologne, Germany.

Shao, Y. P., and Lu, H., 2000, A simple expression for wind erosion threshold friction velocity: Journal of Geophysical Research-Atmospheres, v. 105, no. D17, p. 22437-22443.

Tregnaghi, M., Bottacin-Busolin, A., Marion, A., and Tait, S., 2012, Stochastic determination of entrainment risk in uniformly sized sediment beds at low

transport stages: 1. Theory: Journal of Geophysical Research-Earth Surface, v. 117, p. 15.

Weitz, C. M., Plaut, J. J., Greeley, R., and Saunders, R. S., 1994, Dunes and microdunes on Venus: Why were so few found in the Magellan data: Icarus, v. 112, no. 1, p. 282-295.

White, B. R., 1979, soil transport by winds on Mars: Journal of Geophysical Research: Solid Earth, v. 84, no. B9, p. 4643-4651.

White, B. R., 1981, Venusian saltation: Icarus, v. 46, no. 2, p. 226-232.

Appendix

A1: Experimental set up for previous threshold studies

Table A1: A summary table of the experimental parameters used in previous threshold experiments. All experiments were conducted by placing material into the wind tunnel and incrementally increasing the wind speed in the tunnel until threshold, as defined

Reference	Wind Tunnel	Bed Materials	Particle Density Range (g/cm^3)	Median Particle Diameter Range (microns)	Fluid Composition	Fluid Pressure	Experimental Set Up
Bagnold [1941]	Imperial College Wind Tunnel	sand	not stated	180-300	air	1 bar	Placed the bed of sand, 1.5 cm thick, evenly across the wind tunnel floor and threshold was visually observed by eye.
Greeley et al. [1974]	Iowa State University	sand, glass beads, clover seed, sugar, salt, copper-oxide, bronze, copper, lead	1.3-11.35	8-1290	air	1 bar	Placed the bed material on the surface of the boundary layer and visually determined threshold 5 m downwind from the test section entrance.
Greeley et al. [1976a]	Martian Surface Wind Tunnel	walnut shell, calcium carbonate, glass microspheres, talc	1.1-3	5-700	air	5.3 mb	Placed "a patch of grains" in the tunnel test section and threshold was observed with an optical system.
Greeley *et al.* [1980]	Martian Surface Wind Tunnel	walnut shell	1.1	23-800	95% CO_2 and 5% air	4-80 mb	Placed a 2.5 m long bed of material was placed in the wind tunnel and threshold was observed using an electrostatic detector and high resolution television system.
Greeley et al. [1984]	Venus Wind Tunnel	quartz sand	2.65	30-650	air	30 bar	Placed a full bed in the wind tunnel and visually observed it with a television system that provided eightfold magnification of the field of view.
Burr et al. [2015a]	Titan Wind Tunnel	walnut shell, gas chromatograph packing material, glass spheres, silica sand, basaltic sand	1.1-3	81-917	air	12.5 bar	Placed a 1 cm thick bed of material in the tunnel and visually observed the bed with the human eye.

A2: Definitions of experimental threshold

A fundamental question in threshold experiments is: How is the condition of incipient motion identified? In general, the sediment bed is observed to determine when, under conditions of slowly increasing the speed of the flow, the sediment begins to move. But this method has flaws. Even in weak flows, a particularly strong turbulent eddy could occur and bed material can move as a result. This difficulty in observing threshold has led many researchers to adopt different definitions as summarized in Table A2. Any technology used in making the observations is indicated in Table A1.

Table A2: Definitions of threshold movement used in previous wind tunnel studies

Reference	Wind tunnel	Threshold Definition
Bagnold [1941]	Imperial College Wind Tunnel	The point when "the grains could be seen to have gathered sufficient speed to start bouncing off the ground."
Greeley et al. [1974]	Iowa State University	No definition provided
Greeley et al. [1976]	Martian Surface Wind Tunnel	The speed at which “the movement of particles [occurred] over the entire bed, rather than the movement of only a few individual particles.”
Greeley et al. [1980]	Martian Surface Wind Tunnel	The speed at which "grains of a given size are set into motion over an entire bed."
Greeley et al. [1984]	Venus Wind Tunnel	“The speed at which groups of grains began to saltate sporadically.”
Burr et al. [2015]	Titan Wind Tunnel	The speed of at which “50% of the bed [is] in motion, indicating that one-half of the grains have exceeded threshold and the other half have not.”

A3: Experimental matrix

Table A3: Experimental matrix used for threshold experiments conducted in the Titan Wind Tunnel. The number after the 'T-' refers to the year the data were collected.

Material and Size Range	Density, ρ_p (kg/m^3)	Experiment Number	Desired Pressure (bar)	Atmospheric Denisty, ρ (kg/m^3)	Kinematic Viscosity, ν (m^2/s)	Density Ratio (ρ_p/ρ)
Walnut Shells 833-1000 µm	1100	T-16-1298	3	3.53	5.20E-06	311.85
		T-16-1297	8	9.46	1.95E-06	116.33
		T-16-1296	12.5	14.78	1.25E-06	74.44
		T-16-1295	15	17.68	1.05E-06	62.23
		T-16-1294	20	23.50	7.93E-07	46.81
Walnut Shells 833-1000 µm	1100	T-17-1501	3	3.51	5.23E-06	313.69
		T-17-1500	8	9.64	1.91E-06	114.07
		T-17-1499	12.5	14.94	1.24E-06	73.61
		T-17-1498	15	17.66	1.05E-06	62.30
Walnut Shells 707-833 µm	1100	T-17-1514	3	3.51	5.22E-06	313.09
		T-17-1513	8	9.48	1.95E-06	116.09
		T-17-1512	12.5	14.75	1.26E-06	74.59
		T-17-1511	15	17.57	1.06E-06	62.62
Walnut Shells 500-600 µm	1100	T-17-1497	3	3.61	5.09E-06	305.08
		T-17-1496	8	9.54	1.93E-06	115.29
		T-17-1495	12.5	14.85	1.25E-06	74.10
		T-17-1494	15	17.62	1.05E-06	62.43
Walnut Shells 175-250 µm	1100	T-17-1503	12.5	14.94	1.24E-06	73.60
		T-17-1502	15	17.55	1.06E-06	62.68
Quartzo-feldspathic Sand 833-1000 µm	2500	T-16-1328	8	9.43	1.95E-06	265.01
		T-16-1327	12.5	14.72	1.26E-06	169.78
		T-16-1326	15	17.63	1.05E-06	141.81
		T-16-1325	20	23.40	7.97E-07	106.83
Quartzo-feldspathic Sand 833-1000 µm	2500	T-17-1485	12.5	14.97	1.24E-06	167.06
		T-17-1516	12.5	14.83	1.25E-06	168.60
		T-17-1515	15	17.71	1.05E-06	141.19
Quartzo-feldspathic Sand 707-833 µm	2500	T-17-1520	8	9.50	1.94E-06	263.19
		T-17-1519	12.5	14.80	1.25E-06	168.96
		T-17-1518	15	17.64	1.05E-06	141.73
Quartzo-feldspathic Sand 600-707 µm	2500	T-17-1523	8	9.49	1.94E-06	263.32
		T-17-1522	12.5	14.78	1.25E-06	169.18
		T-17-1521	15	17.64	1.05E-06	141.74
Quartzo-feldspathic Sand 500-600 µm	2500	T-17-1531	8	9.46	1.95E-06	264.15
		T-17-1530	12.5	14.76	1.25E-06	169.36
		T-17-1529	15	17.62	1.05E-06	141.86

Table A3 Continued

Material and Size Range	Density, ρ_p (kg/m^3)	Experiment Number	Desired Pressure (bar)	Atmospheric Denisty, ρ (kg/m^3)	Kinematic Viscosity, ν (m^2/s)	Density Ratio (ρ_p/ρ)
Basalt 707-1000 µm	3300	T-17-1535	8	9.47	1.95E-06	348.63
		T-17-1534	12.5	14.75	1.26E-06	223.71
		T-17-1533	15	17.59	1.05E-06	187.58
Basalt 500-707 µm	3300	T-17-1538	8	9.57	1.93E-06	344.82
		T-17-1537	12.5	14.78	1.25E-06	223.25
		T-17-1536	15	17.62	1.05E-06	187.24
Basalt 500-707 µm	3000	T-16-1345	8	9.44	1.95E-06	317.75
		T-16-1344	12.5	14.70	1.26E-06	204.04
Charcoal 250-300 µm	400	T-16-1356	1	1.27	1.43E-05	314.66
		T-16-1355	3	3.54	5.19E-06	113.07
		T-16-1354	8	9.44	1.95E-06	42.36
		T-16-1353	12.5	14.73	1.26E-06	27.16
		T-16-1352	15	17.64	1.05E-06	22.67
		T-16-1351	20	23.37	7.98E-07	17.12
Charcoal 425-500 µm	400	T-16-1374	1	1.27	1.44E-05	315.52
		T-16-1373	3	3.56	5.15E-06	112.21
		T-16-1372	8	18.80	9.81E-07	21.28
		T-16-1371	12.5	14.86	1.25E-06	26.92
		T-16-1370	15	17.76	1.04E-06	22.52
		T-16-1369	20	23.54	7.92E-07	17.00
Charcoal 600-707 µm	400	T-16-1392	1	1.27	1.43E-05	314.12
		T-16-1391	3	3.57	5.14E-06	112.13
		T-16-1390	8	9.53	1.93E-06	41.97
		T-16-1389	12.5	14.83	1.25E-06	26.98
		T-16-1388	15	17.74	1.05E-06	22.55
		T-16-1387	20	23.22	8.03E-07	17.22
Glass Beads 300-600 µm	2500	T-17-1527	8	9.47	1.95E-06	263.93
		T-17-1526	12.5	14.77	1.25E-06	169.30
		T-17-1525	15	17.63	1.05E-06	141.84
Plastic Chips (LPDE) 606-833 µm	940	T-17-1543	3	3.51	5.23E-06	268.02
		T-17-1542	8	9.48	1.95E-06	99.17
		T-17-1541	12.5	14.75	1.26E-06	63.74
		T-17-1540	15	17.59	1.05E-06	53.45

A4: R Code to reduce boundary layer profiles to find z and z_o

Source of Data

Data from the Titan Wind Tunnel are collected in CSV format with two columns for transducer voltages and a column for the time the data was collected. The voltages are recorded every tenth of a second.

User Inputs

The program asks the user to manually enter the following information into the console:

- Name of the CSV file that contains the voltages and times recorded by Tavis 1 and 2.
- The height interval to perform the linear regression for both the freestream height (z) and the roughness height (z_o)

Program Outputs

- The freestream height (z)
- Roughness height (z_o) for both Tavis 1 and Tavis 2 and the fractional uncertainty
- Summary of all the inputs that the user types into the console

Step 1: Input and filter the data

The raw data reports the voltages recorded along each position that the pitot tube transverses. The program eliminates the voltages that were recorded while the pitot tube was traversing between positions.

```
#Read in the CSV file
CSV<-read.csv(skip=7,"103% fan.csv", col.names=c("Sample","Position","Tavis1","Tavis2",
"Druck", "Events","Events1"))

#Filter the data by keeping only positions that we want, define the positions
target <- c(22,21529, 43141, 64739, 86422, 107938, 129537, 151653, 173246, 194730,
216214, 237691, 259235, 296930, 334612, 372354, 410308, 448130, 485469, 539075, 592787,
646415, 700812, 769993, 839476, 1603259)

CSV_filtered<-CSV%>%
  filter(Position %in% target)%>%
  select(-Events, -Events1)
```

Step 2: Average the data

The program averages the data for each position.

```
CSV_filtered<-CSV_filtered%>%
  group_by(Position) %>%
  summarize(T1 = mean(Tavis1, na.rm = TRUE),
            T2 = mean(Tavis2, na.rm = TRUE),
            Druck = mean(Druck, na.rm = TRUE))
```

Step 3: Add in height data

The program adds in a new column with the heights (in cm) that the pitot tube collected data at.

```
#Create a column of the heights
Height<-c(0, 0.0991, 0.1981, 0.2972, 0.3962, 0.4953, 0.5944, 0.6934, 0.7925, 0.8915,
0.9906, 1.0897, 1.1887, 1.3868, 1.585, 1.7831, 1.9812, 2.1793, 2.3774, 2.6772, 2.9769,
3.2766, 3.5763, 3.9751, 4.3739, 4.7727)

#Add the height column to filtered dataframe
CSV_filtered<-cbind(CSV_filtered, "Height" = Height)
```

Step 4: Calculate the atmospheric density

The air density (ρ) inside the tunnel is calculated using the following equation:

$$\rho = \frac{P}{RT}$$

where *P* is the absolute pressure in Pa, *T* is the temperature in K, and *R* is the dry air constant (*R*=287.04 Kg K). The gauge pressure shows the pressure inside the tunnel and is given in psig, which is converted to absolute pressure. The gauge pressure is recorded as a voltage in the "Druck" column of the data. The program finds the average value in the Druck column and multiplys it by 60 to get the gauge pressure in psig.

```
#Find the average value in the Druck column of the CSV
Ave_Voltage<-mean(Practise[,"Druck"])

#Calculate the average gauge pressure inside the tunnel by multiply average voltage by
60
  P_guage_ave <- Ave_Voltage*60

#The absolute pressure is calculated using the gauge pressure (psig).
#The gauge pressure is converted to Pa (1 psi = 6894.75729 Pa)
#Convert to absolute pressure by adding 100,000 Pa.
  P_ab <- P_guage_ave*6894.75729+100000

#Temp is assumed to be at 297K
 temp <- 297

#calculate Atmospheric Density in kg/m^3 using formula 1
atm_density<-P_ab/(287.04*temp)

#Set a gauge pressure in PSIA
P_guage_ave_psia<-P_guage_ave -14.696
```

Step 5: Convert height data to ln(height)

```
#Add an additional column in the dataframe with ln (height)
Practise<-Practise %>%
 mutate(Ln.ht=log(Height,base=exp(1)))
```

Step 6: Determine the curve needed to convert voltage to dynamic pressure

The manufacturer of the transducer (Tavis) provided calibration data to convert voltage to dynamic pressure. These curves were produced using the manufacturer's calibration for Tavis 1 and Tavis 2. The slope (VDC/psid) and y-intercept (VDC) were previously found for each static pressure (0-285 psig) and are recorded in the Tavis CSV file.

The program reads in the Tavis Calibration Curves:

```
Tavis1<-read.csv("Tavis1.csv")
Tavis2<-read.csv("Tavis2.csv")
```

In order to get the correct calibration curve for the static pressure used in the experiment, you will have to interpolate between two of these curves. An If statement is used to determine the correct two curves to interpolate between based on the calculated gauge pressure. The program determines which points are closest to the gauge pressure, then uses these points to interpolate.

Tavis 1:

```
#Determine the distance between the gauge pressure and the line pressures in the Tavis
1 data frame. Rank the distances. Will use the two that are closest to the gauge
pressure (rank 1 and 2).

Tavis1 <-
    Tavis1 %>%
    mutate(dists = abs(LinePressure-P_guage_ave)) %>%
    mutate(rank=rank(dists))


#List the two pressures that will be used to interpolate the slope and intercept

Pressure1<- Tavis1 %>% filter(rank == 1) %>% select(LinePressure)
Pressure2<- Tavis1 %>% filter(rank == 2) %>% select(LinePressure)

#Interpolate the slope using the slopes from the two line pressures that are closest to
the gauge pressure.
Slope1 <- Tavis1 %>% filter(rank == 1) %>% select(Slope)
Slope2 <- Tavis1 %>% filter(rank == 2) %>% select(Slope)


Slope_Interpolated_T1<-Slope1+(P_guage_ave-Pressure1)/(Pressure2-Pressure1)*(Slope2-Slo
pe1)
#The slope is in a dataframe still, quickly extract it into a value
Slope_Interpolated_T1<-Slope_Interpolated_T1[1,1]

#Interpolate the intercept using the intercepts from the two line pressures that are
closest to the gauge pressure.

yint1 <- Tavis1 %>% filter(rank == 1) %>% select(yint)
yint2 <- Tavis1 %>% filter(rank == 2) %>% select(yint)


yint_Interpolated_T1<-yint1+(P_guage_ave-Pressure1)/(Pressure2-Pressure1)*(yint2-yint1)
#The y-int is in a dataframe still, quickly extract it into a value
yint_Interpolated_T1<-yint_Interpolated_T1[1,1]

```

Tavis 2:

```
#Determine the distance between the gauge pressure and the line pressures in the Tavis
2 data frame. Rank the distances. Will use the two that are closest to the gauge
pressure (rank 1 and 2).

Tavis2 <-
    Tavis2 %>%
    mutate(dists = abs(LinePressure-P_guage_ave)) %>%
    mutate(rank=rank(dists))


#List the two pressures that will be used to interpolate the slope and intercept

Pressure1<- Tavis2 %>% filter(rank == 1) %>% select(LinePressure)
Pressure2<- Tavis2 %>% filter(rank == 2) %>% select(LinePressure)

#Interpolate the slope using the slopes from the two line pressures that are closest to
the gauge pressure.
Slope1 <- Tavis2 %>% filter(rank == 1) %>% select(Slope)
Slope2 <- Tavis2 %>% filter(rank == 2) %>% select(Slope)


Slope_Interpolated_T2<-Slope1+(P_guage_ave-Pressure1)/(Pressure2-Pressure1)*(Slope2-Slo
pe1)
#The slope is in a dataframe still, quickly extract it into a value
Slope_Interpolated_T2<-Slope_Interpolated_T2[1,1]

#Interpolate the intercept using the intercepts from the two line pressures that are
closest to the gauge pressure.

yint1 <- Tavis2 %>% filter(rank == 1) %>% select(yint)
yint2 <- Tavis2 %>% filter(rank == 2) %>% select(yint)


yint_Interpolated_T2<-yint1+(P_guage_ave-Pressure1)/(Pressure2-Pressure1)*(yint2-yint1)
#The y-int is in a dataframe still, quickly extract it into a value
yint_Interpolated_T2<-yint_Interpolated_T2[1,1]
```

Step 7: Convert the voltage to dynamic pressure (psid)

From this point forward, there are two data frames each dedicated to a different transducer.

```
#Set up Tavis 1 dataframe
CSV_T1<- Practise %>%
  select(Height, Ln.ht, T1)

#Set up Tavis 2 dataframe
CSV_T2<- Practise %>%
  select(Height, Ln.ht, T2)
```

To convert voltage to dynamic pressure, the scientist uses the interpolated slope and y-intercept:

$$Dynamic\ \ Pressure = (Slope\ \ Interpolated)\,(Tavis\ \ Voltage) + yint\ \ Interpolated$$

If the voltage is less than the y-intercept, then the scientist sets the dynamic pressure (dPyn) to zero.

```
  #dynamic pressure calculated using Tavis 1 transducer
CSV_T1 <-
    CSV_T1 %>%
    mutate(dynP_T1 = CSV_T1$T1*Slope_Interpolated_T1+yint_Interpolated_T1)%>%
    mutate(dynP_T1_pascal=dynP_T1*6894.75729)

   #dynamic pressure calculated using Tavis 2 transducer
CSV_T2 <-
    CSV_T2 %>%
    mutate(dynP_T2 = CSV_T2$T2*Slope_Interpolated_T2+yint_Interpolated_T2)%>%
    mutate(dynP_T2_pascal=dynP_T2*6894.75729)
```

Step 8: Convert dynamic pressure to freestream wind velocity

The program uses the following formula to convert dynamic pressure (P_{dyn} in Pa) to freestream wind velocity ($u(z)$ in m/s). Use the air density (ρ) calculated in Step 1. Note that P_{dyn} is the dynamic pressure of the gas and is a function of z (wind speed height).

$$u(z) = \sqrt{\frac{2P_{dyn}}{\rho}}$$

Step 5 calculated dynamic pressure in psid. The program converts from psid to Pa (1 psid=6894.75729 Pa)

```
#Add an additional column to the Tavis 1 dataframe for freestream wind velocity
CSV_T1 <-
    CSV_T1 %>%
    mutate(T1_u_m = sqrt((2*dynP_T1*6894.75729)/atm_density))%>%
  mutate(T1_u=T1_u_m*100)%>% #convert from m/s to cm/s
   filter(Height>0) #remove the first row because ln(0) is infinity

#Add an additional column to the Tavis 2 dataframe for freestream wind velocity
CSV_T2 <-
    CSV_T2 %>%
    mutate(T2_u_m = sqrt((2*dynP_T2*6894.75729)/atm_density))%>%
  mutate(T2_u=T2_u_m*100)%>% #convert from m/s to cm/s
  filter(Height>0) #remove the first row because ln(0) is infinity
```

Step 9: Plot the BLPs and find regression values

The program creates a function for regression purposes, that allows it to put the regression data on the plots.

```
ggplotRegression <- function (fit) {

require(ggplot2)

ggplot(fit$model, aes_string(x = names(fit$model)[2], y = names(fit$model)[1])) +
  geom_point(size=4) +
  stat_smooth(method = "lm", col = "red") +
  labs(subtitle = paste("Adj R2 = ",signif(summary(fit)$adj.r.squared, 5),
                       "Intercept =",signif(fit$coef[[1]],5 ),
                       " Slope =",signif(fit$coef[[2]], 5),
                       " P =",signif(summary(fit)$coef[2,4], 5)))
}
```

For the Tavis 1 transducer, the program determines the y-int of the regression curve of freestream speed vs ln (height).

```
#T1 Plot all the data
ggplot(CSV_T1, aes(x=T1_u, y=Ln.ht))+
    geom_point(size=4)+
    xlab("Freestream Speed T1 (cm/s)")+
    ylab("Ln height (height in cm)")
```

```
#The program will stop and ask the user to manually enter in a start and stop point for the regression

  StartReg_input <- readline("At what height should the regression start for zo (in cm)?")
  EndReg_input   <- readline("At what height should the regression end for zo (in cm)?")


#Convert the pressures and temperature entered by the user into a numeric format from character format
  StartReg<- as.numeric(unlist(strsplit(StartReg_input, ",")))
  EndReg <- as.numeric(unlist(strsplit(EndReg_input , ",")))
```

For the Tavis 1 transducer, the program determines the y-int of the regression curve of freestream speed vs ln (height).

```
#T1 Filter the data so that it plots between the start and end of the regression
CSV_T1_filtered<-CSV_T1%>%
  filter(Height>StartReg & Height<EndReg)

#Plot filtered dataset
fit_filtered_T1 <- lm(Ln.ht ~ T1_u, data = CSV_T1_filtered)
ggplotRegression(fit_filtered_T1)+
  xlab("Freestream Speed T1 (cm/s)")+
  ylab("Ln height (height in cm)")
  summary(fit_filtered_T1)

#Extract the regression coefficients
T1_Regression_Values <- summary(fit_filtered_T1)
yint_T1<-T1_Regression_Values$coefficients[[1]]
yint_error_T1<-T1_Regression_Values$coefficients[[3]]
slope_T1<-T1_Regression_Values$coefficients[[2]]
slope_error_T1<-T1_Regression_Values$coefficients[[4]]
```

For the Tavis 2 transducer, the program determines the y-int of the regression curve of freestream speed vs ln (height).

```
#T2 Plot all the data
ggplot(CSV_T2, aes(x=T2_u, y=Ln.ht))+
    geom_point(size=4)+
    xlab("Freestream Speed T2 (cm/s)")+
    ylab("Ln height (height in cm)")+
    geom_smooth(method='lm')#trendline here

#T2 Filter the data so that it plots between 0.3 and 2.2 cm
CSV_T2_filtered<-CSV_T2%>%
  filter(Height>StartReg & Height<EndReg)

#Plot filtered dataset
fit_filtered_T2 <- lm(Ln.ht ~ T2_u, data = CSV_T2_filtered)
ggplotRegression(fit_filtered_T2)+
  xlab("Freestream Speed T2 (cm/s)")+
  ylab("Ln height (height in cm)")
summary(fit_filtered_T2)

#Extract the regression coefficients
T2_Regression_Values <- summary(fit_filtered_T2)
yint_T2<-T2_Regression_Values$coefficients[[1]]
yint_error_T2<-T2_Regression_Values$coefficients[[3]]
slope_T2<-T2_Regression_Values$coefficients[[2]]
slope_error_T2<-T2_Regression_Values$coefficients[[4]]
```

The program calculates the average speed for the freestream portion of the BLP. This line will be used in Step 11 to calculate *z*.

```
#T1 Filter the data so that it plots between the end and start of the regression for the freestream height
CSV_T1_filtered_z<-CSV_T1%>%
  filter(Height>2.5 & Height<4.5)

#Find the average speed for all heights in the freestream
 mean_speed<-mean(CSV_T1_filtered_z$T1_u)
```

Step 10: Find z_o for T1 and T2

The Law of the Wall can be rewritten as:

$$ln(z) = \frac{\kappa}{u_*} + ln(z_o)$$

The freestream velocities have been plotted against the logarithmic height above the bed (z). A trendline has been fitted to this curve and from this curve the y-intercept can be calculated and is equal to $\ln(z_o)$. To calculate z_o raise $\ln(z_o)$ by e.

```
#Find zo in um for T1
zo_T1<-exp(yint_T1)*10000
zo_T1

#Find zo error for T1
zo_error_T1<-zo_T1*yint_error_T1
zo_error_T1

#Find zo in um for T2
zo_T2<-exp(yint_T2)*10000
zo_T2

#Find zo error for T2
zo_error_T2<-zo_T2*yint_error_T2
zo_error_T2
```

Step 11: Calculate z

The program finds the height of the freestream velocity by averaging the freestream speeds and plugging this value into the linear regression for Tavis 1. The program uses Tavis 1 because it has a higher-pressure range. The y value is $\ln(z)$.

```
#calculate x intercept
z_ln<-slope_T1_z*mean_speed+yint_T1_z
z<-exp(z_ln)
z #Z will be in cm
```

A5: R Code to reduce voltages to freestream speeds

Source of Data

Data were collected from the Titan Wind Tunnel at NASA Ames in Mountain View, CA. The data are in CSV format with two columns for transducer voltages and a column for the time the data was collected. The voltages are recorded every eighth of a second.

User Inputs

The program asks the user to manually enter the following information into the console:

- Name of the CSV file that contains the voltages and times recorded by Tavis 1 and 2.
- Atmospheric pressure of tunnel
- Temperature inside tunnel
- Time threshold was observed to occur at

Program Outputs

- Wind speed at threshold, calculated using both Tavis 1 and Tavis 2 transducer, so there will be two wind speeds
- Summary of all the inputs that the user types into the console

Step 1: Calculate the atmospheric density

The air density (ρ) inside the tunnel is calculated using the following equation:

$$\rho = \frac{P}{RT}$$

where *P* is the absolute pressure in Pa, *T* is the temperature in K, and *R* is the dry air constant (*R* = 287.04 Kg K). The gauge pressure shows the pressure inside the tunnel and is given in psig. The guage pressure needs to be converted to absolute pressure.

```
#Program will ask user to input the starting and end gauge pressure of the wind tunnel and the temperature inside the tunnel
#(for purposes of knitting I have already entered in the answers to the user input questions, thus I have added a # sign in front of them)

  P_start_input <- readline("what is the gauge pressure at the start of the experiment in psig?")
  P_end_input <- readline("what is the gauge pressure at the end of the experiment in psig?")
  temp_input <- readline("what is the temperature inside the tunnel in degrees Celsius?")



#Convert the pressures and temperature entered by the user into a numeric format from character format
  P_start<- as.numeric(unlist(strsplit(P_start_input, ",")))
  P_end <- as.numeric(unlist(strsplit(P_end_input, ",")))
  temp <- as.numeric(unlist(strsplit(temp_input, ",")))

#Calculate the average gauge pressure inside the tunnel
  P_guage_ave <- (P_start + P_end)/2

#The absolute pressure is calculated using the gauge pressure (psig). First the gauge pressure is converted to Pa
# (1 psi = 6894.75729 Pa) then its converted to absolute pressure by adding 100,000 Pa.
  P_ab <- P_guage_ave*6894.75729+100000


#Convert the temperature from Celsius to Kelvin
  temp<-temp+273.15

#calculate Atmospheric Density in kg/m^3 using formula 1
atm_density<-P_ab/(287.04*temp)
```

Step 2: Input the voltage data

User inputs the name of the experiment and the corresponding CSV file will be read into the program.

```
#(for purposes of knitting I have already entered in the answers to the user input questions, thus I have added a # sign in front of them)
experiment<-readline("what is the name of the experiment CSV file? (ex. T-16-1278.csv)")



# Read in the CSV file, skip the first 7 rows because data is not logged in these rows, define the names of the columns
CSV<-read.csv(experiment,skip=7,col.names=c("time","position","T1","T2","Channel3","Events1", "Events2"))
```

Step 3: Determine the curve needed to convert voltage to dynamic pressure

The manufacturer of the transducer (Tavis) provided calibration data to convert voltage to dynamic pressure. These curves were produced using the manufacturer's calibration for Tavis 1 and Tavis 2. The slope (VDC/psid) and y-intercept (VDC) were previously found for each static pressure (0-285 psig) and are recorded in the Tavis CSV file.

```
#Read in Tavis Calibration Curves:
Tavis1<-read.csv("Tavis1.csv")
Tavis2<-read.csv("Tavis2.csv")
```

In order to get the correct calibration curve for the static pressure used in the experiment, you will have to interpolate between two of these curves. An If statement is used to determine the correct two curves to interpolate between based on the gauge pressure entered in step 1 (P_gauge_ave).

```
#TAVIS 1

#Determine the distance between the gauge pressure and the line pressures in the Tavis 1 data frame. Rank the distances.
#Will use the two that are closest to the gauge pressure (rank 1 and 2).

Tavis1 <-
    Tavis1 %>%
    mutate(dists = abs(LinePressure-P_guage_ave)) %>%
    mutate(rank=rank(dists))


#List the two pressures that will be used to interpolate the slope and intercept

Pressure1<- Tavis1 %>% filter(rank == 1) %>% select(LinePressure)
Pressure2<- Tavis1 %>% filter(rank == 2) %>% select(LinePressure)

#Interpolate the slope using the slopes from the two line pressures that are closest to the gauge pressure.
Slope1 <- Tavis1 %>% filter(rank == 1) %>% select(Slope)
Slope2 <- Tavis1 %>% filter(rank == 2) %>% select(Slope)


Slope_Interpolated_T1<-Slope1+(P_guage_ave-Pressure1)/(Pressure2-Pressure1)*(Slope2-Slope1)
#The slope is in a dataframe still, quickly extract it into a value
Slope_Interpolated_T1<-Slope_Interpolated_T1[1,1]

#Interpolate the intercept using the intercepts from the two line pressures that are closest to the gauge pressure.

yint1 <- Tavis1 %>% filter(rank == 1) %>% select(yint)
yint2 <- Tavis1 %>% filter(rank == 2) %>% select(yint)


yint_Interpolated_T1<-yint1+(P_guage_ave-Pressure1)/(Pressure2-Pressure1)*(yint2-yint1)
#The y-int is in a dataframe still, quickly extract it into a value
yint_Interpolated_T1<-yint_Interpolated_T1[1,1]
```

```
#TAVIS 2

#Determine the distance between the gauge pressure and the line pressures in the Tavis 2 data frame. Rank the distances.
#Will use the two that are closest to the gauge pressure (rank 1 and 2).

Tavis2 <-
    Tavis2 %>%
    mutate(dists = abs(LinePressure-P_guage_ave)) %>%
    mutate(rank=rank(dists))


#List the two pressures that will be used to interpolate the slope and intercept

Pressure1<- Tavis2 %>% filter(rank == 1) %>% select(LinePressure)
Pressure2<- Tavis2 %>% filter(rank == 2) %>% select(LinePressure)

#Interpolate the slope using the slopes from the two line pressures that are closest to the gauge pressure.
Slope1 <- Tavis2 %>% filter(rank == 1) %>% select(Slope)
Slope2 <- Tavis2 %>% filter(rank == 2) %>% select(Slope)


Slope_Interpolated_T2<-Slope1+(P_guage_ave-Pressure1)/(Pressure2-Pressure1)*(Slope2-Slope1)
#The slope is in a dataframe still, quickly extract it into a value
Slope_Interpolated_T2<-Slope_Interpolated_T2[1,1]

#Interpolate the intercept using the intercepts from the two line pressures that are closest to the gauge pressure.

yint1 <- Tavis2 %>% filter(rank == 1) %>% select(yint)
yint2 <- Tavis2 %>% filter(rank == 2) %>% select(yint)


yint_Interpolated_T2<-yint1+(P_guage_ave-Pressure1)/(Pressure2-Pressure1)*(yint2-yint1)
#The y-int is in a dataframe still, quickly extract it into a value
yint_Interpolated_T2<-yint_Interpolated_T2[1,1]
```

Step 4: Convert the voltage to dynamic pressure (psid)

To convert voltage to dynamic pressure use the interpolated slope and y-intercept:

$$DynamicPressure = \frac{TavisVoltage - yintInterpolated}{SlopeInterpolated}$$

If the voltage is less than the y-intercept than set the dynamic pressure (dPyn) to zero.

```
#From this point forward there will be two dataframes each dedicated to a different transducer.
#Set up Tavis 1 dataframe
CSV_T1<- CSV %>%
  select(time, T1)

#Set up Tavis 2 dataframe
CSV_T2<- CSV %>%
  select(time, T2)

  #dynamic pressure calculated using Tavis 1 transducer
CSV_T1 <-
    CSV_T1 %>%
    mutate(dynP_T1 = ifelse(CSV$T1<yint_Interpolated_T1,0,(CSV$T1-yint_Interpolated_T1)/Slope_Interpolated_T1))
   #dynamic pressure calculated using Tavis 2 transducer
CSV_T2 <-
    CSV_T2 %>%
    mutate(dynP_T2 = ifelse(CSV$T2<yint_Interpolated_T2,0,(CSV$T2-yint_Interpolated_T2)/Slope_Interpolated_T2))
```

Step 5: Convert dynamic pressure to freestream wind velocity

Use the following formula to convert dynamic pressure (P_{dyn} in Pa) to freestream wind velocity ($u(z)$ in m/s). Use the air density (ρ) calculated in Step 1. Note that P_{dyn} is the dynamic pressure of the gas and is a function of z (wind speed height).

$$u(z) = \sqrt{\frac{2P_{dyn}}{\rho}}$$

Step 4 calculated dynamic pressure in psid. We need to convert from psid to Pa (1 psid=6894.75729 Pa)

```
#Add an additional column to the Tavis 1 dataframe for freestream wind velocity
CSV_T1 <-
    CSV_T1 %>%
    mutate(u_T1 = sqrt((2*dynP_T1*6894.75729)/atm_density))

#Add an additional column to the Tavis 2 dataframe for freestream wind velocity
CSV_T2 <-
    CSV_T2 %>%
    mutate(u_T2 = sqrt((2*dynP_T2*6894.75729)/atm_density))
```

Step 6: Smooth the freestream wind velocity

The transducers take voltages every 8th of a second. There is noise in this data so we will smooth out the freestream wind velocities that were calculated in Step 5. Will use the Smoothing Moving Average (SMA) function in the TTR package. Will smooth over a 2 second interval which is 16 time steps.

The smoothing algorithm smooths the data points below, I want it to be smoothed based on the centre. In other words, for 2 second smoothing, the smoothing function will take

all 16 points below and smooth them. I want it to be 8 points above and 8 points below. To achieve this an offset will be applied.

```
#Add an additional column to the Tavis 1 data frame to smooth the wind velocity
CSV_T1 <-
  CSV_T1 %>%
  mutate(u_T1_Smoothed=SMA(u_T1, n=16))%>%
 #The smoothing offseted the data a little. To account for this offest, move the entire smoothed column up 8 rows(equivalent to 1 second)
  mutate(u_T1_Smoothed_Offset=c(u_T1_Smoothed[-(seq(8))], rep(NA, 8)))

#Add an additional column to the Tavis 2 data frame to smooth the wind velocity
CSV_T2 <-
  CSV_T2 %>%
  mutate(u_T2_Smoothed=SMA(u_T2, n=16))%>%
#The smoothing offseted the data a little. To account for this offest, move the entire smoothed column up 8 rows(equivalent to 1 second)
  mutate(u_T2_Smoothed_Offset=c(u_T2_Smoothed[-(seq(8))], rep(NA, 8)))
```

Step 7: Determine the seconds since the start of the experiment

Experiment begins at 0 seconds. Each time step is an 8th of a second. Create a column that will have the seconds since the start of the experiment using a sequence fill. Increase by an 1/8 of a second (0.125).

```
#Determine the number of rows, this will be used to determine the end of the sequence.
n_row<-nrow(CSV_T1)

#Find out the total length of time of the experiment (seconds) by multiplying the number of rows by 0.125
Total_Time<-n_row*0.125

#Create a new column for the time since the start of the experiment for bothe the Tavis 1 and Tavis 2 data frames
CSV_T1 <-
  CSV_T1 %>%
  mutate(time_since_start=seq(0,Total_Time-0.125, by = 0.125) )


CSV_T2 <-
  CSV_T2 %>%
  mutate(time_since_start=seq(0,Total_Time-0.125, by = 0.125) )
```

Step 8: Input the time

While the wind tunnel is running, an observer is looking at the bed of grains and is visually determining when threshold speed is occurring. They record the threshold time since the start of the experiment in MM:SS format.

```
#Create a function that will convert Minute:Second format into seconds.
mmss_to_ss <- function  (string)
{
  mmss <- strsplit (string, ":", T)
  mm <- as.numeric (mmss[[1]][1])
  ss <- as.numeric (mmss[[1]][2])
  return (mm * 60 + ss)
}

#Program asks user to input the time in MM:SS format
#(for purposes of knitting I have already entered in the answers to the user input questions, thus I have added a # sign in front of them)
 time_input <- readline("At what time is threshold occuring (answer in MM:SS format)?")

#Convert into the time inputted into seconds from MM:SS format
time_sec<-mmss_to_ss(time_input)
```

Step 9: Find the freestream speed at threshold

Look up the freestream velocity for the time inputted in step 8 for both Tavis 1 and Tavis 2.

```
#Tavis 1

#Look up speed by filtering the data frame
u_CSV_T1<-CSV_T1%>%
  filter(time_since_start==time_sec)

#The freestream velocity is in the first row and sixth column, extract this value
u_T1<- u_CSV_T1[1,6]

#Tavis 2

#Look up speed by filtering the data frame
u_CSV_T2<-CSV_T2%>%
  filter(time_since_start==time_sec)

#The freestream velocity is in the first row and sixth column, extract this value
u_T2<- u_CSV_T2[1,6]
```

Step 10: Create a CSV file of all the program inputs and outputs

Save all the user inputs and outputs of script into one CSV file. List is given below:

- Name of the CSV file that contains the voltages and times recorded by Tavis 1 and 2. (experiment)
- Atmospheric pressure of tunnel (P_start_input; P_end_input)
- Temperature inside tunnel (temp_input)

- Time threshold was observed to occur at (time_input)
- Wind speed at threshold, calculated using both Tavis 1 and Tavis 2 transducer, so there will be two wind speeds (u_T1; u_T2)

```
#Start by creating a data frame
 threshold_speed<- data.frame(experiment, P_start_input, P_end_input,temp_input, time_input, u_T1, u_T2 )

#Create a name for the CSV file, currently experiment is a character value that we need to modify, want to eliminate the .csv format
name<-gsub(".csv","_threshold.csv" , experiment)

#export to a CSV file
write.csv(threshold_speed, file = name)
```

Vita

Emily Victoria Nield was born in Toronto, Canada on April 2nd, 1991 to parents Gail and Tony Nield. She is the younger sibling to Matthew Nield. At a young age her father encouraged her to pursue the sciences by enrolling her in science themed after school activities and always answering all of her questions about the world. She attended the Country Day School in King City, ON from elementary school through high school. In high school, her geography teacher inspired her to study earth sciences and to attend Trent University. She graduated high school in 2009 and moved to Peterborough, ON to study at Trent where she doubled majored in Physics and Physical Geography. In her sophomore year, her physics lab instructor helped her get an undergraduate summer research assistantship at the University of Guelph. This research focused on the calibration of the Alpha Particle X-Ray Spectrometer (APXS), an instrument on the Mars Exploration Rovers and the Mars Science Laboratory rover. She discovered her love of planetary science at this job. During her junior year at Trent, she became interested in aeolian studies and had the fortunate opportunity to conduct research at the Trent Environment Wind Tunnel. She quickly became captivated by the wind and knew she wanted to continue studying aeolian processes in graduate school. She combined her love of planetary science and aeolian geomorphology by studying threshold speeds on Titan at the University of Tennessee under the supervision of Dr. Devon Burr.

Because of her family, Emily Nield has lived a fortunate life. Her parents instilled a sense of adventure into her that has led her to travel all across the globe. She has watched sea turtles hatch in Costa Rica, studied French in France, went on safaris in Botswana and Zambia, visited the deserts in Namibia and Utah, hiked the highlands in Scotland, she has zip lined in every Central American country, visited the Potala Palace in Tibet, held baby pandas in China, and much more. She is excited to continue to explore this amazing world and to go on her next adventure.